A cross-kingdom conserved ER-phagy receptor maintains endoplasmic reticulum homeostasis during stress

Authors

Madlen Stephani[1*], Lorenzo Picchianti[1,2*], Alexander Gajic[1], Rebecca Beveridge[2], Emilio Skarwan[1], Victor Sanchez de Medina Hernandez[1], Azadeh Mohseni[1], Marion Clavel[1], Yonglung Zeng[3], Christin Naumann[4], Mateusz Matuszkiewicz[1,5], Eleonora Turco[6], Christian Loefke[1], Baiying Li[3], Gerhard Durnberger[1,2], Michael Schutzbier[1,2], Hsiao Tieh Chen[1,3], Alibek Abdrakhmanov[1],Adriana Savova[6], Khong-Sam Chia[1,10], Armin Djamei[1,10], Irene Schaffner[7], Steffen Abel[4], Liwen Jiang[3], Karl Mechtler[1,2], Fumiyo Ikeda[8,9], Sascha Martens[6], Tim Clausen[2,11], Yasin Dagdas[1,12]

Affiliations

[1] Gregor Mendel Institute (GMI), Austrian Academy of Sciences, Vienna BioCenter (VBC), Vienna, Austria.

[2] Research Institute of Molecular Pathology (IMP), Vienna BioCenter (VBC), Vienna, Austria.

[3] School of Life Sciences, Centre for Cell and Developmental Biology and State Key Laboratory of Agrobiotechnology, The Chinese University of Hong Kong, Shatin, New Territories, Hong Kong, China.

[4] Department of Molecular Signal Processing, Leibniz Institute of Plant Biochemistry, Halle (Saale), Germany.

[5] Department of Plant Genetics, Breeding and Biotechnology, Warsaw University of Life Sciences-SGGW, Nowoursynowska 159, Warsaw, Poland.

[6] Department of Biochemistry and Cell Biology, Max Perutz Labs, University of Vienna, Vienna BioCenter (VBC), Vienna, Austria.

[7] BOKU Core Facility Biomolecular & Cellular Analysis, University of Natural Resources and Life Sciences, Vienna, Austria.

[8] Institute of Molecular Biotechnology of the Austrian Academy of Sciences (IMBA), Vienna BioCenter (VBC), Vienna, Austria.

[9] Department of Molecular and Cellular Biology, Medical Institute of Bioregulation, Kyushu University, Fukuoka, Japan

[10] Current address: Department of Breeding Research, Leibniz Institute of Plant Genetics and Crop Plant Research (IPK), Gatersleben, Germany

[11] Medical University of Vienna, Vienna, Austria

[12] Lead Contact

[*] These authors contributed equally to this work.

Correspondence: Tim Clausen, tim.clausen@imp.ac.at and Yasin Dagdas, yasin.dagdas@gmi.oeaw.ac.at

Summary

Eukaryotes have evolved various quality control mechanisms to promote proteostasis in the ER. Selective removal of certain ER domains via autophagy (termed as ER-phagy) has emerged as a major quality control mechanism. However, the degree to which ER-phagy is employed by other branches of ER-quality control remains largely elusive. Here, we identify a cytosolic protein, C53, that is specifically recruited to autophagosomes during ER-stress, in both plant and mammalian cells. C53 interacts with ATG8 via a distinct binding epitope, featuring a shuffled ATG8 interacting motif (sAIM). C53 senses proteotoxic stress in the ER lumen by forming a tripartite receptor complex with the ER-associated ufmylation ligase UFL1 and its membrane adaptor DDRGK1. The C53/UFL1/DDRGK1 receptor complex is activated by stalled ribosomes and induces the degradation of internal or passenger proteins in the ER. Consistently, the C53 receptor complex and ufmylation mutants are highly susceptible to ER stress. Thus, C53 forms an ancient quality control pathway that bridges selective autophagy with ribosome-associated quality control at the ER.

Introduction

Autophagy is an intracellular degradation process where eukaryotic cells remove harmful or unwanted cytoplasmic contents to maintain cellular homeostasis (Dikic and Elazar, 2018; Klionsky et al., 2011; Marshall and Vierstra, 2018). Recent studies have shown that autophagy is highly selective (Johansen and Lamark, 2019; Stolz et al., 2014), and is mediated by receptors that recruit specific cargo, such as damaged organelles or protein aggregates. Autophagy receptors and their cargo are incorporated into the growing phagophore through interaction with ATG8, a ubiquitin-like protein that is conjugated to the phagophore upon activation of autophagy (Stolz et al., 2014; Zaffagnini and Martens, 2016). The phagophore grows, and eventually forms a double-membrane vesicle termed the autophagosome. Autophagosomes then carry the autophagic cargo to lytic compartments for degradation and recycling. Selective autophagy receptors interact with ATG8 via conserved motifs called the ATG8 interacting motif (AIM) or LC3-interacting region (LIR) (Birgisdottir et al., 2013). In contrast to mammals and yeast, cargo receptors that mediate organelle recycling remains mostly elusive in plants (Stephani and Dagdas, 2019).

The endoplasmic reticulum (ER) is a highly dynamic heterogeneous cellular network that mediates folding and maturation of ~40 % of the proteome (Sun and Brodsky, 2019; Walter and Ron, 2011). Proteins that pass through the ER include all secreted and plasma membrane proteins and majority of the organellar proteins. This implies, ER could handle up to a million client proteins in a cell every minute (Karagöz et al., 2019). Unfortunately, the folding process is inherently error prone and misfolded proteins are toxic to the cell (Fregno and Molinari, 2019; Karagöz et al., 2019; Sun and Brodsky, 2019). To maintain the

proteostasis in the ER, eukaryotes have invested in quality control mechanisms that closely monitor, and if necessary, trigger the removal of terminally misfolded proteins. Degradation of the faulty proteins is mediated by proteasomal and vacuolar degradation pathways (Fregno and Molinari, 2019).

One of the main vacuolar/lysosomal degradation processes is ER-phagy. It has emerged as a major quality control pathway, and defects in ER-phagy is linked to various diseases (Chino and Mizushima, 2020; Hübner and Dikic, 2019; Stolz and Grumati, 2019; Wilkinson, 2019). ER-phagy involves cargo receptors that mediate removal of certain regions of the ER via autophagy. Several ER-resident ER-phagy receptors have been identified. These include Fam134B, RTN3L, ATL3, Sec62, CCPG1, and TEX264 in mammals and ATG39 and ATG40 in yeast (An et al., 2019; Chen et al., 2019; Chino et al., 2019; Fumagalli et al., 2016; Grumati et al., 2017; Khaminets et al., 2015; Mochida et al.; Smith et al., 2018). A recent study showed reticulon proteins could also function as ER-phagy receptors in plants (Zhang et al., 2020). These receptors are activated during starvation or stress conditions and remodel the ER network to maintain proteostasis. Despite the emerging links, how ER-phagy cross-talks with the rest of the ER quality control pathways needs further investigation (Chino and Mizushima, 2020; Dikic, 2018).

Here, using a peptide-competition coupled affinity proteomics screen, we identified a highly conserved cytosolic protein, C53, that is specifically recruited into autophagosomes during ER stress. C53 interacts with plant and mammalian ATG8 isoforms via non-canonical ATG8 interacting motifs (AIM), termed shuffled AIM (sAIM). C53 is recruited to the ER by forming a ternary receptor complex with the UFL1, the E3 ligase that mediates ufmylation, and its ER membrane adaptor DDRGK1 (Gerakis et al., 2019). C53 mediated autophagy is activated upon ribosome stalling during co-translational protein translocation and mediates degradation of model ribosome stalling constructs and various other ER resident or folded proteins. Consistently, C53 is crucial for ER stress tolerance in both plants and HeLa cells.

Results

C53 interacts with plant and mammalian ATG8 isoforms in an ER-stress dependent manner.

To identify specific cargo receptors that mediate selective removal of ER compartments during proteotoxic stress, we performed an immunoprecipitation coupled to mass spectrometry (IP-MS) screen to identify AIM-dependent ATG8 interactions triggered by ER stress. We hypothesized that a synthetic AIM peptide that has higher affinity for ATG8 can outcompete, and thus reveal, AIM-dependent ATG8 interactors. To identify this synthetic peptide, we performed a peptide array analysis that revealed the AIM *wt* peptide (Figure S1a, b; Table S1). Using isothermal titration calorimetry (ITC), we showed that the AIM *wt* binds

71 ATG8 with nanomolar affinity (K_D=~700 nM), in contrast to the AIM mutant peptide (AIM *mut*), which
72 does not show any binding (Figure S1c-f) or the low micromolar-range affinities measured for most cargo
73 receptors (Zaffagnini and Martens, 2016). As plants have an expanded set of ATG8 proteins, we first tested
74 if any of the ATG8 isoforms specifically responded to ER stress induced by tunicamycin (Kellner et al.,
75 2016). Tunicamycin inhibits glycosylation and leads to proteotoxic stress at the ER (Bernales et al., 2006).
76 Quantification of ATG8 puncta in transgenic seedlings expressing GFP-ATG8A-I revealed that
77 tunicamycin treatment significantly induced all nine ATG8 isoforms (Figure S2). Since all ATG8 isoforms
78 were induced, we chose ATG8A, and performed peptide competition coupled IP-MS analysis (See methods
79 for detailed description). In addition to well-known AIM dependent ATG8 interactors such as ATG4
80 (Autophagy related gene 4) and NBR1 (Neighbour of BRCA1) (Wild et al., 2014), our analyses revealed
81 that the highly conserved cytosolic protein C53 (aliases: CDK5RAP3, LZAP, IC53, HSF-27) is an AIM-
82 dependent ATG8 interactor (Figure 1a, Table S2, Figure S3).
83
84 To confirm our IP-MS results, we performed *in vitro* pull-down experiments. *Arabidopsis thaliana* (At*)*
85 C53 specifically interacted with GST-ATG8A, and this interaction was outcompeted with the AIM *wt*, but
86 not AIM *mut* peptide. Consistently, ATG8 receptor accommodating site mutations (LDS – LIR Docking
87 Site) prevented C53 binding (Figure 1b). We extended our analysis to all Arabidopsis ATG8 isoforms and
88 showed that AtC53 interacts with 8 of 9 Arabidopsis isoforms. To probe for evolutionary conservation of
89 C53-ATG8 interaction, we tested the orthologous proteins from the basal land plant *Marchantia*
90 *polymorpha* (Mp) and showed that MpC53 interacts with 1 of 2 Marchantia ATG8 isoforms (Figure S4a,
91 b). As C53 is highly conserved in multicellular eukaryotes and has not been characterized as an ATG8
92 interactor in mammals, we tested whether human C53 (HsC53) interacts with human ATG8 isoforms
93 (LC3A-C, GABARAP, -L1, -L2). HsC53 interacted with GABARAP and GABARAPL1 in an AIM-
94 dependent manner via the LIR docking site, similar to plant C53 homologs (Figure 1c, Figure S4c, d).
95 Together, these data suggest that C53-ATG8 interaction is conserved across kingdoms.
96
97 In order to examine the *in vivo* link between C53 and ATG8 function, we generated transgenic AtC53-
98 mCherry Arabidopsis lines and measured autophagic flux during ER stress. Without stress, AtC53
99 displayed a diffuse cytosolic pattern. Similarly, upon carbon starvation (-C, Figure 1d), which is commonly
100 used to activate bulk autophagy, AtC53-mCherry remained mostly diffuse (Marshall and Vierstra, 2018).
101 However, tunicamycin (Tm) treatment led to a rapid increase in AtC53 puncta. The number of puncta was
102 further increased upon concanamycin A (ConA) treatment that inhibits vacuolar degradation, suggesting
103 that AtC53 puncta are destined for vacuoles (Figure 1d). The AtC53 puncta disappeared when AtC53-
104 mCherry lines were crossed into core autophagy mutants *atg5* and *atg2*, confirming that formation of AtC53
105 puncta is dependent on macroautophagy (Figure 1d). Consistent with this, other ER-stressors such as

106 phosphate starvation, cyclopiazonic acid (CPA), and dithiothreitol (DTT) treatments also induced AtC53
107 puncta (Figure S5) (Fumagalli et al., 2016; Naumann et al., 2018; Smith et al., 2018). The AtC53 puncta
108 co-localized with GFP-ATG8A and GFP-ATG11, indicating that they are autophagosomes (Figure 1e,
109 Figure S6a). Moreover, as recently shown for other selective autophagy receptors, AtC53 and HsC53
110 directly interacted with the mammalian ATG11 homolog FIP200 (PTK2/FAK family-interacting protein of
111 200 kDa) (Figure S6b) (Lahiri and Klionsky, 2018; Ravenhill et al., 2019; Turco et al., 2019; Vargas et al.,
112 2019). Ultrastructural analysis using immunogold labelling also confirmed localization of AtC53 at
113 autophagosomes during ER-stress (Figure S7). Similar to plant proteins, transfected HsC53-GFP co-
114 localized with mCherry-GABARAP upon tunicamycin treatment in HeLa cells. The number of HsC53
115 puncta increased upon bafilomycin (BAF) treatment, which inhibits lysosomal degradation; suggesting that
116 HsC53 puncta eventually fuse with lysosomes (Figure 1f). To support our imaging-based autophagic flux
117 assays, we also performed western blot based autophagic flux analyses, which further demonstrated ER-
118 stress specific autophagic degradation of AtC53 and HsC53 (Figure 2).
119
120 **C53-ATG8 interaction is mediated by non-canonical shuffled ATG8 interacting motifs (sAIM)**
121
122 Having validated C53 as an autophagy substrate, we next sought to identify its ATG8-interacting motif
123 (AIM). For this purpose, we reconstituted the binary complex *in vitro* and determined the stoichiometry of
124 the C53-ATG8 interaction by native mass spectrometry (nMS). Both HsC53 and AtC53 formed 1:1 and 1:2
125 complexes with GABARAP and ATG8A, respectively; pointing to the existence of multiple binding
126 epitopes (Figure 3a). To map the ATG8-binding region of C53, we performed *in vitro* pull downs using
127 truncated proteins. C53 contains an intrinsically disordered region (IDR) that bridges two α-helical domains
128 located at the N and C termini. *In vitro* pull downs revealed that the IDR is necessary and sufficient to
129 mediate ATG8 binding, as also confirmed with ITC and nMS experiments (Figure 3b-d, Figure S8).
130 Multiple sequence alignment of the C53-IDR uncovered three highly conserved sites with the consensus
131 sequence "IDWG", representing a shuffled version of the canonical AIM sequence (W/F/Y-X-X-L/I/V)
132 (Figure 3c, Figure S9). Mutational analysis of the three shuffled AIM sites in HsC53 and AtC53 revealed
133 the importance of the sAIM epitopes for binding to GABARAP and ATG8, respectively; though in AtC53,
134 an additional canonical AIM had to be mutated to fully abrogate the binding (Figure 3e). ITC experiments
135 with the purified IDRs, as well as nMS and surface plasmon resonance (SPR) experiments with full length
136 proteins, also supported sAIM-mediated ATG8-binding for both HsC53 and AtC53 (Figure 3f, g, Figure
137 S10). Circular dichroism spectroscopy showed that sAIM mutants had very similar secondary structures to
138 the wild type proteins, suggesting that lack of ATG8 binding is not due to misfolding (Figure S10c). To
139 verify our *in vitro* results *in vivo*, we analysed the subcellular distribution of sAIM mutants in transgenic
140 Arabidopsis lines and transfected HeLa cells. Confocal microscopy analyses showed that $C53^{sAIM}$ mutants

were not recruited into autophagosomes and had diffuse localization patterns upon ER stress induction (Figure 3h, i). Altogether these biochemical and cell biological analyses show that C53 is recruited to the autophagosomes by interacting with ATG8 via the non-canonical sAIMs.

C53 is activated by ribosome stalling during co-translational protein translocation

Next, we looked for client proteins subject to C53-mediated autophagy. Quantitative proteomics analyses of wild type and AtC53 mutant lines revealed that AtC53 mediates degradation of ER resident proteins as well as proteins passaging the ER to the cell wall, apoplast, and lipid droplets (Figure S11, Table S3, 4). These data are consistent with a recent study, showing that ER-resident proteins accumulate in a conditional mutant of mouse C53 (Yang et al., 2019). Since C53 is a cytosolic protein, we then explored how it senses proteotoxic stress in the ER lumen, considering four likely scenarios: C53 may collaborate with (*i*) a sensor of the unfolded protein response (UPR) (Karagöz et al., 2019) or (*ii*) a component of the ER-associated degradation pathway (ERAD) (Sun and Brodsky, 2019). Alternatively, it may sense clogged translocons caused by (*iii*) ribosome stalling triggered during co-translational protein translocation (Wang et al., 2019) or (*iv*) aberrant signal recognition particle (SRP) independent post-translational protein translocation events (Ast et al., 2016) (Figure S12a). To test the connection with the UPR system, we used western blot and live cell imaging based autophagic flux assays and demonstrated that AtC53 flux was already higher than wild type in Arabidopsis UPR sensor mutants *ire1a/b* and *bzip17/28* (Figure S12b, c) (Kim et al., 2018; Koizumi et al., 2001). Consistently, inhibition of Ire1 activity using chemical inhibitors 4μ8c or KIRA6 also increased HsC53 puncta in HeLa cells (Figure S12d); indicating that recruitment of C53 to the autophagosomes does not depend on UPR sensors (Maly and Papa, 2014). Next, we performed colocalization analyses using model ERAD substrates. In transgenic plant lines expressing model ERAD substrates, the client proteins did not colocalize with AtC53 puncta (Figure S13a) (Shin et al., 2018). Likewise, the model mammalian ERAD substrates GFP-CFTRΔF508 (ERAD-C), A1AT^{NHK}-GFP (ERAD-L), and INSIG1-GFP (ERAD-M) only partially colocalized with HsC53 puncta in HeLa cells (Figure S13b), suggesting C53-mediated autophagy may cross-talk with the ERAD pathway (Leto et al., 2019).

Next, we tested the effect of clogged translocons on C53 function. Remarkably, HsC53 significantly colocalized with the ER-targeted ribosome stalling construct ER-K20 (Wang et al., 2019), but not with an SRP-independent translocon clogger construct (Ast et al., 2016), despite both leading to clogging at the Sec61 translocon (Figure S13c). HsC53 puncta were also induced by anisomycin treatment (Figure S13d), which also leads to ribosome stalling (Wang et al., 2019). Consistently, silencing of HsC53 using shRNA significantly reduced lysosomal trafficking of ER-K20 (Figure S13e), suggesting C53 is activated upon ribosome stalling during co-translational protein translocation (Wamsley et al., 2017).

176 **C53 forms a tripartite receptor complex with the ufmylation E3 ligase UFL1 and its membrane**
177 **adaptor DDRGK1**
178
179 How is C53 recruited to the ER during ribosome stalling? Notably, C53 has been previously linked to
180 UFL1, an E3 ligase that mediates ufmylation of stalled, ER-bound ribosomes, modifying ribosomal protein
181 RPL26 (Walczak et al., 2019; Wang et al., 2019). To test if C53 forms a higher order receptor complex, we
182 analysed the interaction of C53 with UFL1 and its ER membrane adaptor DDRGK1 (Gerakis et al., 2019).
183 *In vitro* pull-down assays and yeast two hybrid analysis showed that AtUFL1 directly interacts with AtC53
184 and AtDDRGK1 (Figure 4a, Figure S14a). Consistently, AtC53 associates with DDRGK1 and UFL1 in *in*
185 *vivo* coimmunoprecipitations (Figure 4b). Furthermore, co-localization of UFL1 and DDRGK1 with AtC53
186 in punctate structures increases upon ER stress and these puncta are delivered to the vacuole (Figure 4c, d,
187 Figure S14b, c). Strikingly, AtC53 autophagic flux requires functional UFL1 and DDRGK1, as the number
188 of AtC53 puncta were significantly lower in ufl1 and ddrgk1 mutants (Figure 4e, Extended Figure 14d).
189 Altogether these data suggest C53 is recruited to the ER by forming a tripartite receptor complex with UFL1
190 and DDRGK1.
191
192 We then explored how C53 is kept inactive under normal conditions. We hypothesized that UFM1 may
193 safeguard the C53 receptor complex under normal conditions and keep ATG8 at bay. Upon ER stress,
194 UFM1 would be transferred to RPL26, exposing sAIMs on C53. To test this, we first tested UFM1-C53
195 interaction, using i*n vitro* pull downs, and showed that AtC53 can interact with AtUFM1 (Figure 4f).
196 Furthermore, *in vitro* competition experiments suggested a competition between UFM1 and ATG8 (Figure
197 4f), reminiscent of the mutually exclusive UFM1 and GABARAP binding of UBA5, the E1 enzyme in the
198 ufmylation cascade (Huber et al., 2019). We then performed *in vivo* co-immunoprecipitation experiments
199 during ER stress. Consistent with our hypothesis and *in vitro* data, ER stress led to depletion of UFM1 and
200 enhanced AtC53-ATG8 interaction (Figure 4g, h, Figure S14e). Altogether, these data suggest that the two
201 ubiquitin-like proteins UFM1 and ATG8 compete with each other for association with the C53 receptor
202 complex (Figure 4i).
203
204 **C53 is crucial for ER stress tolerance**
205
206 Finally, we examined if C53 is physiologically important for ER stress tolerance. First, we tested if C53
207 plays a general role in autophagy using carbon and nitrogen starvation assays. Carbon and nitrogen
208 starvation are typically used to characterize defects in bulk autophagy responses (Marshall and Vierstra,
209 2018). In contrast to the core autophagy mutants *atg5* and *atg2*, CRISPR-generated *Atc53* mutants did not
210 show any phenotype under carbon or nitrogen starvation conditions (Figure 5a, b). However, consistent

211 with increased flux, *Atc53* mutants were highly sensitive to phosphate starvation, which has been shown to
212 trigger an ER stress response (Naumann et al., 2018) (Figure 5c, Figure S15a). Similarly, in both root length
213 and survival assays, *Atc53* mutants were sensitive to tunicamycin treatment (Figure 5d, Figure S15b, c). In
214 addition, ufmylation machinery mutants (Figure 5e), including *ufl1* and *ddrgk1*, were also sensitive to
215 tunicamycin treatment but insensitive to carbon and nitrogen starvation (Figure 5f, Figure S15d, e). Lastly,
216 the *Marchantia polymorpha c53* mutant was also sensitive to tunicamycin, suggesting C53 function is
217 conserved across the plant kingdom (Figure S15f). We then performed complementation assays using wild
218 type AtC53 and the AtC53^{sAIM} mutant. AtC53 expressing lines behaved like wild type plants in tunicamycin
219 supplemented plates (Figure 5g). However, AtC53^{sAIM} mutant did not complement the tunicamycin
220 sensitivity phenotype, and had significantly shorter roots (Figure 5g, Figure S15g). Parallel to analysing
221 C53-mediated ER homeostasis in plants, stress tolerance assays in HeLa cells showed that silencing of
222 HsC53 led to an induction of Bip3 chaperone protein levels (Figure S15h), indicating increased ER stress.
223 Complementation of *Hsc53* silenced lines with HsC53-GFP dampened Bip3 expression (Figure S15h).
224 Altogether, these results demonstrate that C53 coordinated ER-phagy is crucial for ER stress tolerance in
225 plant and mammalian cells.
226
227 **Discussion**
228
229 In conclusion, our data show that C53 forms an ancient autophagy receptor complex that is closely
230 connected to the ER quality control system via the ufmylation pathway. During ER stress, UFM1 is depleted
231 from the C53-receptor complex, exposing the sAIM motifs on C53 for ATG8 binding. Notably, the Sec61
232 translocon and ER-associated ribosomes are not targeted by C53, pointing to further factors complementing
233 the C53/UFM1/DDRDPK system of selective ER-phagy.
234
235 Our findings highlight C53 mediated ER-phagy is a central player operating at the interface of key quality
236 control pathways, controlling ER homeostasis across different kingdoms of life. Consistently, recent
237 genome wide CRISPR screens identified ufmylation as a major regulator of ER-phagy, the ERAD pathway,
238 and viral infection (Kulsuptrakul et al., 2019; Leto et al., 2019; Liang et al., 2020). Excitingly, using
239 fluorescent reporter lines and genome wide CRISPRi screens, Liang et al., showed that ufmylation plays a
240 major role in regulating starvation induced ER-phagy. They showed that both DDRGK1 and UFL1 are
241 critical for starvation induced ER-phagy; whereas C53 mutants did not show any ER-phagy defects (Liang
242 et al., 2020). Our results using stable transgenic organisms show that C53 mediated autophagy is not
243 activated by carbon or nitrogen starvation that are typically used to activate bulk autophagy. C53 is activated
244 by phosphate starvation, but this is not due starvation but because of the ER stress triggered during
245 phosphate starvation. Furthermore, C53 and the ufmylation machinery is asymptomatic during carbon or

246 nitrogen starvation. Additionally, Liang et al., show ufmylation works together with known ER-phagy
247 receptors such as Fam134B. Whether C53 also works with other ER-phagy receptors needs further
248 investigation. Differences in our and Liang et. al.'s findings may imply cell-type specific differences and
249 highlight the need for further studies to resolve the discrepancies.
250
251 C53 and ufmylation are essential for mammalian development (Gerakis et al., 2019). Defects in C53
252 receptor complex have been associated with various diseases including liver cancer, pancreatitis, and
253 cardiomyopathy (Gerakis et al., 2019). Our results suggest C53 and ufmylation is also critical for stress
254 tolerance in plants, but they are not essential for development; suggesting plants have evolved
255 compensatory mechanisms during adaptation to sessile life. Future comparative studies could reveal these
256 mechanisms and help us develop sustainable strategies for promoting ER proteostasis during stress in
257 mammals and plants.
258
259 **Acknowledgements**
260 We thank R. Strasser, M. Schuldiner, R. Kopito, J. Christianson, K. Mukhtar, S. Howell, D. Hofius, R.
261 Vierstra, Y. Ye, W. Yarbrough and T. Ueda for sharing plasmids or plant lines. We acknowledge the Vienna
262 BioCenter Core Facilities GmbH (VBCF) facilities Plant Sciences (J. Jez), Electron Microscopy (T. Heuser,
263 S. Jakob, M. Brandstetter), and Protein Technologies (P. Stolt-Bergner, A. Sedivy, J. Neuhold, A. Lehner)
264 as well as the GMI/IMBA/IMP Protein Chemistry Core facility (M. Madalinski, E. Roitinger, K. Stejskal,
265 R. Imre) and A. Schleiffer for their help with the experiments. The SPR and ITC equipment were kindly
266 provided by the EQ-BOKU VIBT GmbH and the BOKU Core Facility Biomolecular & Cellular Analysis.
267 We thank members of the *Vienna Biocenter Ubiquitin Club* for fruitful discussions. This work has been
268 funded by the Vienna Science and Technology Fund (WWTF) through project LS17-047 (YD, TC), the
269 Austrian Science Fund (FWF): P32355 (YD), P30401-B21 (SM), I3033-B22 (AD), Unidocs Fellowship
270 (AS), ERC grant No.646653 (S.M.), and the Austrian Academy of Sciences. M.M. is financially supported
271 by The Financial Supports for Young Scientists (WULS-SGGW) International Research Scholarship Fund
272 No. BWM 315/2018. We thank Claudine Kraft, Elif Karagoz, James Watson and Youssef Belkhadir for
273 critical evaluation of the manuscript. We also acknowledge Sabbi Lall, Life Science Editors for editing
274 assistance.
275
276 **Author Contributions.** MS, LP, TC and YD conceived and designed the project. MS, ES, AM, MC, CN,
277 MM and CL, performed plant related experiments. AG, AA, AS performed or contributed to human cell
278 culture related experiments. RB performed native mass spectrometry experiments. KC performed the yeast
279 two hybrid assays. LP, VM, ET and HC performed *in vitro* biochemical and biophysical assays. YZ, BL
280 performed electron microscopy experiments. GD, MS performed quantitative mass spectrometry

experiments. AD, IS, SA, LJ, KM, FI, SM, TC, YD supervised the project. MS, LP, AG and YD wrote the manuscript with input from all the authors.

Competing interest declaration. S.M is member of the scientific advisory board of Casma Therapeutics.

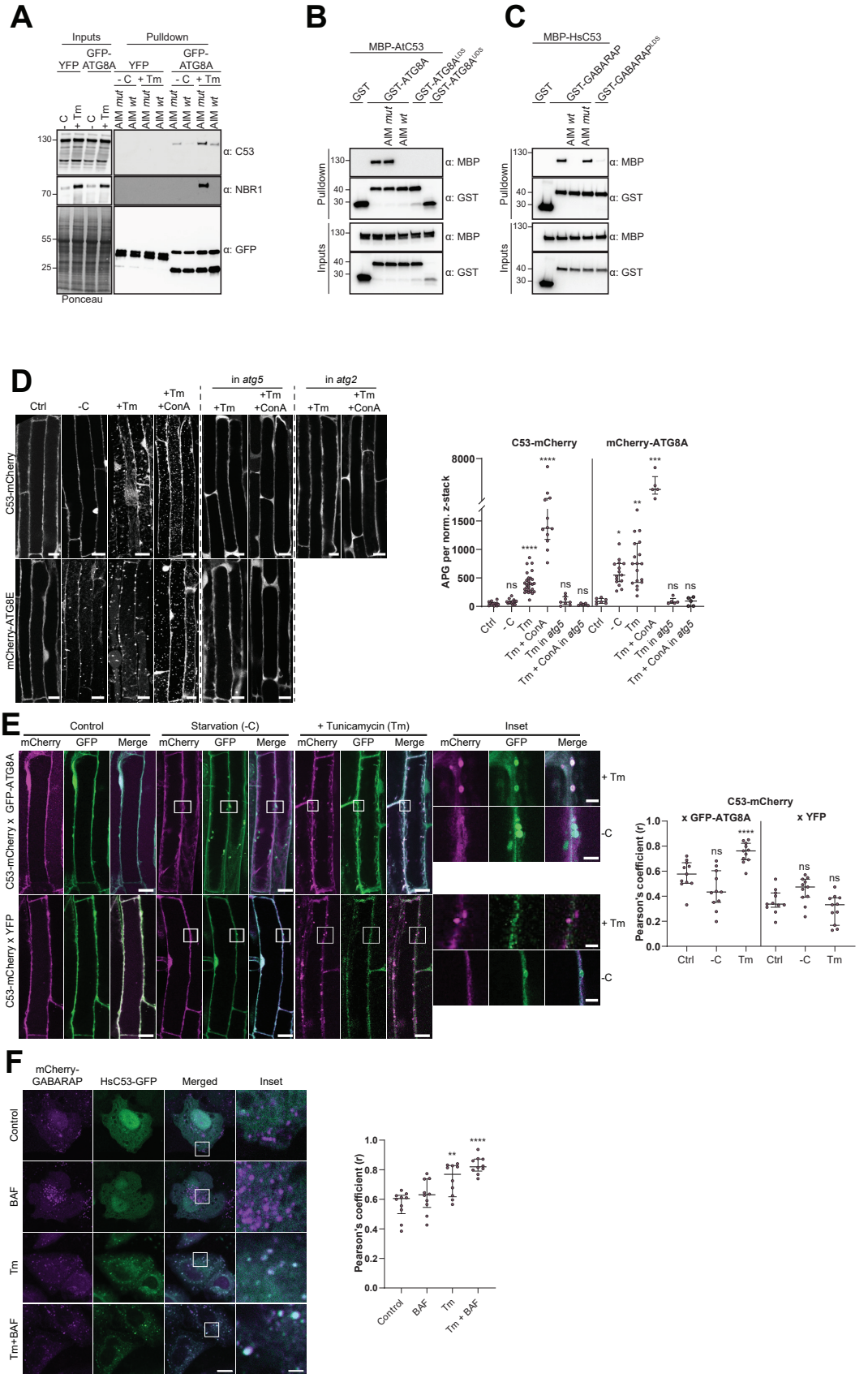
A
Inputs
Pulldown
GFP-ATG8A
YFP
- C
+ Tm
AIM mut
AIM wt
α: C53
α: NBR1
α: GFP
Ponceau
B
MBP-AtC53
GST
GST-ATG8A
GST-ATG8A^LDS
Pulldown
Inputs
α: MBP
α: GST
C
MBP-HsC53
GST-GABARAP
GST-GABARAP^LDS
D
Ctrl
-C
+Tm
+ConA
in atg5
in atg2
C53-mCherry
mCherry-ATG8E
APG per norm. z-stack
Tm + ConA
Tm in atg5
Tm + ConA in atg5
E
Control
Starvation (-C)
+ Tunicamycin (Tm)
Inset
mCherry
GFP
Merge
C53-mCherry x GFP-ATG8A
C53-mCherry x YFP
Pearson's coefficient (r)
x GFP-ATG8A
x YFP
F
mCherry-GABARAP
HsC53-GFP
Merged
Inset
BAF
Tm+BAF

288 **Figure 1. C53 binds ATG8 in an AIM dependent manner and undergoes ER-stress specific**
289 **autophagic degradation.** (**A**) **Peptide competition coupled *in vivo* pull-down revealed C53 as an AIM**
290 **dependent ATG8 interactor.** *In vivo* co-immunoprecipitation of extracts of Arabidopsis seedlings
291 expressing YFP alone or GFP-ATG8A incubated in sucrose (-C)-deficient or 10 µg/ml tunicamycin (Tm)
292 containing media. The peptides AIM *wt* and AIM *mut* were added to a final concentration of 200 µM. Input
293 and bound proteins were visualized by immunoblotting with anti-GFP, anti-NBR1, and anti-C53 antibodies.
294 (**B, C**) **AtC53 and HsC53 interact with ATG8A and GABARAP, respectively, in an AIM-dependent**
295 **manner**. Bacterial lysates containing recombinant protein were mixed and pulled down with glutathione
296 magnetic agarose beads. The peptides AIM *wt* and AIM *mut* were added to a final concentration of 200
297 µM. Input and bound proteins were visualized by immunoblotting with anti-GST and anti-MBP antibodies.
298 LDS=LIR-Docking-Site mutant (Marshall et al., 2019); UDS = Ubiquitin Docking Site mutant (Marshall
299 et al., 2019). (**D**) **AtC53 is specifically recruited to puncta upon ER stress and this depends on ATG5**
300 **and ATG2.** *Left Panel*, representative confocal images of transgenic Arabidopsis seedlings expressing
301 C53-mCherry and mCherry-ATG8E in Col-0 wild type, *atg5* and *atg2* mutant backgrounds. 6-day old
302 seedlings were incubated in either control, sucrose (-C)-deficient, tunicamycin (10 µg/ml), or tunicamycin
303 (Tm, 10 µg/ml) + Concanamycin (ConA, 1 µM) containing media. Scale bars, 10 µm. *Right Panel*,
304 Quantification of the autophagosomes (APG) per normalized Z-stacks. Bars represent the mean (± SD) of
305 at least 10 biological replicates. (**E**) **AtC53 puncta colocalize with GFP-ATG8A labelled**
306 **autophagosomes during ER stress**. *Left Panel*, Co-localization analyses of single plane confocal images
307 obtained from transgenic Arabidopsis roots co-expressing C53-mCherry (magenta) with GFP-ATG8A or
308 YFP alone (green). 4-day old seedlings were incubated in either control, sucrose deficient (-C), or
309 tunicamycin containing media. Scale bars, 20 µm. Inset scale bars, 2 µm. *Right Panel*, Pearson's Coefficient
310 (r) analysis of the colocalization of C53-mCherry with GFP-ATG8A or YFP alone. Bars represent the mean
311 (± SD) of at least 5 biological replicates. (**F**) **HsC53 puncta colocalize with mCherry-GABARAP**
312 **labelled autophagosomes during ER stress.** *Left Panel***,** Confocal images of PFA fixed HeLa cells
313 transiently expressing C53-GFP (green) and mCherry-GABARAP (magenta). Cells were either untreated
314 (Control) or treated with tunicamycin (Tm) or Tm + Bafilomycin (BAF). Scale bar, 20 µm. Inset scale bar,
315 2 µm. *Right Panel*, Pearson's Coefficient analysis of the colocalization of HsC53-GFP with mCherry-
316 GABARAP under control and Tm treated conditions. Bars represent the mean (± SD) of at least 5 biological
317 replicates. Significant differences are indicated with * when p value ≤ 0.05, ** when p value ≤ 0.01, and
318 *** when p value ≤ 0.001.

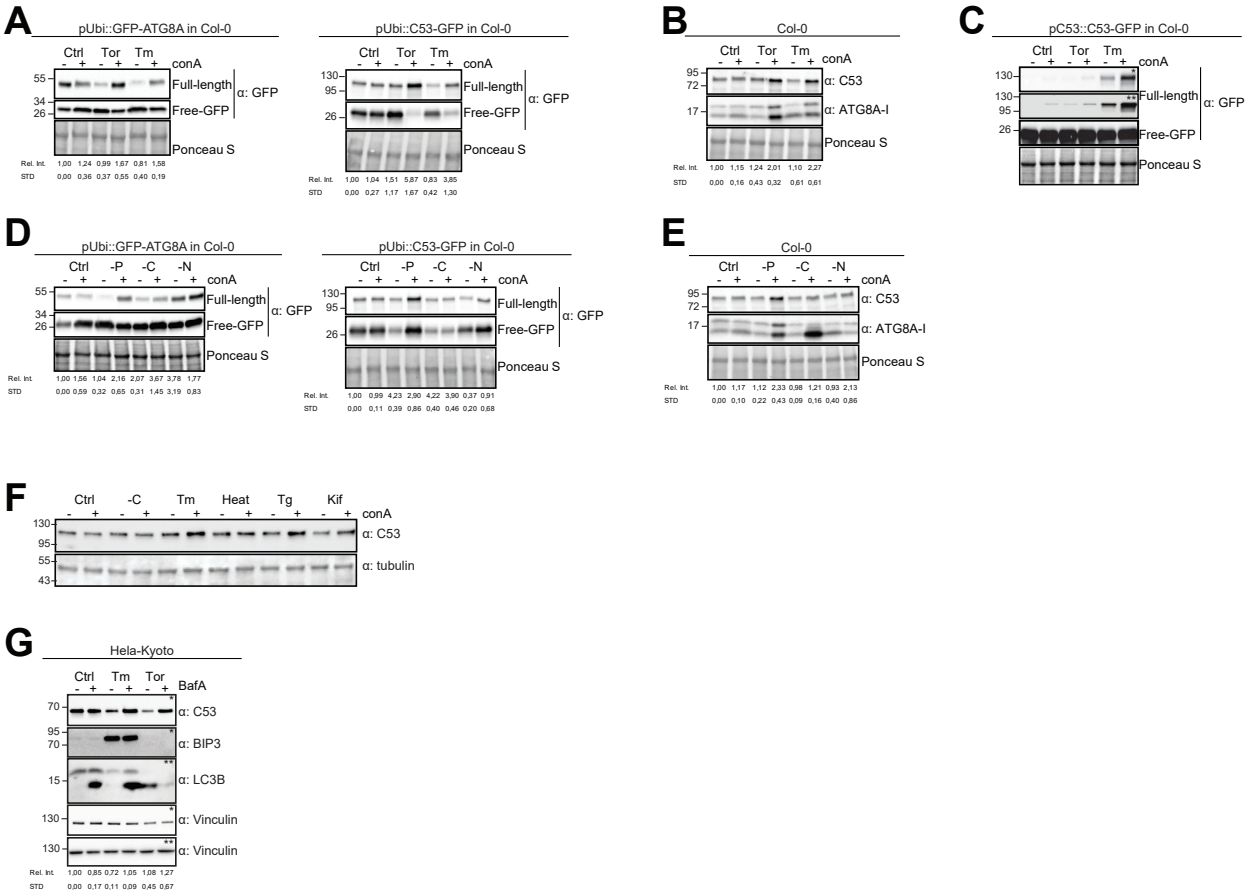
A
pUbi::GFP-ATG8A in Col-0
Ctrl Tor Tm
conA
55
34
26
Full-length
Free-GFP
α: GFP
Ponceau S
Rel. Int. 1,00 1,24 0,99 1,67 0,81 1,58
STD 0,00 0,36 0,37 0,55 0,40 0,19
pUbi::C53-GFP in Col-0
Ctrl Tor Tm
conA
130
95
26
Full-length
Free-GFP
α: GFP
Ponceau S
Rel. Int. 1,00 1,04 1,51 5,87 0,83 3,85
STD 0,00 0,27 1,17 1,67 0,42 1,30
B
Col-0
Ctrl Tor Tm
conA
95
72
17
α: C53
α: ATG8A-I
Ponceau S
Rel. Int. 1,00 1,15 1,24 2,01 1,10 2,27
STD 0,00 0,16 0,43 0,32 0,61 0,61
C
pC53::C53-GFP in Col-0
Ctrl Tor Tm
conA
130
95
26
Full-length
Free-GFP
α: GFP
Ponceau S
D
pUbi::GFP-ATG8A in Col-0
Ctrl -P -C -N
conA
55
34
26
Full-length
Free-GFP
α: GFP
Ponceau S
Rel. Int. 1,00 1,56 1,04 2,16 2,07 3,67 3,78 1,77
STD 0,00 0,59 0,32 0,65 0,31 1,45 3,19 0,83
pUbi::C53-GFP in Col-0
Ctrl -P -C -N
conA
130
95
26
Full-length
Free-GFP
α: GFP
Ponceau S
Rel. Int. 1,00 0,99 4,23 2,90 4,22 3,90 0,37 0,91
STD 0,00 0,11 0,39 0,86 0,40 0,46 0,20 0,68
E
Col-0
Ctrl -P -C -N
conA
95
72
17
α: C53
α: ATG8A-I
Ponceau S
Rel. Int. 1,00 1,17 1,12 2,33 0,98 1,21 0,93 2,13
STD 0,00 0,10 0,22 0,43 0,09 0,16 0,40 0,86
F
Ctrl -C Tm Heat Tg Kif
conA
130
95
55
43
α: C53
α: tubulin
G
Hela-Kyoto
Ctrl Tm Tor
BafA
70
95
70
15
130
130
α: C53
α: BIP3
α: LC3B
α: Vinculin
α: Vinculin
Rel. Int. 1,00 0,85 0,72 1,05 1,08 1,27
STD 0,00 0,17 0,11 0,09 0,45 0,67

319 **Figure 2. Autophagic flux analysis of AtC53 and HsC53 show that C53 autophagic flux is induced**
320 **during ER stress. (A-C) AtC53 flux is induced by Torin and tunicamycin treatment. (A)** Autophagic
321 flux analysis of transgenic pUbi::AtC53-GFP (right panel) and pUbi::GFP-ATG8A (left panel) seedlings.
322 **(B)** Autophagic flux analysis of endogenous AtC53 and ATG8, using AtC53 and ATG8 antibodies,
323 respectively. **(C)** Autophagic flux analysis of transgenic pAtC53::AtC53-GFP seedlings. Col-0 or
324 transgenic seedlings were incubated in control media or media containing 9 µM Torin1 (Tor) or 10 µg/ml
325 tunicamycin (Tm). In addition, each treatment was supplied with 1 µm concanamycin A (conA) to visualize
326 vacuolar degradation. Representative Western blots are displayed. Full-length and free GFP-bands from the
327 same blot were separated due to different exposure times. In (C), * and ** correspond to short and long
328 exposures of the same blot, respectively. Quantification of the relative intensities (Rel. Int.) of the protein
329 bands were normalized for the total protein level of the lysate (Ponceau S). Average C53 levels and SD for
330 n = 3 are shown. **(D-E) AtC53 flux is specifically induced upon phosphate starvation. (D)** Autophagic
331 flux analysis of transgenic pUbi::AtC53-GFP (right panel) and pUbi::GFP-ATG8A (left panel) seedlings
332 under carbon, nitrogen, and phosphate starvation conditions. **(E)** Autophagic flux analysis of endogenous
333 AtC53 and ATG8, using AtC53 and ATG8 antibodies, respectively. Col-0 or transgenic seedlings were
334 incubated in control media or media depleted with sucrose (-C), nitrogen (-N) or phosphate (-P). In addition,
335 each treatment was supplied with 1 µm concanamycin A (conA) to visualize vacuolar degradation.
336 Representative Western blots are displayed. Full-length and free GFP-bands from the same blot were
337 separated due to different exposure times. Quantification of the relative intensities (Rel. Int.) of the protein
338 bands were normalized for the total protein level of the lysate (Ponceau S). Average C53 levels and SD for
339 n = 3 are shown. **(F) AtC53 autophagic flux is induced by various ER stress inducing conditions.**
340 Western blot analysis of Arabidopsis transgenic seedlings expressing AtC53-GFP incubated in either
341 control (Ctrl), sucrose -deficient medium (-C), 10 µg/ml tunicamycin (Tm), 3 h at 37°C (Heat), 2.5 µM
342 Thapsigargin (Tg), or 50 µM Kifunensine (Kif). In addition, each treatment was supplied with 1 µm
343 concanamycin A (conA) to visualize vacuolar degradation. (**G) HsC53 flux is induced by Torin and**
344 **tunicamycin treatment.** Western blot analysis of HeLa whole cell lysates. Cells were either left untreated
345 or treated for 16 h with 2.5 µg/ml tunicamycin (Tm) or 1.5 µM Torin (Tor) and subsequently given a

346 recovery period of 2 h in presence or absence of 100 nM Bafilomycin A1 (BAF). C53 and BIP3 blots were
347 run on 4-20% gradient gels and transferred to nitrocellulose membranes, LC3B blots were run on 15% gels
348 and transferred to PVDF membranes. (* or ** indicate corresponding membranes). Quantification of the
349 relative intensities (Rel. Int.) of the protein bands were normalized for the total protein level of the lysate
350 (Vinculin). Average C53 levels and SD for n = 3 are shown.

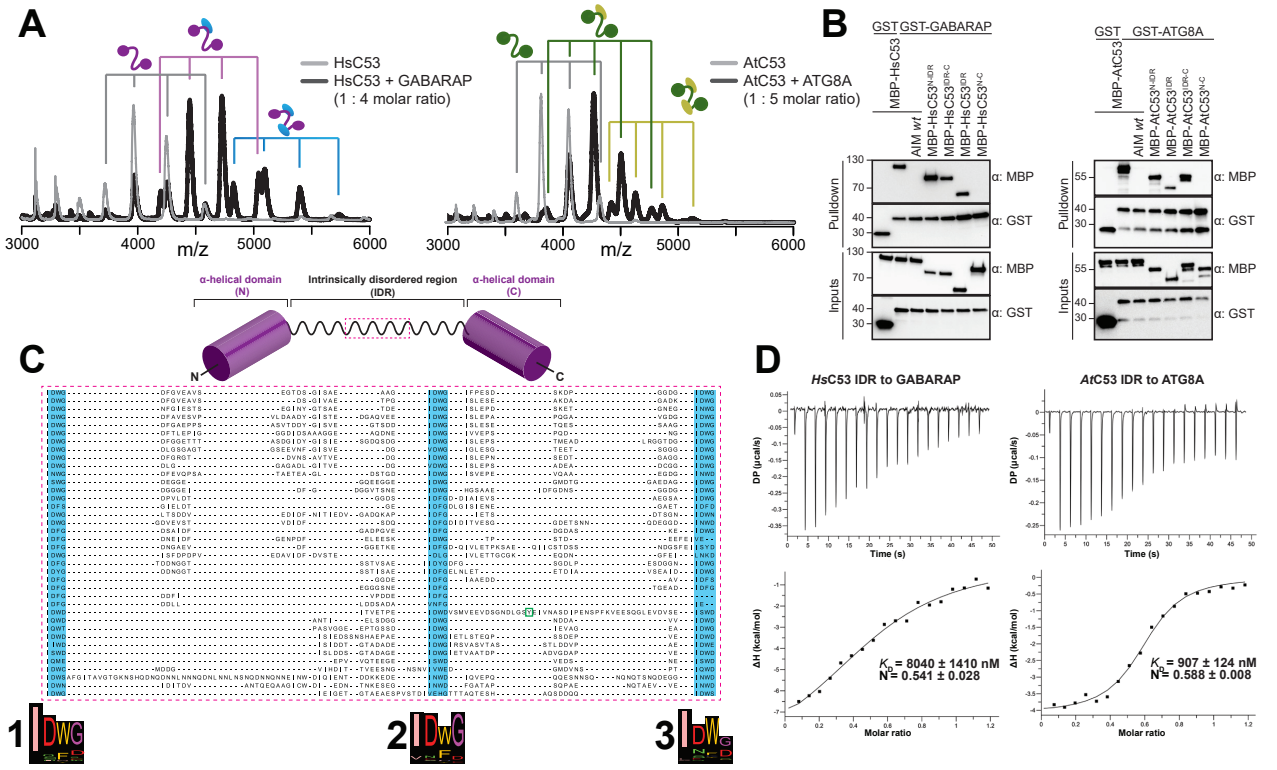
A
HsC53
HsC53 + GABARAP
(1 : 4 molar ratio)
AtC53
AtC53 + ATG8A
(1 : 5 molar ratio)
m/z
B
GST GST-GABARAP
GST GST-ATG8A
Pulldown
Inputs
α: MBP
α: GST
C
α-helical domain (N)
Intrinsically disordered region (IDR)
α-helical domain (C)
D
HsC53 IDR to GABARAP
AtC53 IDR to ATG8A
Time (s)
Molar ratio
ΔH (kcal/mol)
DP (µcal/s)
K_D = 8040 ± 1410 nM
N = 0.541 ± 0.028
K_D = 907 ± 124 nM
N = 0.588 ± 0.008

1
2
3

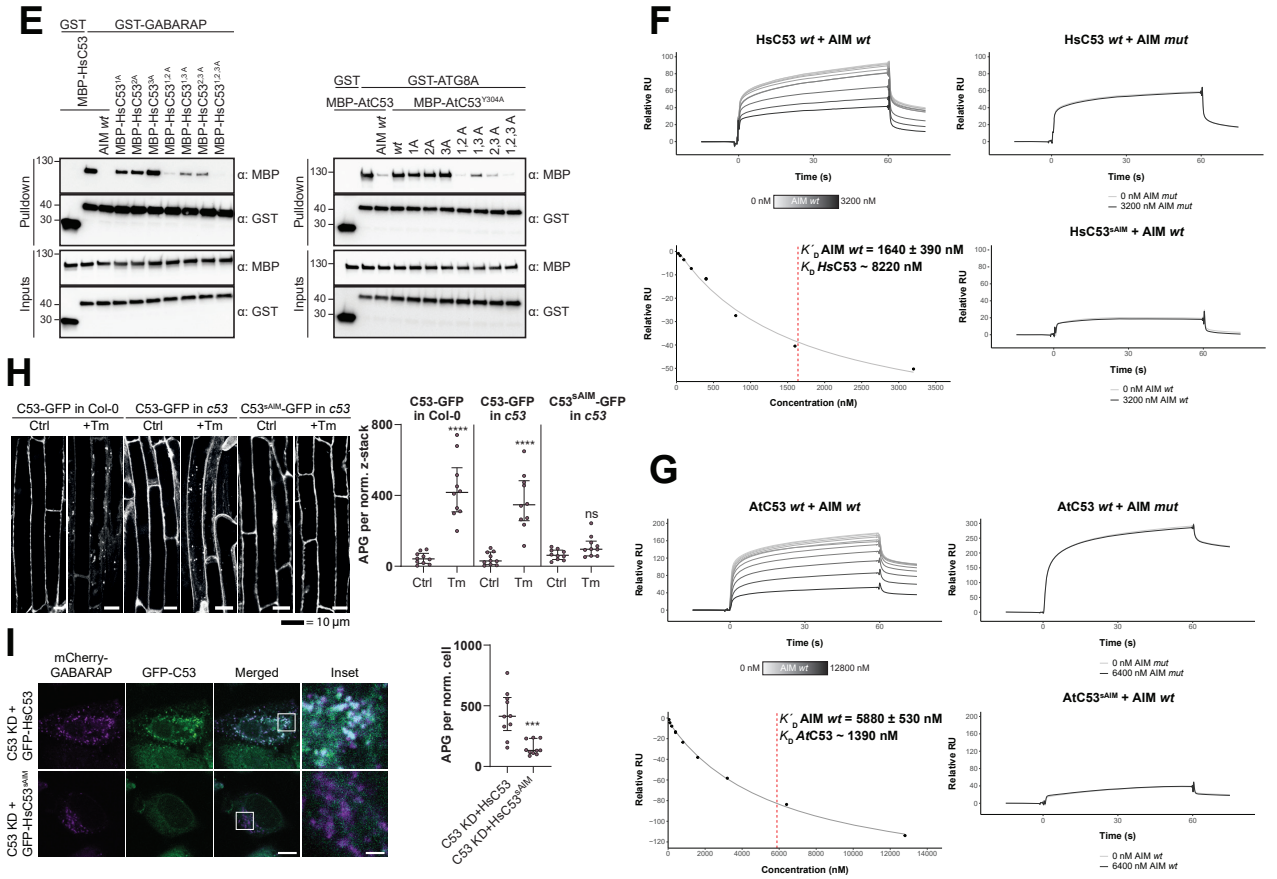
E
GST GST-GABARAP
GST GST-ATG8A
MBP-HsC53
MBP-AtC53
MBP-AtC53Y304A
Pulldown
Inputs
α: MBP
α: GST
F
HsC53 wt + AIM wt
HsC53 wt + AIM mut
HsC53sAIM + AIM wt
Relative RU
Time (s)
Concentration (nM)
K´D AIM wt = 1640 ± 390 nM
KD HsC53 ~ 8220 nM
G
AtC53 wt + AIM wt
AtC53 wt + AIM mut
AtC53sAIM + AIM wt
K´D AIM wt = 5880 ± 530 nM
KD AtC53 ~ 1390 nM
H
C53-GFP in Col-0
C53-GFP in c53
C53sAIM-GFP in c53
Ctrl
+Tm
APG per norm. z-stack
= 10 µm
I
mCherry-GABARAP
GFP-C53
Merged
Inset
C53 KD + GFP-HsC53
C53 KD + GFP-HsC53sAIM
APG per norm. cell
C53 KD+HsC53
C53 KD+HsC53sAIM

351 **Figure 3. C53 interacts with ATG8 via shuffled ATG8 interacting motifs (sAIMs).** (**A**) **Native mass**
352 **spectrometry (nMS) analysis showing HsC53 and AtC53 form 1:1 and 1:2 complexes with**
353 **GABARAP and ATG8A, respectively**. Left; nMS of HsC53 (grey) and HsC53 plus GABARAP in a 1:4
354 molar ratio (black). Peaks corresponding to unbound HsC53, the 1:1 complex and 1:2 complex are indicated
355 with grey, magenta and blue, respectively. Right; nMS of AtC53 (grey) and AtC53 plus ATG8A in a 1:5
356 molar ratio (black). Peaks corresponding to unbound AtC53, the 1:1 complex and 1:2 complex are indicated
357 with grey, green and yellow, respectively. Full spectra are shown in Figure S9. (**B**) ***Left Panel,* HsC53**
358 **intrinsically disordered region (IDR) is necessary and sufficient to mediate the interaction with**
359 **GABARAP. *Right Panel*, AtC53 IDR is necessary and sufficient to mediate the interaction with**
360 **ATG8A.** Bacterial lysates containing recombinant protein were mixed and pulled down with glutathione
361 magnetic agarose beads. The AIM *wt* peptide was added at a final concentration of 200 µM. Input and
362 bound proteins were visualized by immunoblotting with anti-GST and anti-MBP antibodies. N: N-terminal
363 truncation; M: IDR; C: C-terminal truncation. **(C) C53 IDR has three highly conserved regions.** Protein
364 sequence alignment of the predicted IDR amino acid sequences showed three highly conserved regions
365 with a consensus sequence of IDWG (highlighted in blue). Y304 is highlighted in the green rectangle. The
366 species names and the full protein sequence alignment is presented in Figure S10. (**D**) **Isothermal titration**
367 **calorimetry (ITC) experiments showing binding of *At*C53 and *Hs*C53 IDRs to ATG8A and**
368 **GABARAP, respectively.** Upper left and right panels show heat generated upon titration of *At*C53 IDR
369 (250 µM) or *Hs*C53 IDR (250 µM) to ATG8A or GABARAP (both 40 µM). Lower left and right panels
370 show integrated heat data (■) and the fit (solid line) to a one-set-of-sites binding model using PEAQ-ITC
371 analysis software. Representative values of K_D, N, ΔH, -TΔS, and ΔG from three independent ITC
372 experiments are reported in Table S5. (**E**) ***Left Panel,* the three conserved IDWG motifs (sAIMs) in**
373 ***Hs*C53 IDR mediate interaction with GABARAP.** Pull downs were performed as described in (b). 1A:
374 W269A; 2A: W294A; 3A: W312A. ***Right Panel*, *At*C53 quadruple mutant cannot interact with**
375 **ATG8A. In addition to the sAIM motifs, a canonical AIM (304-YEIV) also contributes to ATG8**
376 **binding.** Pull downs were performed as described in (b). 1A: W276A; 2A: W287A; 3A: W335A. (**F, G**)
377 **Surface plasmon resonance (SPR) analyses of C53-ATG8 binding.** GST-GABARAP or GST-ATG8A
378 fusion proteins were captured on the surface of the active cell (500 RU) and GST alone was captured on
379 the surface of the reference cell (300 RU). *Upper Left Panels:* Increasing concentrations of the AIM *wt*
380 peptide were premixed with 10 µM C53 and injected onto the sensor surface. Binding curves were obtained
381 by subtracting the reference cell signal from the active cell signal. *Lower left Panels*: Binding affinities
382 were determined by plotting the maximum response units versus the respective concentration of the AIM
383 *wt* peptide and the data were fitted using the Biacore T200 Evaluation software 3.1 (GE Healthcare). *Upper*
384 *Right Panels:* C53 was premixed with buffer or 3600 nM of AIM *mut* peptide and injected onto the sensor
385 surface. *Lower Right Panels:* $C53^{sAIM}$ was premixed with buffer or 3600 nM of AIM wt peptide and injected

386 onto the sensor surface. A representative sensorgram from three independent experiments is shown. (**H**)
387 ***At*C53 quadruple mutant (sAIM) does not form puncta upon ER-stress.** *Left Panel*, representative
388 confocal images of transgenic Arabidopsis seedlings expressing AtC53-GFP or AtC53^{sAIM}-GFP in Col-0
389 wild type and *c53* mutant backgrounds. 4-day old seedlings were incubated in either control or tunicamycin
390 (10 µg/ml) containing media. Scale bars, 10 µm. *Right Panel*, Quantification of autophagosomes (APG)
391 per normalized Z-stacks. Bars represent the mean (± SD) of at least 10 biological replicates. **(I) *Hs*C53**
392 **sAIM mutant does not form puncta upon ER-stress.** *Left Panel,* Confocal images of PFA fixed C53
393 knockdown HeLa cells transiently expressing *Hs*C53-GFP or *Hs*C53^{sAIM}-GFP (green) and mCherry-
394 GABARAP (magenta). Cells were treated for 16 h with 2.5 µg/ml tunicamycin (Tm). Scale bar, 10 µm.
395 Inset scale bar, 2 µm. Representative images are shown. *Right Panel,* Quantification of autophagosomes
396 (APG) per normalized cell. Bars represent the mean (± SD) of at least 10 biological replicates. Significant
397 differences are indicated with * when p value ≤ 0.05, ** when p value ≤ 0.01, and *** when p value ≤
398 0.001.
399

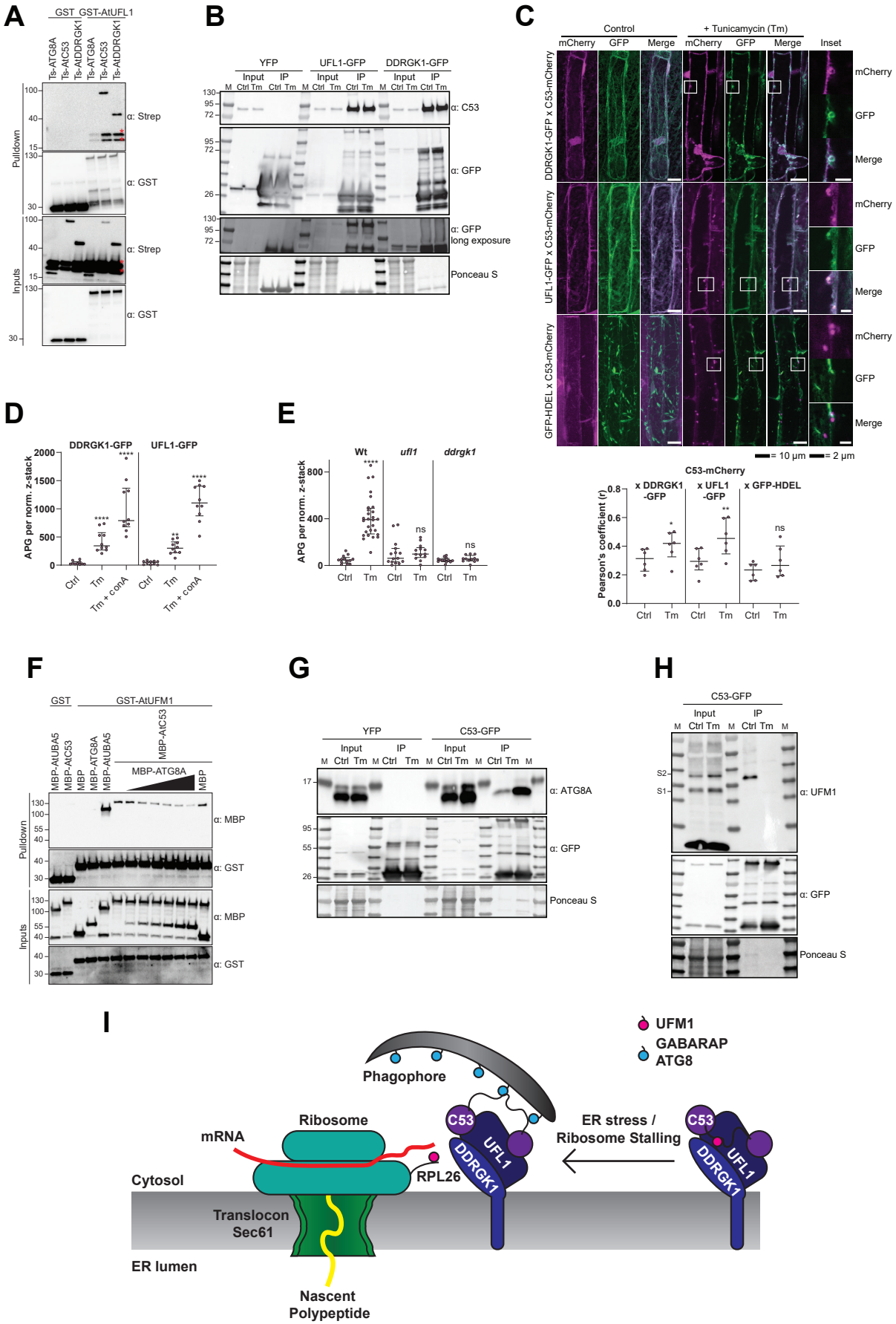
A
GST
GST-AtUFL1
Ts-ATG8A
Ts-AtC53
Ts-AtDDRGK1
Pulldown
Inputs
α: Strep
α: GST
B
YFP
UFL1-GFP
DDRGK1-GFP
Input
IP
α: C53
α: GFP
α: GFP long exposure
Ponceau S
C
Control
+ Tunicamycin (Tm)
mCherry
GFP
Merge
Inset
DDRGK1-GFP x C53-mCherry
UFL1-GFP x C53-mCherry
GFP-HDEL x C53-mCherry
= 10 µm
= 2 µm
C53-mCherry
x DDRGK1 -GFP
x UFL1 -GFP
x GFP-HDEL
Pearson's coefficient (r)
D
DDRGK1-GFP
UFL1-GFP
APG per norm. z-stack
Ctrl
Tm
Tm + conA
E
Wt
ufl1
ddrgk1
F
GST
GST-AtUFM1
MBP-AtUBA5
MBP-AtC53
MBP
MBP-ATG8A
MBP-AtUBA5
MBP-AtC53
MBP-ATG8A
α: MBP
G
YFP
C53-GFP
α: ATG8A
α: GFP
Ponceau S
H
C53-GFP
S2
S1
α: UFM1
I
UFM1
GABARAP
ATG8
Phagophore
Ribosome
mRNA
C53
UFL1
DDRGK1
RPL26
Cytosol
Translocon
Sec61
ER lumen
Nascent
Polypeptide
ER stress /
Ribosome Stalling

400 **Figure 4. C53 forms a tripartite receptor complex and is activated by depletion of UFM1 during ER**
401 **stress. (A) AtUFL1 interacts with AtC53 and AtDDRGK1.** Bacterial lysates containing recombinant
402 protein were mixed and pulled down with glutathione magnetic agarose beads. Input and bound proteins
403 were visualized by immunoblotting with anti-GST and anti-Strep antibodies. Red asterisks indicate
404 endogenous *E. coli* biotinylated proteins **(B) AtC53 associates with AtUFL1 and AtDDRGK1.** *In vivo*
405 co-immunoprecipitation of UFL1-GFP or DDRGK1-GFP expressing Arabidopsis seedlings incubated in
406 either control (Ctrl) or 10 µg/ml tunicamycin (Tm) containing media. **(C) AtDDRGK1 and AtUFL1**
407 **colocalize with AtC53 puncta upon ER stress induction.** *Left Upper Panel*, Co-localization analyses of
408 confocal micrographs of wild type Col-0 roots co-expressing AtC53-mCherry (magenta) with DDRGK1-
409 GFP, UFL1-GFP, or GFP-HDEL (green). Transgenic seedlings were incubated in either control or
410 tunicamycin (10 µg/ml) containing media. Representative confocal images of control conditions are shown
411 in maximum projection to emphasize ER association. Images of tunicamycin treatments are shown in single
412 plane. Scale bars, 10 µm. Inset scale bars, 2 µm. *Left Lower Panel*, Pearson's Coefficient colocalization
413 analysis per normalized Z-scan. Bars represent the mean (± SD) of 5 biological replicates. **(D) DDRGK1**
414 **and UFL1 undergo vacuolar degradation upon ER stress induction.** Quantification of confocal
415 micrographs of autophagic flux of UFL1-GFP and DDRGK1-GFP. Seedlings were incubated in either
416 control, 10 µg/ml tunicamycin (Tm), or 10 µg/ml tunicamycin with 1 µM Concanamycin A (Tm+ConA)
417 media. Quantification of autophagosomes (APG) per normalized Z-stacks of UFL1-GFP and DDRGK1-
418 GFP. Bars represent the mean (± SD) of at least 10 biological replicates. **(E) AtC53 vacuolar degradation**
419 **requires DDRGK1 and UFL1.** Quantification of confocal images of Wildtype (Wt), *ufl1*, and *ddrgk1*
420 Arabidopsis seedlings expressing AtC53-mCherry. 6-day old seedlings were incubated in either control
421 (Ctrl) or 10 µg/ml tunicamycin (Tm) containing media. Scale bars, 20 µm. Quantification of
422 autophagosomes (APG) per normalized Z-stacks. Bars represent the mean (± SD) of at least 10 biological
423 replicates. Significant differences compared to control treatment (Ctrl) are indicated with * when p value ≤
424 0.05, ** when p value ≤ 0.01, and *** when p value ≤ 0.001. **(F) AtUFM1 directly interacts with UFM1**
425 **and this interaction becomes weaker upon increasing concentrations of ATG8A.** Bacterial lysates
426 containing recombinant protein were mixed and pulled down with glutathione magnetic agarose beads.
427 Input and bound proteins were visualized by immunoblotting with anti-GST and anti-MBP antibodies. The
428 red asterisk indicates MBP-ATG8A. **(G) AtC53-ATG8 association becomes stronger upon ER stress**
429 **induction triggered by tunicamycin.** *In vivo* co-immunoprecipitation of extracts of Arabidopsis seedlings
430 expressing AtC53-GFP incubated in either control (Ctrl) or 10 µg/ml tunicamycin (Tm) containing media.
431 **(H) AtC53-UFM1 association becomes weaker upon ER stress induction triggered by tunicamycin.**
432 *In vivo* pull downs of extracts of Arabidopsis seedlings expressing C53-GFP incubated in either control
433 (Ctrl) or 10 µg/ml tunicamycin (Tm) containing media. Input and bound proteins were visualized by
434 immunoblotting with the indicated antibodies. **(I) Current working model of the C53 receptor complex.**

435 Upon ribosome stalling, UFM1 is transferred from the C53 receptor complex to the tail of RPL26, exposing
436 the sAIMs on C53 for ATG8 binding and subsequent recruitment to the autophagosomes.
437
438
439
440

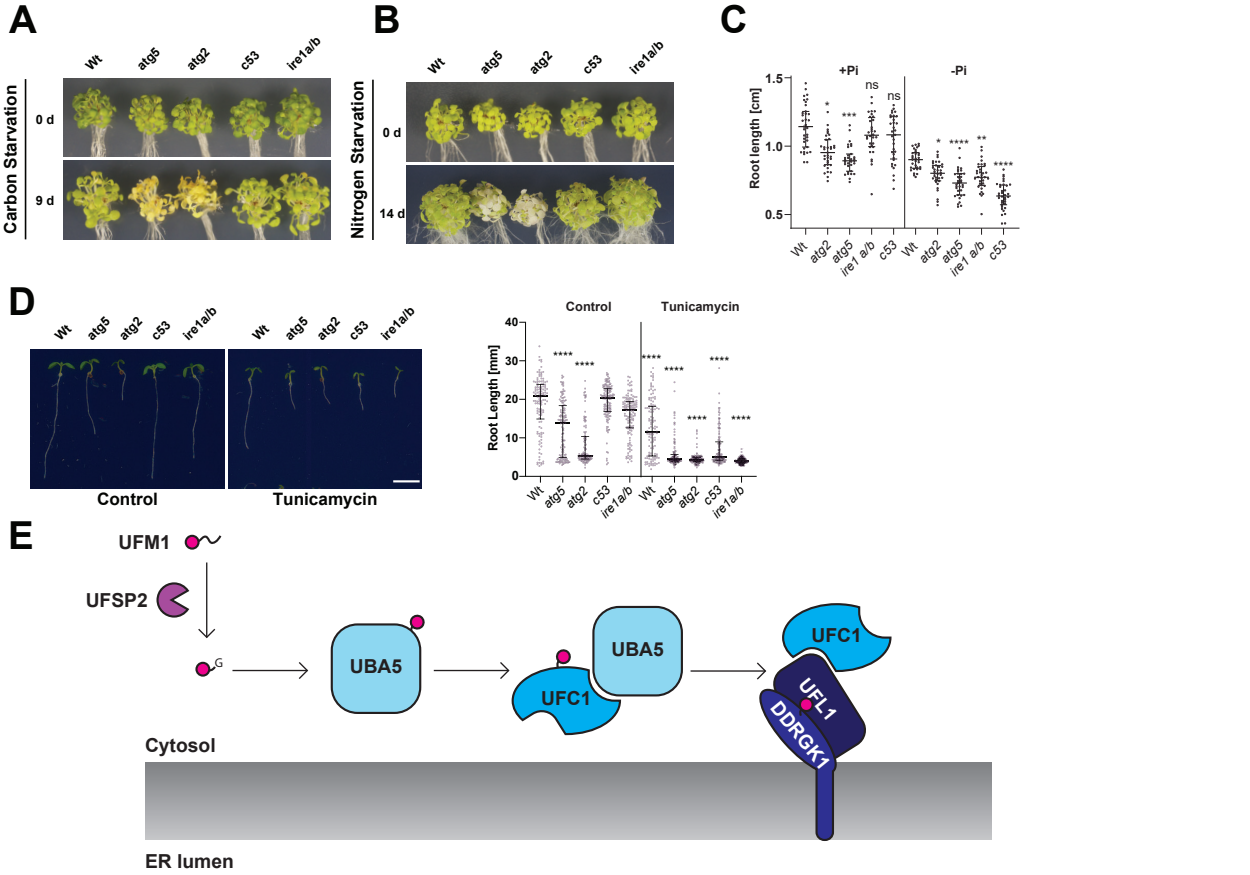
A
Wt
atg5
atg2
c53
ire1a/b
Carbon Starvation
0 d
9 d
B
Nitrogen Starvation
14 d
C
+Pi
-Pi
Root length [cm]
D
Control
Tunicamycin
Root Length [mm]
E
UFM1
UFSP2
UBA5
UFC1
UFL1
DDRGK1
Cytosol
ER lumen
F
ufm1
ddrgk1
ufl1
ufc1
uba5
ufsp2
G
AtC53-GFP in c53

441 **Figure 5. C53 is crucial for ER stress tolerance.** (**A**) ***Atc53*** **mutant is insensitive to carbon starvation.**
442 Phenotypes before (0 d) and after 9 days carbon starvation (9 d) of seven-day-old seedlings, n ≥ 20 seedlings
443 per genotype. (**B**) ***Atc53*** **mutant is insensitive to nitrogen starvation.** Phenotypes before (0 d) and after
444 14 days nitrogen starvation (14 d) of seven-day-old seedlings, n ≥ 20 seedlings per genotype. **(C)** ***Atc53***
445 **mutant is sensitive to phosphate starvation.** Root-length quantification of seven-day-old seedlings which
446 were transferred to media with or without Pi supplement (+Pi, -Pi), and imaged after 2 days. (**D**) **Atc53**
447 **mutants are sensitive to ER stress induced by tunicamycin**. Root-length quantification of 7-day old
448 seedlings grown on half strength MS media without sucrose treated with 100 ng/mL tunicamycin (Tm).
449 Bottom Panel, Root-length quantification of 7-day old seedlings. n≈125 seedlings per genotype and
450 treatment. *Left Panel*, Example of 7-day old seedlings grown in described conditions. Scale bars = 5 mm.
451 Left, non-treated seedlings. Right, seedlings grown at 100 ng/mL Tm. *Right Panel,* Root length of each
452 genotype was compared pairwise with the wildtype (Col-0) for each specific treatment condition. **(E) Main**
453 **molecular players in the ufmylation pathway.** UFSP2: UFM1 specific protease 2 that matures UFM1,
454 exposing the terminal glycine residue. UBA5: the E1 activating enzyme, UFC1: E2 conjugating enzyme,
455 UFL1: E3 ligase (**F**) **Ufmylation pathway mutants are sensitive to ER stress triggered by tunicamycin.**
456 Root length quantification of 7-day old seedlings grown on half strength MS media without sucrose treated
457 with 100 ng/mL tunicamycin (Tm). *Left panel,* Root length quantification of 7-day old seedlings. n≈100
458 seedlings per genotype and treatment. *Right Panel,* Representative images of 7-day old seedlings grown in
459 described conditions. Scale bars, 5 mm. To the left are non-treated seedlings, to the right are seedlings
460 grown at 100 ng/mL Tm. **(G) AtC53^{sAIM} mutant does not complement tunicamycin sensitivity**
461 **phenotype.** Root length quantification of indicated 7-d old seedlings grown on half strength MS media
462 without sucrose in control conditions (Ctrl) or treated with 100 ng/mL tunicamycin (Tm). T1 transgenic
463 lines were used. n=12 seedlings per genotype and treatment. Data represent the median with its interquartile
464 range. Root length of each genotype was compared pairwise with the wildtype (Col-0) for each treatment
465 condition. Significant differences compared to control treatment (Ctrl) are indicated with * when p value ≤
466 0.05, ** when p value ≤ 0.01, and *** when p value ≤ 0.001.
467
468
469
470
471
472
473
474
475

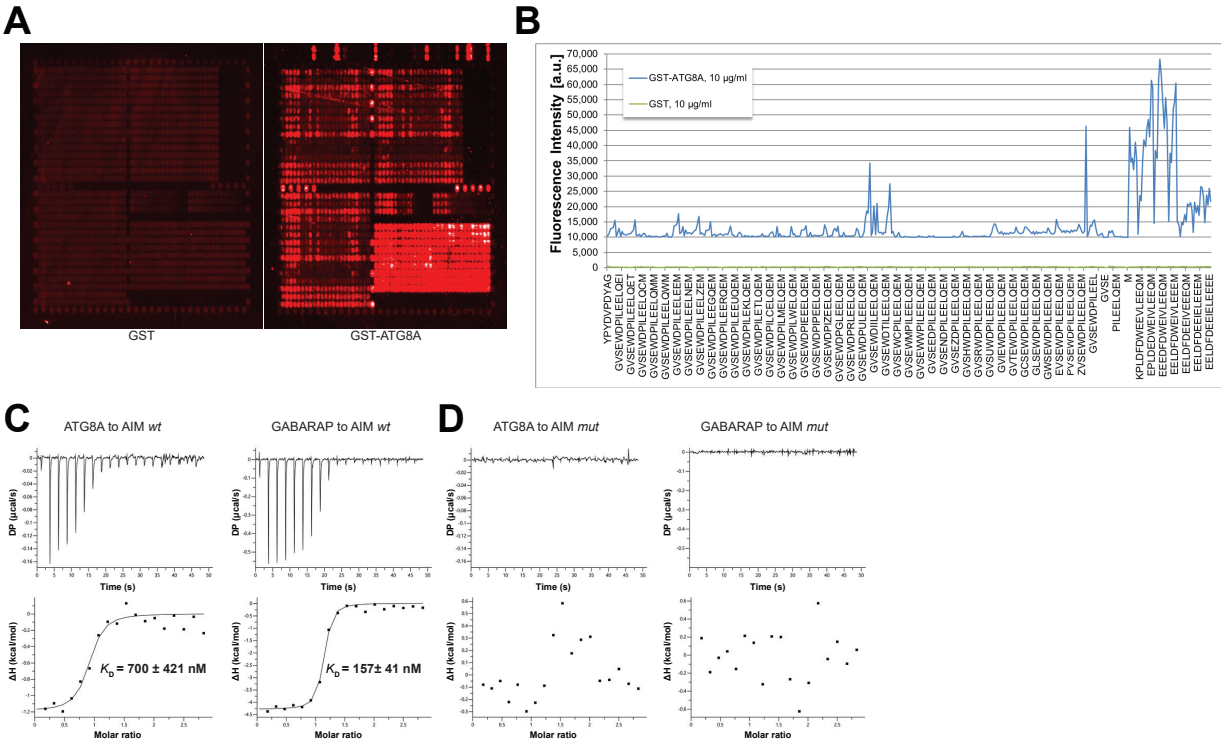
A
GST
GST-ATG8A
B
GST-ATG8A, 10 µg/ml
GST, 10 µg/ml
Fluorescence Intensity [a.u.]
C
ATG8A to AIM wt
GABARAP to AIM wt
D
ATG8A to AIM mut
GABARAP to AIM mut
DP (µcal/s)
Time (s)
ΔH (kcal/mol)
Molar ratio
K_D = 700 ± 421 nM
K_D = 157± 41 nM

479 **Figure S1. Identification of high affinity AIM peptides for peptide competition coupled**
480 **immunoprecipitation mass spectrometry and *in vitro* pull-down experiments. (a) Qualitative analysis**
481 **of peptide array results.** A library of ATG8-interacting motif peptides (See Table S1), were spotted onto
482 an array and incubated with GST or GST-ATG8A. **(b) Quantification of peptide array results for**
483 **selected AIM peptides.** The AIM peptide (AIM *wt*) (EEEDFDWEIVLEEEM) showed the highest
484 fluorescence intensity. **(c) Isothermal titration calorimetry (ITC) experiments showing binding of AIM**
485 ***wt* to ATG8A and GABARAP.** Upper left and right panels show heat generated upon titration of AIM *wt*
486 (600 μM) to ATG8A or GABARAP (both 40 μM). Lower left and right panels show integrated heat data
487 (■) and the fit (solid line) to a one-set-of-sites binding model using PEAQ-ITC analysis software.
488 Representative values of K_D, N, ΔH, -TΔS and ΔG from three independent ITC experiments are reported in
489 Table S5. **(d) Isothermal titration calorimetry (ITC) experiments showing that the AIM mutant**
490 **peptide (AIM *mut*) (EEEDFDAEIALEEEM) cannot bind to ATG8A or GABARAP.** Upper left and
491 right panels show heat generated upon titration of *AIM mut* (600 μM) to ATG8A or GABARAP (both 40
492 μM). Lower left and right panels show integrated heat data (■) from PEAQ-ITC analysis software.

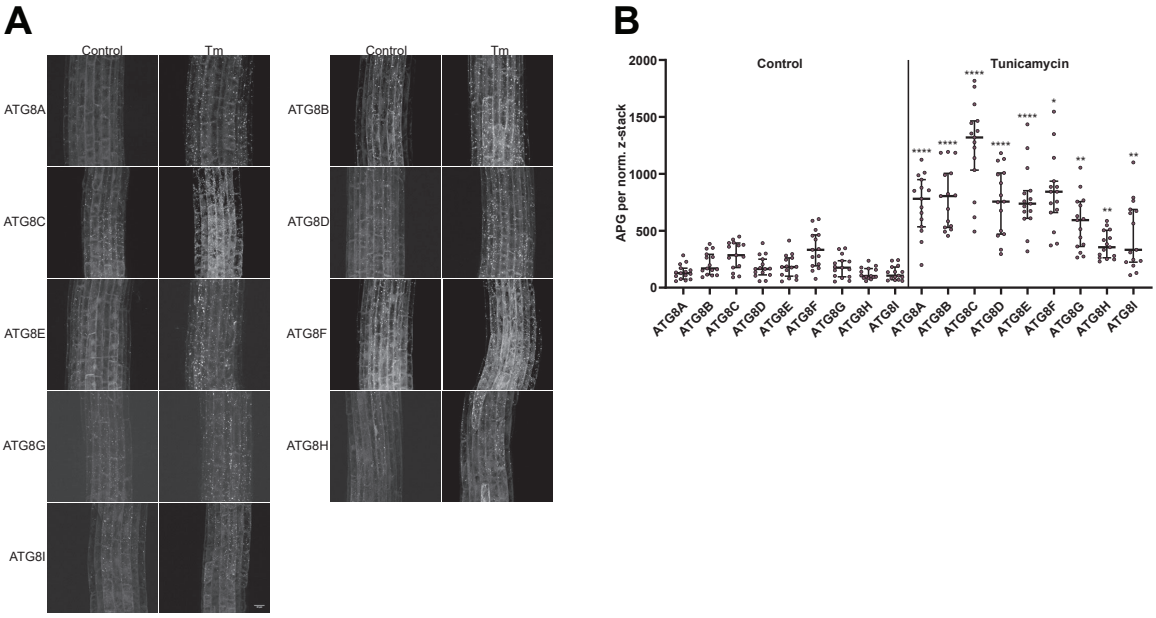
A
Control
Tm
ATG8A
ATG8B
ATG8C
ATG8D
ATG8E
ATG8F
ATG8G
ATG8H
ATG8I
B
Control
Tunicamycin
APG per norm. z-stack
2000
1500
1000
500
0
ATG8A
ATG8B
ATG8C
ATG8D
ATG8E
ATG8F
ATG8G
ATG8H
ATG8I

493 **Figure S2. All** Arabidopsis **ATG8 isoforms are induced by tunicamycin-triggered ER stress. (a)**
494 Representative confocal images of transgenic Arabidopsis seedlings expressing GFP-ATG8A to I in Col-0
495 background. 6-day old seedlings were incubated in either control or tunicamycin (10 µg/ml) containing
496 media. **(b)** Quantification of the autophagosomes (APG) per normalized Z-stack. Bars represent the mean
497 (± SD) of at least 10 biological replicates. Significant differences between control and tunicamycin-treated
498 samples are indicated with * when p value ≤ 0.05, ** when p value ≤ 0.01, and *** when p value ≤ 0.001.
499

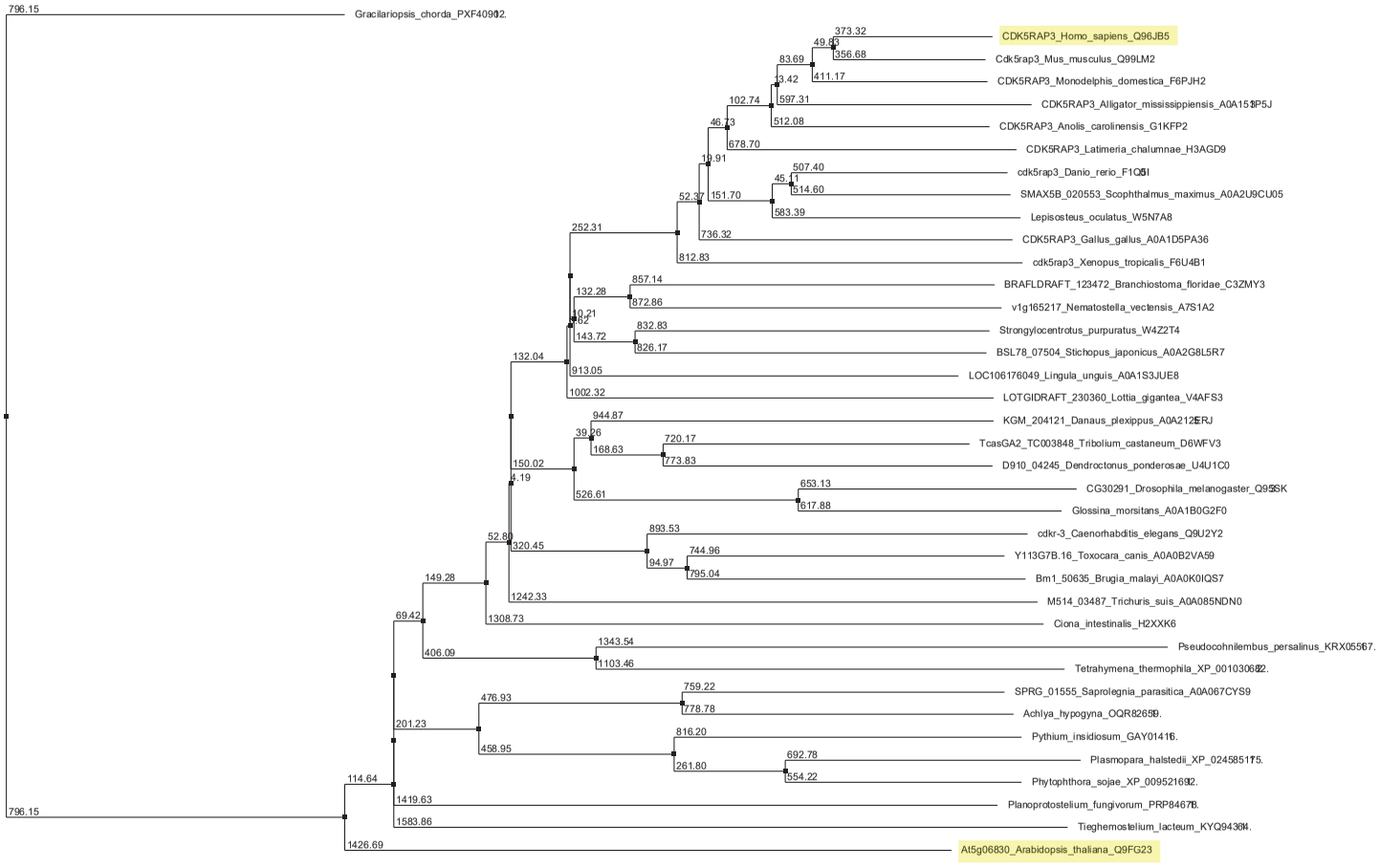
796.15
Gracilariopsis_chorda_PXF40902.
373.32
CDK5RAP3_Homo_sapiens_Q96JB5
49.83
356.68
Cdk5rap3_Mus_musculus_Q99LM2
83.69
411.17
CDK5RAP3_Monodelphis_domestica_F6PJH2
597.31
CDK5RAP3_Alligator_mississippiensis_A0A151P5J
102.74
512.08
CDK5RAP3_Anolis_carolinensis_G1KFP2
46.73
678.70
CDK5RAP3_Latimeria_chalumnae_H3AGD9
507.40
cdk5rap3_Danio_rerio_F1Q5I
45.11
514.60
SMAX5B_020553_Scophthalmus_maximus_A0A2U9CU05
52.37
151.70
583.39
Lepisosteus_oculatus_W5N7A8
736.32
CDK5RAP3_Gallus_gallus_A0A1D5PA36
812.83
cdk5rap3_Xenopus_tropicalis_F6U4B1
252.31
857.14
BRAFLDRAFT_123472_Branchiostoma_floridae_C3ZMY3
132.28
872.86
v1g165217_Nematostella_vectensis_A7S1A2
143.72
832.83
Strongylocentrotus_purpuratus_W4Z2T4
826.17
BSL78_07504_Stichopus_japonicus_A0A2G8L5R7
132.04
913.05
LOC106176049_Lingula_unguis_A0A1S3JUE8
1002.32
LOTGIDRAFT_230360_Lottia_gigantea_V4AFS3
944.87
KGM_204121_Danaus_plexippus_A0A212ERJ
39.26
720.17
TcasGA2_TC003848_Tribolium_castaneum_D6WFV3
168.63
773.83
D910_04245_Dendroctonus_ponderosae_U4U1C0
150.02
653.13
CG30291_Drosophila_melanogaster_Q9VSK
526.61
617.88
Glossina_morsitans_A0A1B0G2F0
893.53
cdkr-3_Caenorhabditis_elegans_Q9U2Y2
52.80
320.45
744.96
Y113G7B.16_Toxocara_canis_A0A0B2VA59
94.97
795.04
Bm1_50635_Brugia_malayi_A0A0K0IQS7
149.28
1242.33
M514_03487_Trichuris_suis_A0A085NDN0
69.42
1308.73
Ciona_intestinalis_H2XXK6
1343.54
Pseudocohnilembus_persalinus_KRX05567.
406.09
1103.46
Tetrahymena_thermophila_XP_001030622.
759.22
SPRG_01555_Saprolegnia_parasitica_A0A067CYS9
476.93
778.78
Achlya_hypogyna_OQR82659.
201.23
816.20
Pythium_insidiosum_GAY01416.
458.95
692.78
Plasmopara_halstedii_XP_024585175.
261.80
554.22
Phytophthora_sojae_XP_009521692.
114.64
1419.63
Planoprotostelium_fungivorum_PRP84678.
796.15
1583.86
Tieghemostelium_lacteum_KYQ94364.
1426.69
At5g06830_Arabidopsis_thaliana_Q9FG23

500 **Figure S3. Unrooted maximum likelihood phylogenetic tree of C53 homologs.** The tree was generated
501 from protein sequence alignments of C53 homologs from 38 species. The bootstrap support for each node
502 is indicated. The tree was calculated with Jalview 2.11.0 from distance matrices determined from aggregate
503 BLOSUM 62 scores using Average Distance (UPGMA) algorithm.
504
505

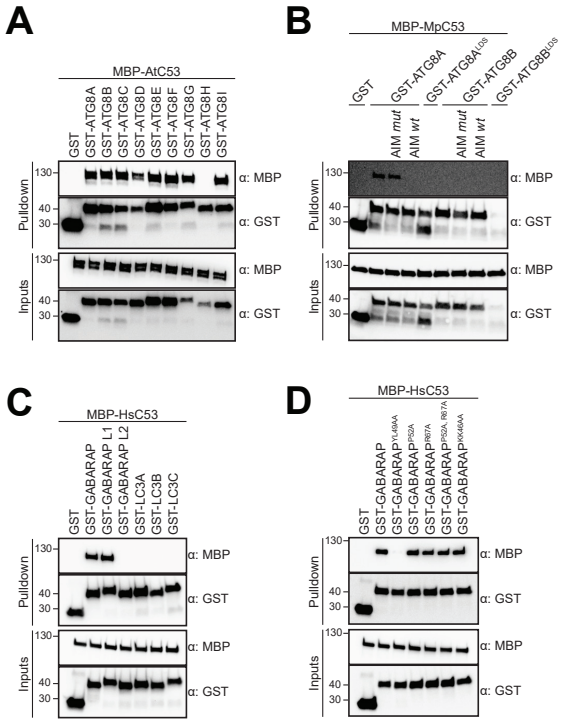
A
MBP-AtC53
GST
GST-ATG8A
GST-ATG8B
GST-ATG8C
GST-ATG8D
GST-ATG8E
GST-ATG8F
GST-ATG8G
GST-ATG8H
GST-ATG8I
Pulldown
Inputs
130
40
30
α: MBP
α: GST
B
MBP-MpC53
GST
GST-ATG8A
GST-ATG8A^LDS
GST-ATG8B
GST-ATG8B^LDS
AIM mut
AIM wt
AIM mut
AIM wt
Pulldown
Inputs
130
40
30
α: MBP
α: GST
C
MBP-HsC53
GST
GST-GABARAP
GST-GABARAP L1
GST-GABARAP L2
GST-LC3A
GST-LC3B
GST-LC3C
Pulldown
Inputs
130
40
30
α: MBP
α: GST
D
MBP-HsC53
GST
GST-GABARAP
GST-GABARAP^Y0,49AA
GST-GABARAP^P52A
GST-GABARAP^R67A
GST-GABARAP^P52A, R67A
GST-GABARAP^KK46AA
Pulldown
Inputs
130
40
30
α: MBP
α: GST

506 **Figure S4. C53 binds ATG8 isoforms from plants and humans in an AIM-dependent manner (a)**
507 **AtC53 interacts with AtATG8 in an isoform specific manner.** *In vitro* pull down with all ATG8 isoforms
508 of *Arabidopsis thaliana* (At) shows that AtC53 can interact with eight out of nine ATG8 isoforms. Bacterial
509 lysates containing recombinant protein were mixed and pulled down with glutathione magnetic agarose
510 beads. **(b) MpC53 interacts with MpATG8 isoforms in a specific manner.** *In vitro* pull down with both
511 ATG8 isoforms of *Marchantia polymorpha* (Mp) shows that MpC53 can interact with one out of two ATG8
512 isoforms. Bacterial lysates containing recombinant protein were mixed and pulled down with glutathione
513 magnetic agarose beads. Before MpC53 pull down, peptides AIM *wt* and AIM *mut* were added to a final
514 concentration of 200 µM. Input and bound proteins were visualized by immunoblotting with anti-GST and
515 anti-MBP antibodies. **(c) HsC53 interacts with GABARAP and GABARAP L1.** Bacterial lysates
516 containing recombinant protein were mixed and pulled down with glutathione magnetic agarose beads.
517 Input and bound proteins were visualized by immunoblotting with anti-GST and anti-MBP antibodies. **(d)**
518 **HsC53 interacts with GABARAP via the LIR Docking Site (LDS).** Mutating the W site to a YL49AA
519 mutation (Marshall et al., 2019) prevents binding of GABARAP to C53. However, mutating the L position
520 to P52A or R67A (Marshall et al., 2019), or mutating KK64AA (which mediates the interaction with the
521 atypical LIR motif found in UBA5 (Huber et al., 2019)) did not prevent C53 binding. Bacterial lysates
522 containing recombinant protein were mixed and pulled down with glutathione magnetic agarose beads.
523 Input and bound proteins were visualized by immunoblotting with anti-GST and anti-MBP antibodies.
524
525
526

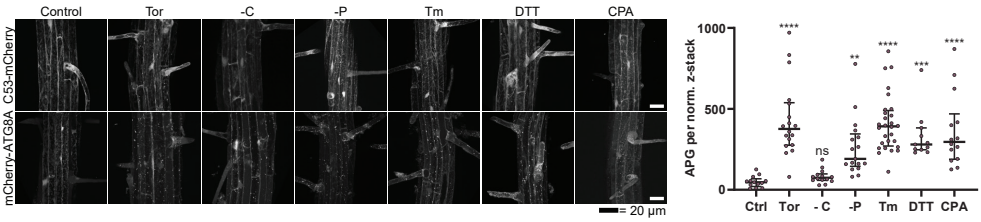
Control
Tor
-C
-P
Tm
DTT
CPA
C53-mCherry
mCherry-ATG8A
= 20 µm
APG per norm. z-stack
1000
500
0
****
ns
**
****
***
****
Ctrl
Tor
- C
-P
Tm
DTT
CPA

527 **Figure S5. Analysis of AtC53 puncta under various stress conditions revealed induction of C53**
528 **puncta upon ER stress.** *Left Panel*, representative confocal images of transgenic Arabidopsis seedlings
529 expressing C53-mCherry and mCherry-ATG8A in Col-0 background. 6-day old seedlings were incubated
530 in either control (Ctrl), sucrose deficient (-C), or phosphate deficient (-P) media, or media containing 9 µm
531 Torin1 (Tor), 10 µg/ml tunicamycin (Tm), 15 µM CPA, or 2.5 mM DTT. The TOR kinase inhibitor Torin
532 and ER stress inducing conditions -P, DTT, Tm, and CPA triggered formation of both C53 and ATG8
533 puncta, whereas carbon starvation only triggered ATG8 puncta. Scale bars, 20 µm. *Right Panel*,
534 Quantification of autophagosomes (APG) per normalized Z-stack. Bars represent the mean (± SD) of at
535 least 10 biological replicates. Significant differences compared to control treatment (Ctrl) are indicated with
536 * when p value ≤ 0.05, ** when p value ≤ 0.01, and *** when p value ≤ 0.00. ns=not significant.
537

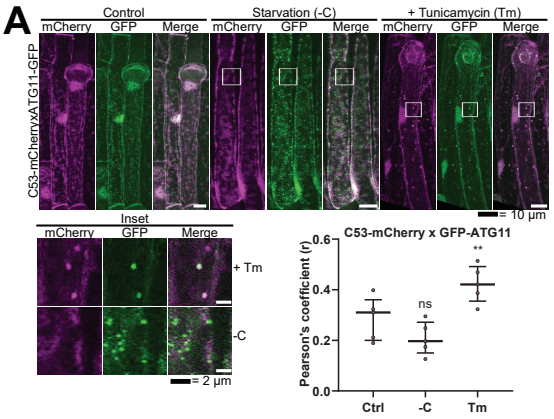
A
Control
Starvation (-C)
+ Tunicamycin (Tm)
mCherry
GFP
Merge
C53-mCherryxATG11-GFP
= 10 µm
Inset
+ Tm
-C
= 2 µm
C53-mCherry x GFP-ATG11
Pearson's coefficient (r)
0.6
0.4
0.2
0.0
ns
**
Ctrl
-C
Tm

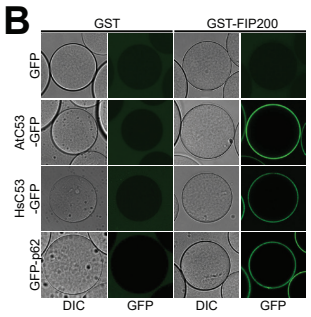
B
GST
GST-FIP200
GFP
AtC53 -GFP
HsC53 -GFP
GFP-p62
DIC
GFP
DIC
GFP

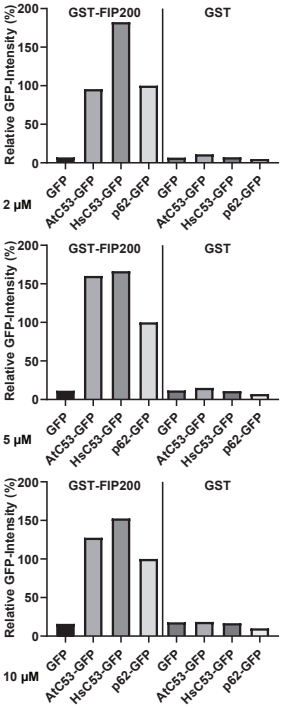
Relative GFP-Intensity (%)
200
150
100
50
0
GST-FIP200
GST
GFP
AtC53-GFP
HsC53-GFP
p62-GFP
2 µM
5 µM
10 µM

538 **Figure S6. C53 binds selective autophagy adaptor ATG11. (a) C53 puncta partially colocalize with**
539 **ATG11-GFP during ER stress**. *Upper Panel*, Co-localization analyses of single plane confocal images
540 obtained from transgenic Arabidopsis roots co-expressing C53-mCherry (magenta) with ATG11-GFP
541 (green). 4-day old seedlings were incubated in either control, sucrose deficient (-C), or 10 µg/ml
542 tunicamycin (Tm) containing media. Scale bars, 20 µm. *Lower Left Panel,* Inset Scale bar, 2 µm. *Lower*
543 *Right Panel*, Pearson's Coefficient (r) analysis of the colocalization of C53-mCherry with ATG11-GFP.
544 C53 only colocalized with ATG11 under ER stress treatments. Bars represent the mean (± SD) of at least 5
545 biological replicates. Significant differences are indicated with * when p value ≤ 0.05, ** when p value ≤
546 0.01, and *** when p value ≤ 0.001. ns= not significant **(b) AtC53 and HsC53 directly interact with**
547 **mammalian ATG11 homolog FIP200.** GSH beads were coated with GST or GST-FIP200. Excess GST
548 or GST-FIP200 was washed off, and beads were incubated with 2, 5 or 10 µM of recombinant GFP
549 (negative control), GFP-p62 (positive control), AtC53-GFP, or HsC53-GFP. Beads were equilibrated for 1
550 hour and imaged using a confocal microscope. *Right Panel*, Quantification of C53 binding to FIP200. The
551 graphs on the right show the average GFP intensity of beads n ≥ 15, normalized to the signal of GFP-p62.
552
553

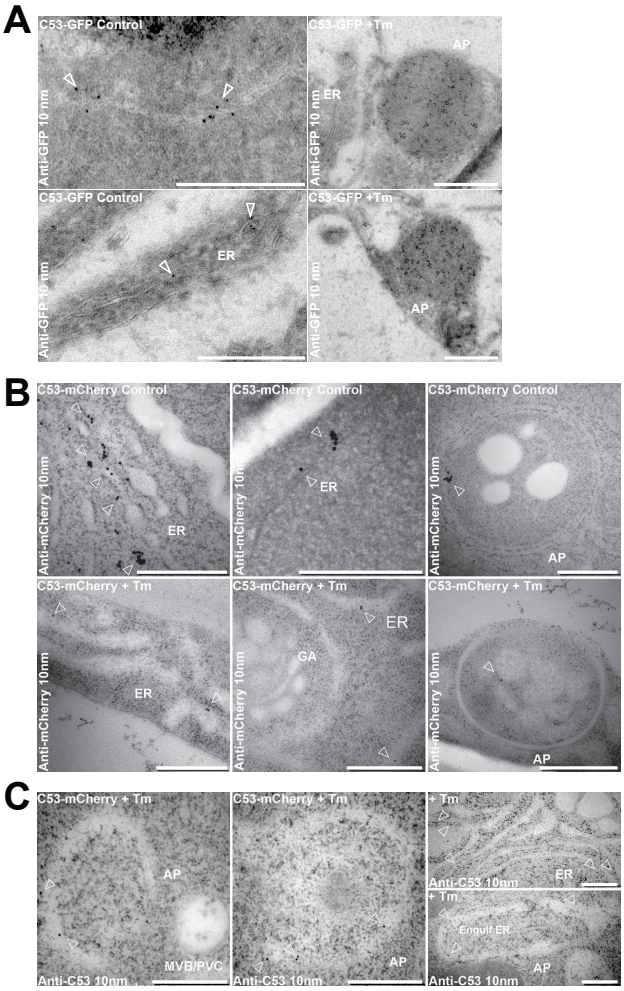
A
C53-GFP Control
Anti-GFP 10 nm
C53-GFP +Tm
AP
ER
Anti-GFP 10 nm
C53-GFP Control
ER
Anti-GFP 10 nm
C53-GFP +Tm
AP
Anti-GFP 10 nm
B
C53-mCherry Control
Anti-mCherry 10nm
ER
C53-mCherry Control
ER
C53-mCherry Control
Anti-mCherry 10nm
AP
C53-mCherry + Tm
Anti-mCherry 10nm
ER
C53-mCherry + Tm
ER
GA
Anti-mCherry 10nm
C53-mCherry + Tm
Anti-mCherry 10nm
AP
C
C53-mCherry + Tm
AP
MVB/PVC
Anti-C53 10nm
C53-mCherry + Tm
AP
Anti-C53 10nm
+ Tm
Anti-C53 10nm
ER
+ Tm
Engulf ER
AP
Anti-C53 10nm

554 **Figure S7. Electron micrographs showing that C53 localizes to the ER and autophagosomes during**
555 **ER stress. (a-c)** Immunogold labelling of high-pressure frozen, 5-day old *Arabidopsis* roots treated with
556 (Tm) or without (control) 10 µg/ml tunicamycin for 6 hours. Arrowheads indicate 10 nm gold particles.
557 Scale bars, 500 nm. **(a)** C53-GFP transgenic roots were prepared for immunogold electron microscopy
558 analysis using GFP antibody. **(b)** C53-mCherry transgenic roots were prepared for immunogold electron
559 microscopy analysis using RFP antibody. **(C)** Col-0 non-transgenic roots were prepared for immunogold
560 electron microscopy analysis using C53-antibody. ER= Endoplasmic reticulum, AP=autophagosome,
561 MVB/PVC=multivesicular body
562
563
564
565
566
567
568
569
570

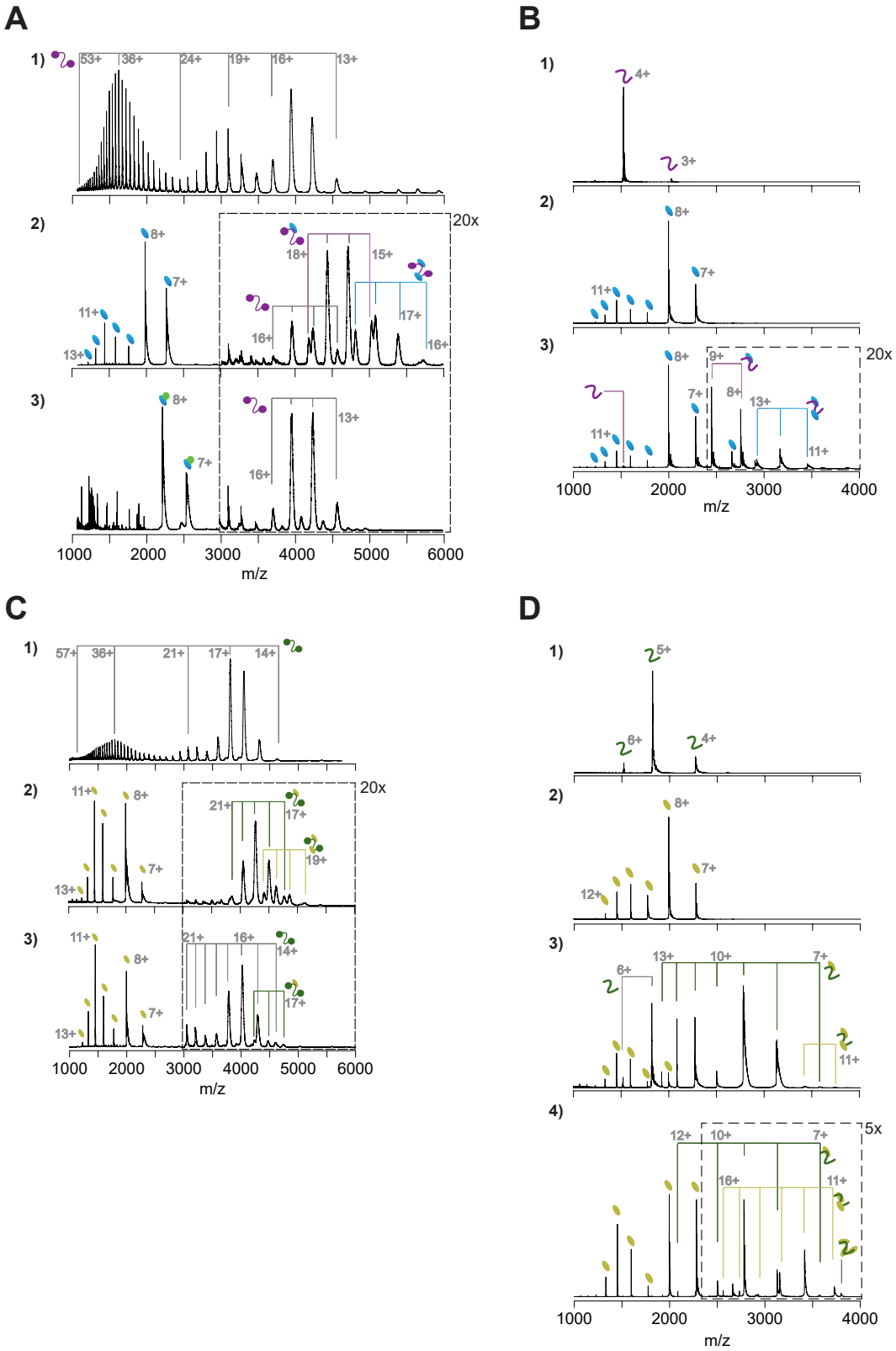
A
1)
53+
36+
24+
19+
16+
13+
2)
8+
7+
11+
13+
18+
15+
16+
17+
16+
20x
3)
8+
7+
16+
13+
1000
2000
3000
4000
5000
6000
m/z
B
1)
4+
3+
2)
8+
7+
11+
3)
8+
9+
7+
8+
13+
11+
11+
20x
1000
2000
3000
4000
m/z
C
1)
57+
36+
21+
17+
14+
2)
11+
8+
7+
13+
21+
17+
19+
20x
3)
11+
8+
7+
13+
21+
16+
14+
17+
1000
2000
3000
4000
5000
6000
m/z
D
1)
5+
6+
4+
2)
8+
7+
12+
3)
6+
13+
10+
7+
11+
4)
12+
10+
7+
16+
11+
5x
1000
2000
3000
4000
m/z

571 **Figure S8. Native mass spectrometry analyses of HsC53-GABARAP and AtC53-ATG8A**
572 **interactions. (a)** Native mass spectrometry (nMS) of **(1)** HsC53 (5 μM), **(2)** HsC53 (5 μM) + GABARAP
573 (20 μM), and **(3)** HsC53 (5 μM) + GABARAP (10 μM) + AIM *wt* peptide (10 μM). **(1)** HsC53 is a
574 monomeric protein, which presents in charge states 13+ to 53+. The trimodal shape of the charge state
575 distribution is diagnostic of a protein that exists in compact and extended conformations (Beveridge et al.,
576 2014). **(2)** Binding of HsC53 to GABAPRAP is observed in 1:0, 1:1 and 1:2 ratios. **(3)** All GABARAP is
577 now present in a 1:1 complex with the AIM peptide, which prevents it from binding to HsC53. HsC53 is
578 present in the unbound state. **(b)** nMS of **(1)** HsC53-IDR (2.5 μM), **(2)** GABARAP (5 μM), and **(3)** HsC53-
579 IDR (2.5 μM) + GABARAP (12.5 μM). Binding of HsC53-IDR to GABARAP is observed in 1:1 and 1:2
580 ratios. **(c)** nMS of **(1)** AtC53 (1 μM), **(2)** AtC53 (1 μM) + AtG8A (5 μM), and **(3)** $AtC53^{sAIM}$ (1 μM) +
581 AtG8A (5 μM). **(1)** AtC53 is a monomeric protein, which presents in charge states 14+ to 57+. The trimodal
582 shape of the charge state distribution is diagnostic of a protein that exists in compact and extended
583 conformations (Beveridge et al., 2014). **(2)** Binding of AtC53 to AtG8A is observed in 1:1 and 1:2 ratios.
584 **(3)** $AtC53^{sAIM}$ is mainly present in the unbound state, with small amounts of 1:1 complex formed with
585 AtG8A. **(d)** nMS of **(1)** AtC53-IDR (2.5 μM), **(2)** AtG8A (10 μM), **(3)** AtC53-IDR (2.5 μM) + AtG8A (10
586 μM), and **(4)** AtC53-IDR (2.5 μM) + AtG8A (20 μM). Binding of AtC53-IDR to ATG8A is observed in
587 1:1 and 1:2 ratios, with a small amount of 1:3 binding at 1:8 molar excess of ATG8A.
588
589
590
591

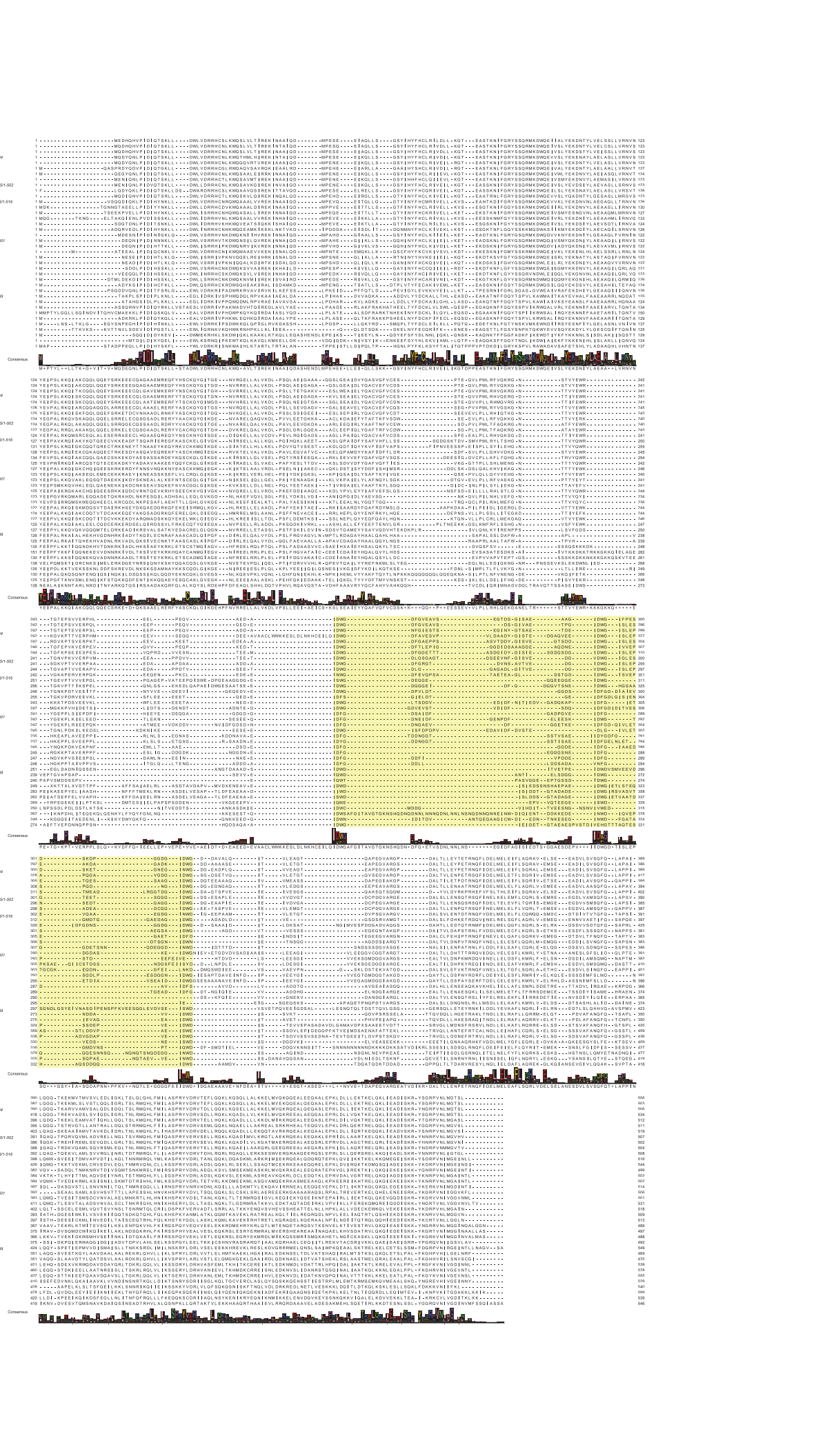

592 **Figure S9. Multiple sequence alignment of C53 homologs**. Protein sequences of C53 homologs from
593 selected multicellular eukaryotic species were aligned using Clustal Omega server (Madeira et al., 2019)
594 and processed with Jalview. Residue numbers are labelled according to the HsC53 sequence. The multiple
595 sequence alignment used in Figure 3D is highlighted in yellow.
596

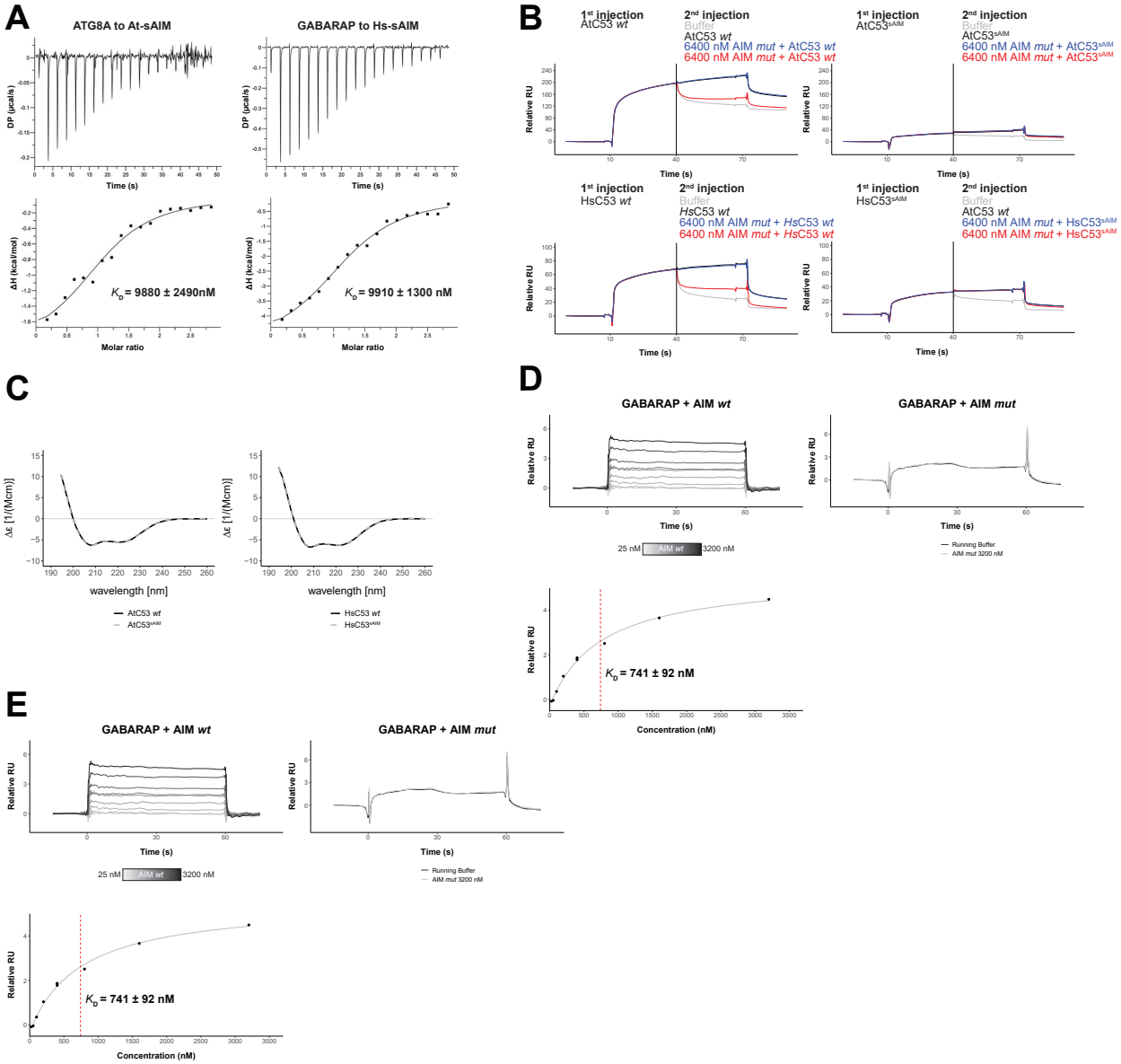
A
ATG8A to At-sAIM
GABARAP to Hs-sAIM
DP (µcal/s)
Time (s)
ΔH (kcal/mol)
Molar ratio
K_D = 9880 ± 2490nM
K_D = 9910 ± 1300 nM
B
1st injection
AtC53 wt
2nd injection
Buffer
AtC53 wt
6400 nM AIM mut + AtC53 wt
6400 nM AIM mut + AtC53 wt
1st injection
AtC53sAIM
2nd injection
Buffer
AtC53sAIM
6400 nM AIM mut + AtC53sAIM
6400 nM AIM mut + AtC53sAIM
1st injection
HsC53 wt
2nd injection
Buffer
HsC53 wt
6400 nM AIM mut + HsC53 wt
6400 nM AIM mut + HsC53 wt
1st injection
HsC53sAIM
2nd injection
Buffer
AtC53 wt
6400 nM AIM mut + HsC53sAIM
6400 nM AIM mut + HsC53sAIM
Relative RU
Time (s)
C
Δε [1/(Mcm)]
wavelength [nm]
AtC53 wt
AtC53sAIM
HsC53 wt
HsC53sAIM
D
GABARAP + AIM wt
GABARAP + AIM mut
Relative RU
Time (s)
25 nM
AIM wt
3200 nM
Running Buffer
AIM mut 3200 nM
K_D = 741 ± 92 nM
Concentration (nM)
E
GABARAP + AIM wt
GABARAP + AIM mut
Relative RU
Time (s)
25 nM
AIM wt
3200 nM
Running Buffer
AIM mut 3200 nM
K_D = 741 ± 92 nM
Concentration (nM)

Figure S10. Biophysical characterization of sAIM mediated C53-ATG8 interaction. (a) Isothermal titration calorimetry (ITC) experiments showing binding of At-sAIM and Hs-sAIM peptides to ATG8A and GABARAP, respectively. Upper left and right panels show heat generated upon titration of At-sAIM (EPLDFDIDWDLEEEM) (600 μM) or Hs-sAIMC53 (EPLDFDIDWGLEEEM) (600 μM) to ATG8A or GABARAP (both 40 μM). Lower left and right panels show integrated heat data (■) and the fit (solid line) to a one-set-of-sites binding model using PEAQ-ITC analysis software. Representative values of K_D, N, ΔH, -TΔS and ΔG from three independent ITC experiments are reported in Table S5. **(b)** AtC53 and HsC53 sAIM mutants do not interact with ATG8A or GABARAP, respectively. *Upper Panels,* GST-ATG8A or *Lower Panels,* GST-GABARAP were captured on the surface of the active cell (500 RU) and GST was captured on the surface of the reference cell (300 RU). The 2 flow cells were exposed to the ligands *Upper left* AtC53, *Upper right* AtC53^{sAIM}, *Lower Left*, HsC53 and *Lower right,* HsC53^{sAIM} with 4 sets of double consecutive injections (1st set: 10 μM ligand, running buffer; 2nd set: 10 μM ligand, 10 μM ligand; 3rd set: 10 μM ligand, 10 μM ligand + 6.4 μM AIM *wt* peptide; 4th set: 10 μM protein, 10 μM protein + 6.4 μM AIM *mut* peptide. Binding curves were obtained by subtracting the reference cell from the active cell. A representative sensorgram from two independent experiments is shown. **(c) AtC53^{sAIM} and HsC53^{sAIM} mutants have similar secondary structure compared to AtC53 and HsC53, respectively.** *Left Panel*, Far-UV circular dichroism (CD) spectra of AtC53 *wt* (black line) and its variant AtC53^{sAIM} (grey dashed line). *Right Panel*, Far-UV circular dichroism (CD) spectra of HsC53 *wt* (black line) and its variant HsC53^{sAIM} (grey dashed line). **(D) Quantification of the binding affinity of AIM *wt* to GABARAP.** GST-GABARAP fusion protein was captured on the surface of the active cell (500 RU) and GST was captured on the surface of the reference cell (300 RU). Representative sensorgrams from at least 3 independent experiments are shown. *Upper Left Panel*, Multi-cycle kinetics experiment with increasing concentrations of the AIM *wt* peptide. Binding curves were obtained by double referencing (i.e. reference cell signal subtracted from active cell signal; subtraction of buffer injection). 400 nM* = Internal replicate. *Upper Right Panel*, Injection of running buffer (grey) and 3600 nM AIM *mut* peptide (black). *Lower Left Panel*, Plot of steady-state response units versus the respective concentration of the AIM *wt* peptide, which was used to determine the dissociation constant K_D. **(E) Quantification of the binding affinity of AIM *wt* to**

624 **ATG8A.** GST-ATG8A fusion protein was captured on the surface of the active cell (500 RU) and GST was
625 captured on the surface of the reference cell (300 RU). Representative sensorgrams from at least 3
626 independent measurements are shown. *Upper Left Panel*, Multi-cycle kinetics experiment with increasing
627 concentrations of the AIM *wt* peptide. Binding curves were obtained by double referencing (i.e. reference
628 cell signal subtracted from active cell signal; subtraction of buffer injection). 400 nM* = Internal replicate.
629 *Upper right Panel*, Injection of running buffer (grey) and 3600 nM AIM *mut* peptide (black). *Lower Left*
630 *Panel*, Plot of steady-state response units versus the respective concentration of the AIM *wt* peptide which
631 was used to determine the dissociation constant K_D.
632
633
634

A

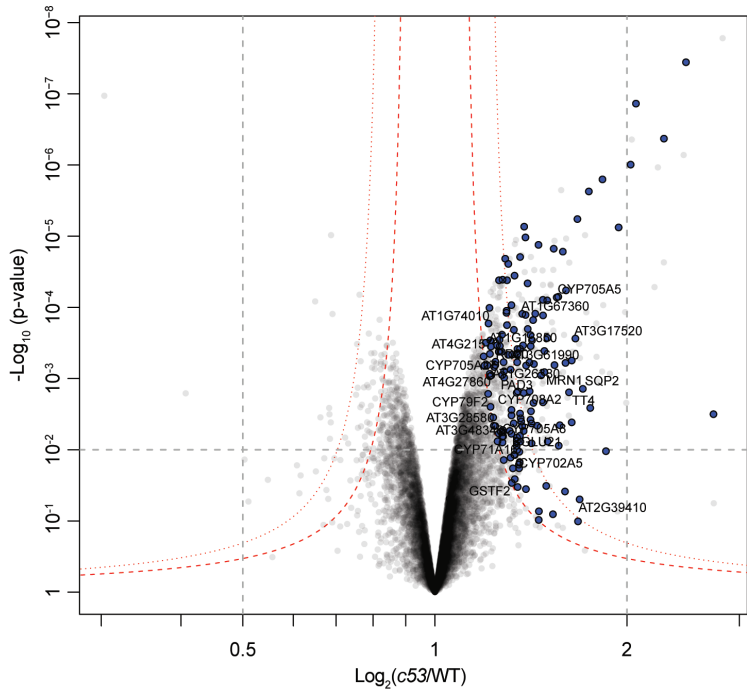
-Log10 (p-value)
Log2(c53/WT)
0.5
1
2
CYP705A5
AT1G67360
AT1G74010
AT3G17520
AT4G27860
PAD3
MRN1
SQP2
CYP79F2
CYP708A2
TT4
CYP702A5
GSTF2
AT2G39410

B

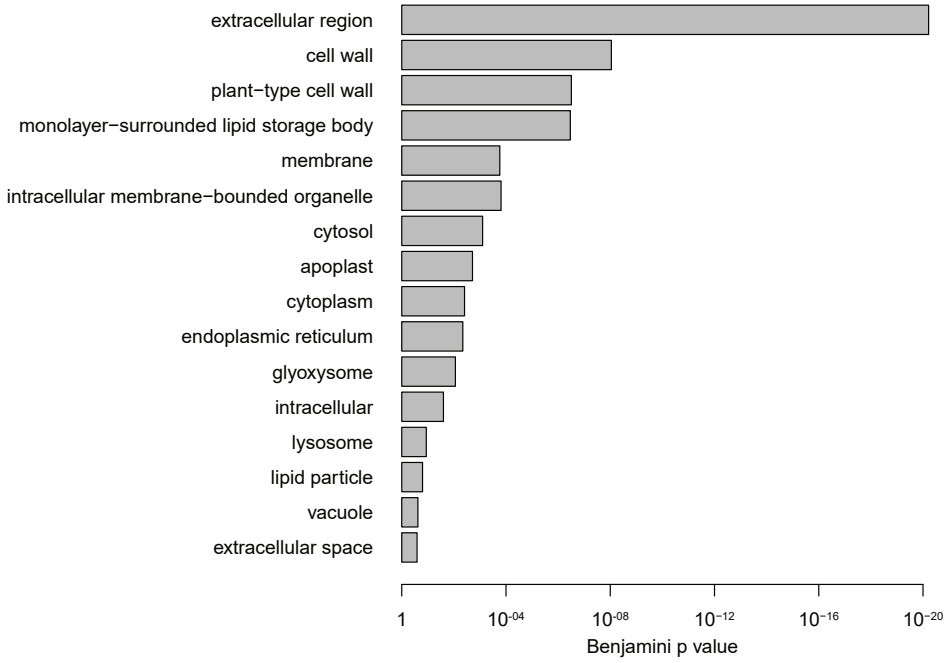
extracellular region
cell wall
plant−type cell wall
monolayer−surrounded lipid storage body
membrane
intracellular membrane−bounded organelle
cytosol
apoplast
cytoplasm
endoplasmic reticulum
glyoxysome
intracellular
lysosome
lipid particle
vacuole
extracellular space
1
10-04
10-08
10-12
10-16
10-20
Benjamini p value

635 **Figure S11. Quantitative proteomics analyses of AtC53 mediated degradation. (a) Volcano plot**
636 **showing proteins that are accumulating in *Atc53 mutants***. Names of ER resident proteins are shown.
637 Proteins that are labelled with blue either reside or mature at the ER. **(b) GO analysis of proteins**
638 **accumulating in *Atc53*.** See Table S3 and Table S4 for details.
639

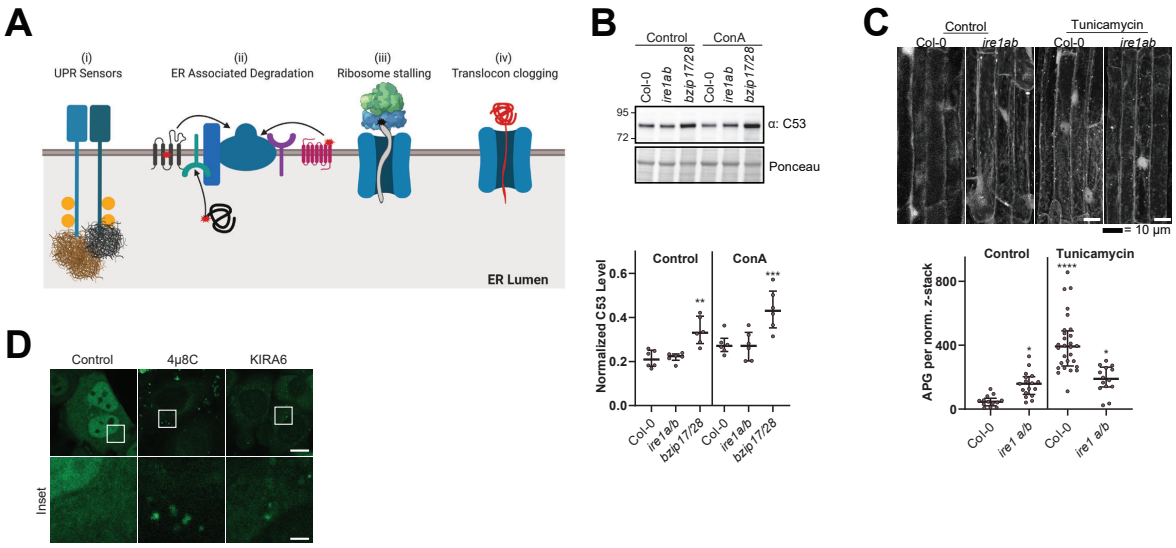
A
(i)
UPR Sensors
(ii)
ER Associated Degradation
(iii)
Ribosome stalling
(iv)
Translocon clogging
ER Lumen
B
Control
ConA
Col-0
ire1ab
bzip17/28
Col-0
ire1ab
bzip17/28
95
72
α: C53
Ponceau
Control
ConA
Normalized C53 Level
0.6
0.4
0.2
0.0
**
***
Col-0
ire1a/b
bzip17/28
Col-0
ire1a/b
bzip17/28
C
Control
Tunicamycin
Col-0
ire1ab
Col-0
ire1ab
= 10 µm
Control
Tunicamycin
APG per norm. z-stack
800
400
0
****
*
*
Col-0
ire1 a/b
Col-0
ire1 a/b

D
Control
4µ8C
KIRA6
Inset

640 **Figure S12. C53 is not activated by associating with UPR sensors. (a) Cartoon explaining the four**
641 **scenarios we tested to understand the mechanism of activation of C53. (b) AtC53 flux is enhanced in**
642 **Arabidopsis UPR sensor mutants.** *Upper Panel*, representative western blot image of autophagic flux
643 analysis of C53 in Col-0 wild type, *ire1a/b*, and *bzip17/28* double mutants. Seedlings were incubated in
644 either control (Ctrl) or 1 µM concanamycin A (ConA) containing medium for 16 h. Proteins extracted from
645 whole seedlings were analysed by immunoblotting with anti-C53 antibody. Total proteins were analysed
646 by Ponceau S staining. *Lower Panel*, Quantification of the intensities of the C53 bands normalized to the
647 total protein level of the lysate (Ponceau S). Average C53 levels and SD for n = 6 are shown. Significant
648 differences are indicated with * when p value ≤ 0.05, ** when p value ≤ 0.01, and *** when p value ≤
649 0.001. **(c) AtC53 puncta are already induced in *ire1a/b* without ER stress.** *Upper Panel,* Confocal
650 micrographs of autophagic flux of transgenic seedlings expressing C53-mCherry in Col-0 wild type and the
651 *ire1a/b* double mutant. Seedlings were incubated in either control media or media containing 10 µg/ml
652 tunicamycin (Tm). Representative confocal images in single plane are shown. Scale bars, 10 µm. *Lower*
653 *Panel,* Quantification of autophagosomes (APG) per normalized Z-stack. Bars represent the mean (± SD)
654 of at least 10 biological replicates. **(d) Chemical inhibition of IRE1 activity enhances HsC53 autophagic**
655 **flux in HeLa cells.** Confocal micrographs of PFA fixed HeLa cells transiently expressing HsC53-GFP.
656 Cells were either left untreated (Control) or treated for 1 h with 5µM 4µ8C (IRE1 RNase activity inhibitor)
657 or 1µM KIRA6 (IRE1 kinase activity inhibitor). Inhibitor treatments led to the depletion of HsC53 from
658 the nucleus and puncta formation. Scale Bar, 20 µm. Representative images are shown.
659

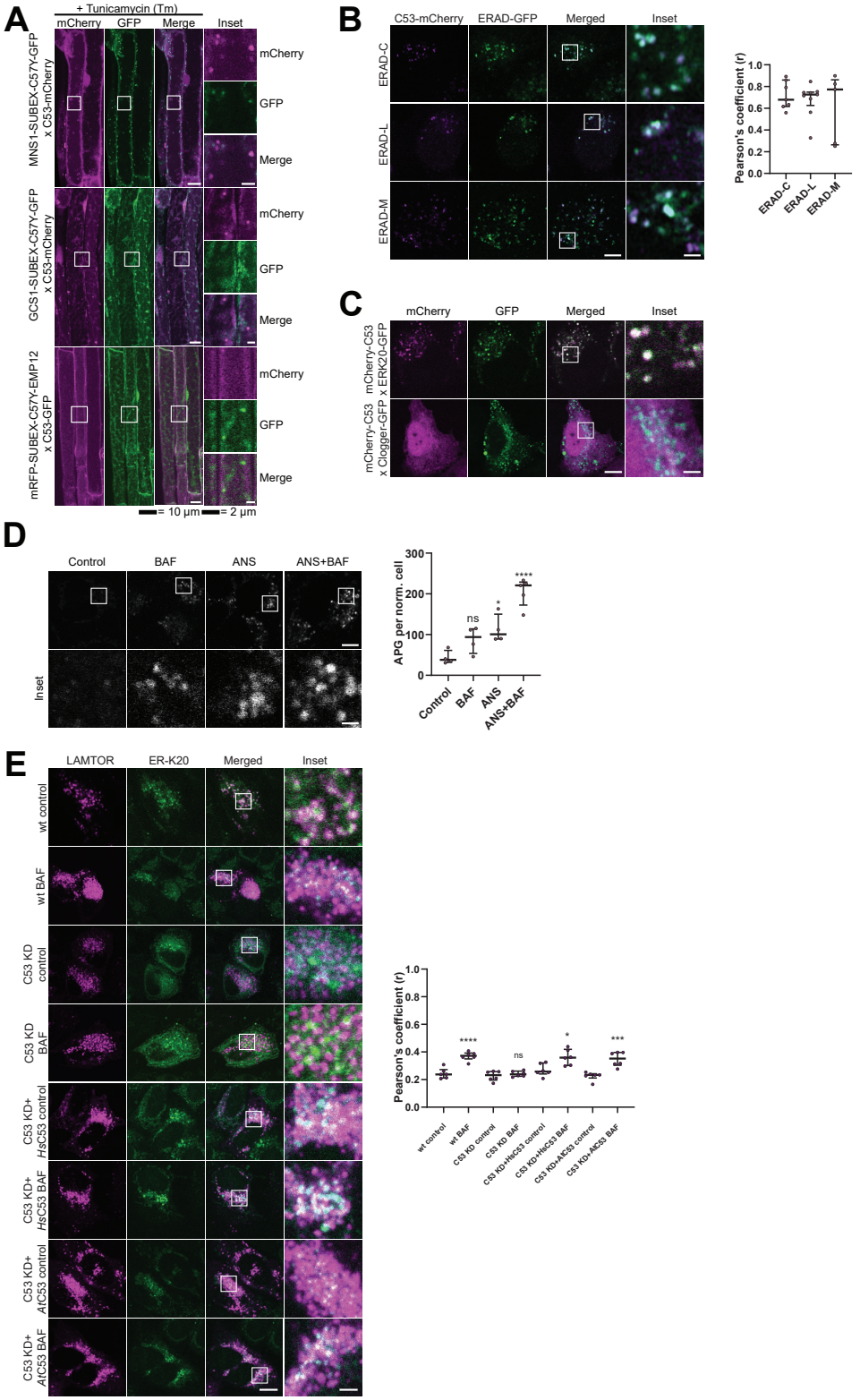
A
+ Tunicamycin (Tm)
mCherry
GFP
Merge
Inset
MNS1-SUBEX-C57Y-GFP x C53-mCherry
GCS1-SUBEX-C57Y-GFP x C53-mCherry
mRFP-SUBEX-C57Y-EMP12 x C53-GFP
= 10 µm
= 2 µm
B
C53-mCherry
ERAD-GFP
Merged
Inset
ERAD-C
ERAD-L
ERAD-M
Pearson's coefficient (r)
C
mCherry
GFP
Merged
Inset
mCherry-C53 x ERK20-GFP
mCherry-C53 x Clogger-GFP
D
Control
BAF
ANS
ANS+BAF
Inset
APG per norm. cell
ns
****
E
LAMTOR
ER-K20
Merged
Inset
wt control
wt BAF
C53 KD control
C53 KD BAF
C53 KD+ HsC53 control
C53 KD+ HsC53 BAF
C53 KD+ AtC53 control
C53 KD+ AtC53 BAF
Pearson's coefficient (r)
****
ns
*
***

660 **Figure S13. C53 is activated upon ribosome stalling during co-translational protein translocation. (a)**
661 **AtC53 does not co-localize with ERAD substrates.** *Left Upper Panel*, Colocalization analysis from
662 confocal micrographs of C53-mCherry or C53-GFP (magenta/green) transgenic lines crossed with MNS1-
663 SUBEX-C57Y-GFP (green), GCS1-SUBEX-C57Y-GFP (green), or mRFP-SUBEX-C57Y-EMP12
664 (magenta). Transgenic seedlings were incubated in either control or tunicamycin (10 µg/ml) containing
665 media. Representative confocal images of control conditions are shown as maximum projection images to
666 demonstrate the ER localization of the substrates. Images of tunicamycin treatments are shown in single
667 plane. Scale bar, 10 µm. Inset scale bar, 2 µm. **(b) HsC53 partially co-localizes with ERAD substrates.**
668 *Left Panel,* Confocal images of PFA fixed HeLa cells transiently co-expressing C53-mCherry with GFP-
669 CFTRΔF508 (ERAD-C), A1AT^{NHK}-GFP (ERAD-L), and INSIG1-GFP (ERAD-M). Scale Bar, 20µm.
670 *Right Panel,* Pearson's Coefficient analysis of the co-localization. (**c) HsC53 colocalize with ribosome**
671 **stalling construct ER-K20.** Confocal images of PFA fixed HeLa cells co-expressing ER-K20-GFP or the
672 clogger construct with mCherry-HsC53. **(d) HsC53 puncta are induced by anisomycin treatment.** *Left*
673 *Panel,* Confocal images of PFA fixed HeLa cells transiently expressing C53-GFP. Cells were either left
674 untreated or treated for 15 min with 200 nM anisomycin (ANS) and subsequently given a recovery period
675 of 2 h in the presence or absence of 100 nM bafilomycin A1 (BAF). Scale Bar, 20 µm. *Right Panel,*
676 Quantification of C53 puncta. **(e) HsC53 mediates degradation of the ribosome stalling construct ER-**
677 **K20.** *Upper Panel,* Confocal images of PFA fixed HeLa cells transiently expressing ER_K20-GFP (green)
678 and miRFP-LAMTOR1 (magenta). HsC53 knock down (KD) cells were complemented with HsC53 or
679 AtC53. Cells were either left untreated or treated for 2 h with 100 nM bafilomycin A1 (BAF). Scale Bar,
680 20 µm. Representative images are shown. *Lower Panel:* Quantification of the colocalization of Lamtor1
681 with ER-K20 in knock down and complemented cells.

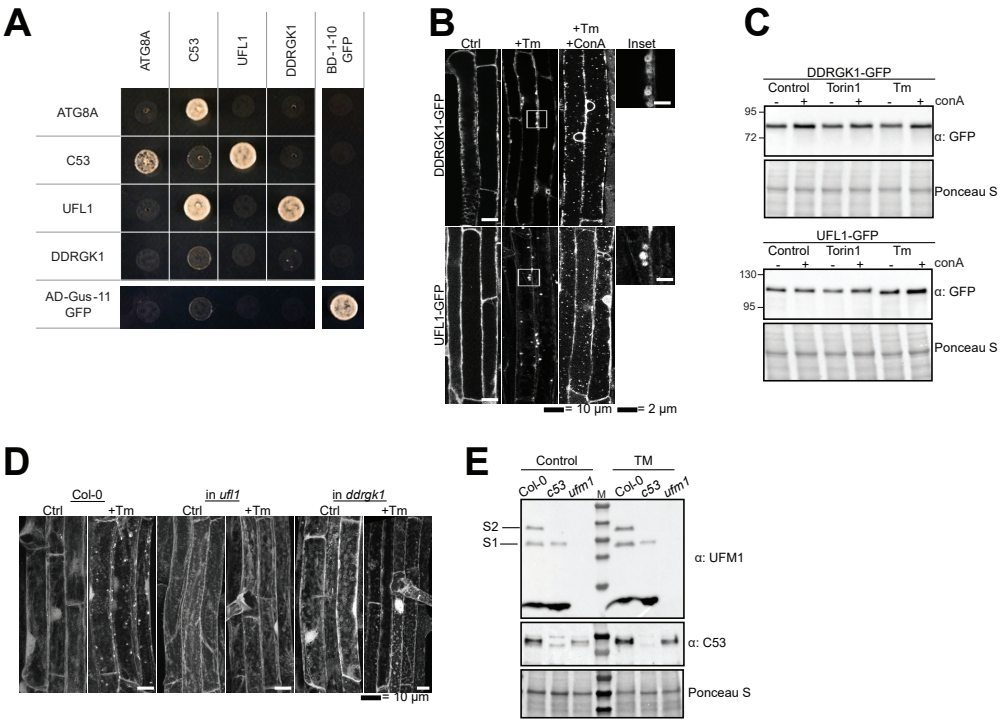
A
ATG8A
C53
UFL1
DDRGK1
BD-1-10 GFP
AD-Gus-11 GFP
B
Ctrl
+Tm
+Tm +ConA
Inset
DDRGK1-GFP
UFL1-GFP
= 10 µm
= 2 µm
C
DDRGK1-GFP
Control
Torin1
Tm
conA
95
72
α: GFP
Ponceau S
UFL1-GFP
130
95
D
Col-0
in ufl1
in ddrgk1
Ctrl
+Tm
= 10 µm
E
Control
TM
Col-0
c53
ufm1
M
S2
S1
α: UFM1
α: C53
Ponceau S

682 **Figure S14. C53, DDRGK1, and UFL1 form a tripartite receptor complex. (a) pairwise Yeast two**
683 **hybrid analysis of Arabidopsis thaliana UFL1, C53, DDRGK1, and ATG8A.** Combinations of
684 pGADT7 (prey vector) and pGBKT7 (bait vector) vectors carrying the indicated genes were transformed
685 in yeast. After mating, yeast was selected for growth on (SD)-Leu/-Trp, (SD)-Leu/-Trp/-His and (SD)-Leu/-
686 Trp/-His/-Ade plates (displayed). Split GFP was used as a positive control. **(b, c) DDRGK1 and UFL1**
687 **undergo vacuolar degradation upon ER stress. (b)** Confocal micrographs of transgenic seeds expressing
688 UFL1-GFP and DDRGK1-GFP. Seedlings were incubated in either control, 10 µg/ml tunicamycin (Tm) or
689 10 µg/ml tunicamycin and 1 µM concanamycin A (Tm+ConA). Representative confocal images in single
690 plane are shown. Scale bars, 10 µm. Inset scale bars, 2 µm. **(c)** Representative western blots of UFL1-GFP
691 and DDRGK1-GFP upon ER stress treatments. Seedlings were incubated in either control, 10 µg/ml
692 tunicamycin (Tm) or 10 µg/ml tunicamycin with 1 µM concanamycin A (Tm+ConA). Protein extracts from
693 whole seedlings were analysed by immunoblotting with anti-GFP. Total proteins were analysed by Ponceau
694 S staining. **(d) AtC53 puncta formation requires UFL1 and DDRGK1.** Representative confocal images
695 of Col-0, *ufl1*, and *ddrgk1* Arabidopsis seedlings. 6-day old seedlings were incubated in either control (Ctrl)
696 or 10 µg/ml tunicamycin (Tm) containing media. In contrast to wild type, AtC53 did not form puncta in
697 DDRGK1 and UFL1 mutants. For quantification, see Figure 3f. **(e) Validation of UFM1 antibody used**
698 **in 3g.** S1 and S2 correspond to ufmylated RPL26 bands.

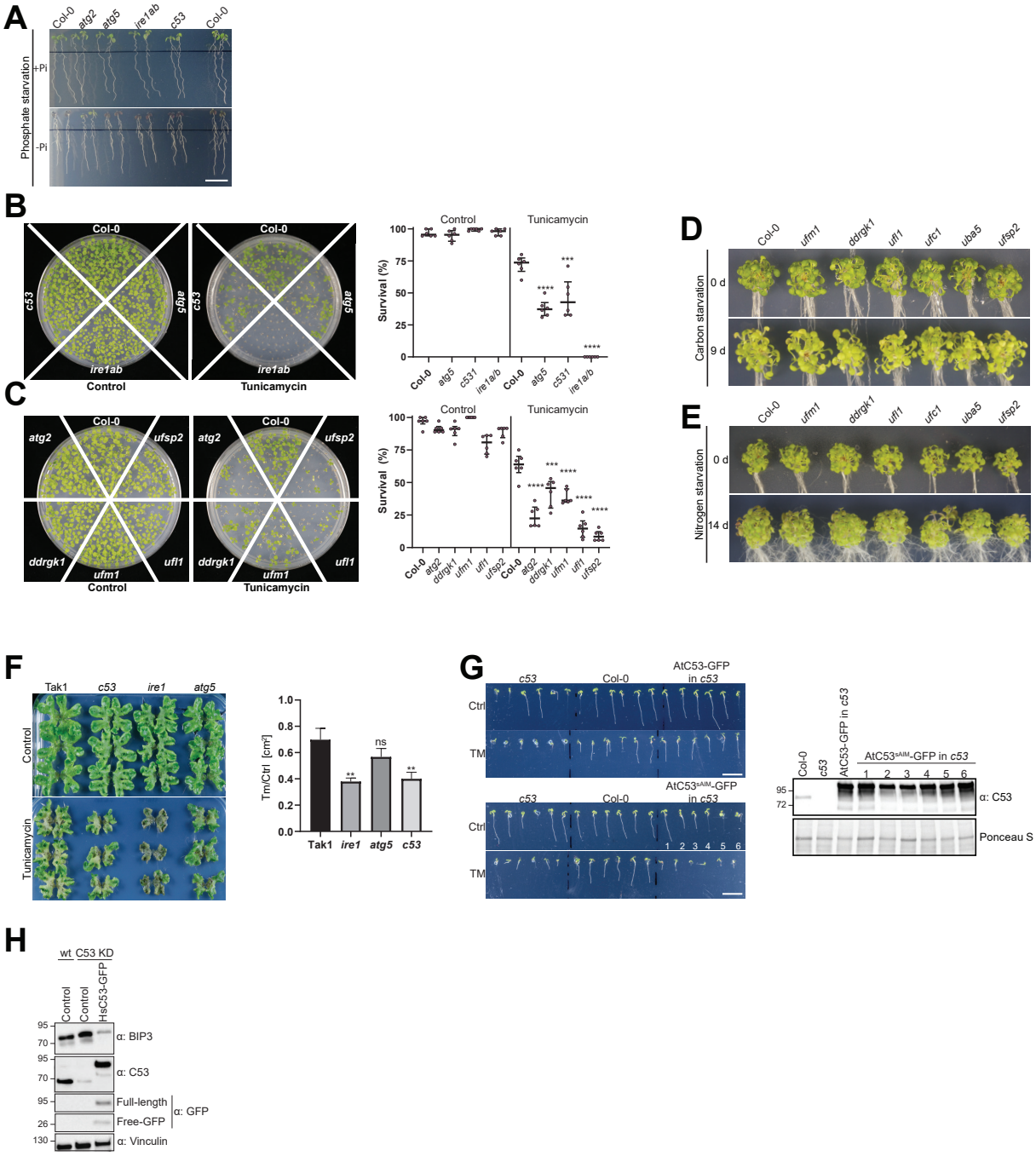
A
Col-0
atg2
atg5
ire1ab
c53
Col-0
Phosphate starvation
+Pi
-Pi
B
Col-0
c53
atg5
ire1ab
Control
Tunicamycin
Survival (%)
Control
Tunicamycin
Col-0
atg5
c531
ire1a/b
C
Col-0
atg2
ufsp2
ddrgk1
ufl1
ufm1
Control
Tunicamycin
D
Col-0
ufm1
ddrgk1
ufl1
ufc1
uba5
ufsp2
Carbon starvation
0 d
9 d
E
Nitrogen starvation
14 d
F
Tak1
c53
ire1
atg5
Control
Tunicamycin
Tm/Ctrl [cm²]
ns
Tak1
ire1
atg5
c53
G
c53
Col-0
AtC53-GFP in c53
Ctrl
TM
AtC53sAIM-GFP in c53
1 2 3 4 5 6
Col-0
c53
AtC53-GFP in c53
AtC53sAIM-GFP in c53
α: C53
Ponceau S
H
wt
C53 KD
Control
Control
HsC53-GFP
α: BIP3
α: C53
Full-length
Free-GFP
α: GFP
α: Vinculin

Figure S15. C53 and the UFMylation machinery are essential for ER stress tolerance (a) *Atc53* mutant is sensitive to phosphate starvation. Seedlings were germinated for 5 days on +Pi media prior to transfer for 2 days to medium supplemented with or without Pi (-Pi, +Pi) and imaged after 2 days (Naumann et al., 2019). See Figure 5c for quantification. Scale bars, 1 cm. **(b, c) *Atc53* and UFMylation pathway mutants display lower survival on tunicamycin-containing plates.** Seedlings were grown on control or 150 ng/mL tunicamycin containing half-strength MS media for two weeks and were evaluated for survival. *Left Panel* shows an example of the plates. *Right Panel*, Quantification of living and dead seedlings. Data represents 6 plates with 4 x 36 seedlings (n=216). Survival percentage was compared pairwise to the survival of the wildtype (Col-0). Data represent the median with its interquartile range. **(d,e) Ufmylation mutants are insensitive to carbon and nitrogen starvation**. **(d)** Phenotypes before (0 d) and after 9 days carbon starvation (9 d). n ≥ 25. 7-day old seedlings per genotype were used. **(e)** Phenotypes before (0 d) and after 14 days nitrogen starvation (14 d). n ≥ 25. 7-day old seedlings per genotype were used. **(f) *Marchantia polymorpha c53* mutants are sensitive to tunicamycin.** 14-day old plants were transferred to control or 2 µg/ml tunicamycin containing agar plates. *Right Panel,* Quantification of the plant area 21 days after transfer. Data shown as mean ±SD. **(g) The AtC53^{sAIM} mutant does not complement tunicamycin sensitivity phenotype.** *Left Panel,* Representative images of 7-day old seedlings grown on half strength MS media without sucrose in control conditions (Ctrl) or treated with 100 ng/mL tunicamycin (Tm). At least 10 independent T1 transgenic lines were analysed to measure the root lengths. See Figure 5g for quantification. Significant differences compared to control treatment (Ctrl) are indicated with * when p value ≤ 0.05, ** when p value ≤ 0.01, and *** when p value ≤ 0.001. *Right Panel*, western blot analyses of AtC53 complementation lines showing expression of the tested constructs used in Figure 5g. **(h) Knockdown of C53 leads to increased BiP3 chaperone levels.** Knock down and complementation assays showing C53 function is important for ER stress tolerance in HeLa cells.

727 **Methods**
728

729 **Cloning procedures**

730 Constructs for *Arabidopsis thaliana* and *E. coli* transformation were generated using the GreenGate (GG)
731 cloning method (Lampropoulos et al., 2013). Plasmids used are listed in materials section. The coding
732 sequence of genes of interest were either ordered from Twist Biosciences or Genewiz or amplified from
733 Col-0 or HeLa cDNA using the primers listed in the materials section. The internal BsaI sites were mutated
734 by site-directed-mutagenesis without affecting the amino acid sequence.

735 For *Marchantia polymorpha* Gateway Cloning (Ishizaki et al., 2015) was used to generate all constructs.

736 For HeLa expression experiments, plasmids used are listed in the materials section. The constructs were
737 made by conventional restriction enzyme-based cloning.

738 **CRISPR/Cas9 construct design**

739 The CRISPR/Cas9 constructs for mutating *c53*, *DDRGK1* and *UFM1* in *Arabidopsis thaliana* were
740 prepared according to the protocol described by Xing et al., 2014 (Xing et al., 2014) and Wang et al., 2015
741 (Ma et al., 2015). The pHEE401E and pCBC-DT1T2 vectors for expressing two sgRNAs were provided
742 by Youssef Belkhadir and Jixiang Kong, GMI Vienna. sgRNA target sites were chosen using the website
743 http://crispr.hzau.edu.cn/CRISPR2/. Each gene was targeted by two sgRNAs to remove a fragment of the
744 gene. The CRISPR cassettes of each gene were generated by PCR amplification using pCBC-DT1T2 as
745 template with the primer pairs BsF/F0 and BsR/R0, using adaptors containing the BsaI-restriction sites
746 respectively (see materials section). The PCR products were digested with *Bsa*I, ligated into the pHEE401E
747 plasmid, and transformed into DH5α *E. coli*. Floral dipping proceeded as described previously (Clough and
748 Bent, 1998). Genotyping primers P1 5′-xxx-3′ and P2 5′-xxx-3′ flanking each target site were used to select
749 T1 plants that carried deletions. Sanger sequencing was performed to define the deletion. Through
750 backcrossing with Col-0 plants and genotyping, Cas9-free plants were achieved.

751 In *Marchantia polymorpha*, CRISPR/Cas9 constructs were generated by selecting two target sequences in
752 *c53* and *ire1*. Synthetic oligonucleotides were annealed and inserted at the BsaI site of the entry vector
753 pMpGE_En03 flanked by attL1 and attL2 sequences (Sugano et al., 2018). The resultant cassettes were

754 inserted to the destination vector pMpGE011 by LR Clonase II Enzyme Mix. The vectors were introduced
755 into thalli of TAK1 via *A. tumefaciens* GV3101+pSoup, and the transformants were selected with 0.5 µM
756 chlorsulfuron (KUBOTA et al., 2013). Genomic DNA from transformants was amplified by PCR and sent
757 for sequencing to verify mutations.

758 **Plant materials and Growth conditions**

759 All *Arabidopsis thaliana* lines used originate from the Columbia (Col-0) ecotype background. Mutant lines
760 used in this study are listed in the materials section. All transgenic plants were generated by the floral
761 dipping method (Clough and Bent, 1998) for which the plasmid constructs were prepared using the green
762 gate cloning method (Lampropoulos et al., 2013).

763 Seeds were then spread on plates or liquid culture with half-strength MS media (Murashige & Skoog salt +
764 Gamborg B5 vitamin mixture) with 1 % sucrose ,0.5 g/L MES and 1% plant agar. pH was adjusted to 5.7
765 with NaOH. Seeds were imbibed for 4 days at 4 °C in darkness. Plants were grown at 21 ºC at 60 % humidity
766 under LEDs with 50 µM/m^2s and 12h:12h photoperiod.

767 For the autophagy flux assay, TMT and *in-vivo* immunoprecipitation, seedlings were grown in liquid culture
768 under continuous light.

769 Male *Marchantia polymorpha* accession Takaragaike-1 (Tak-1) was maintained asexually and cultured
770 through gemma using half-strength Gamborg's B5 medium containing 1% agar under 50-60 mmol photons
771 $m^{-2}s^{-1}$ continuous white light at 22° C unless otherwise defined (KUBOTA et al., 2013).

772 **Plant Sensitivity Tests**

773 <u>*Arabidopsis thaliana*</u>

774 **Root-length quantification**

775 Seedlings were grown for 9 days on media supplemented with the indicated drug concentration. Plates were
776 scanned on day 0 and then quantified daily starting from day 2 to day 9. Large scale root-length
777 quantification was conducted using the automated plant imaging analysis software BRAT (Buschlab Root
778 Analysis Toolchain) (Slovak et al., 2014) with the inhouse high-performance computer cluster MENDEL.
779 Before analysis, collected data was passed through software quality control.

780 **Starvation treatments**

781 Carbon Starvation: Seedlings were grown on half-strength MS media with 1% sucrose for 7 days. They
782 were then transferred to media without sucrose, followed by wrapping the plates in aluminium foil and
783 placing them under the same growth conditions as before for 9 days.
784 Nitrogen Starvation: Seedlings grew on half-strength MS media with 0.5% sucrose for 7 days. They were
785 then transferred to media without nitrogen and put under the same growth conditions as before for 14 days.
786 Seedlings were arranged in a similar fashion to Jia et al., 2019 (Jia et al., 2019).
787 Phosphate Starvation: The method was previously described by Naumann *et al*., 2018 (Naumann et al.,
788 2019). Seeds were surface-sterilized and germinated 5 days on +Pi medium prior to transfer to 1% (w/v)
789 Phyto-Agar (Duchefa) containing 2.5 mM KH_2PO_4, pH 5.6 (high Pi or +Pi medium) or no Pi supplement
790 (low Pi or –Pi medium), 5 mM KNO_3, 0.025 mM Fe-EDTA, 2 mM $MgSO_4$, 2 mM Ca(NO3)2, 2.5 mM
791 MES-KOH, 0.07 mM H3BO3, 0.014 mM $MnCl_2$, 0.01 mM NaCl, 0.5 µM $CuSO_4$, 1 µM $ZnSO_4$, 0.2 µM
792 Na_2MoO_4, 0.01 µM $CoCl_2$, 5 g/L sucrose. The agar was routinely purified by repeated washing in deionized
793 water and underwent subsequent dialysis using DOWEX G-55 anion exchanger (Ticconi et al., 2009). ICP-
794 MS analysis of the treated agar (7.3 µg/g Fe and 5.9 µg/g P) indicated a contribution of 1.25 µM Fe and
795 1.875 µM P to the solid 1% agar medium. Images were analysed using ImageJ software.
796 **Survival Assay**
797 Seedlings were grown on 9 cm round plates supplemented with the indicated drug at the indicated
798 concentration. Seedling survival was quantified after 14 days. Differentiation between live and dead
799 seedlings was carried out similar to Yang et al., 2016 (Yang et al., 2016). Surviving seedlings were defined
800 as seedlings which had two green cotyledons and two green true leaves. Plants with yellow leaves or
801 cotyledons were defined as dead.
802 *Marchantia polymorpha*
803 Tunicamycin Sensitivity
804 14 days old plants were transformed to half-strength Gamborg's B5 medium containing indicated
805 concentration of tunicamycin and grown in continues light at 22°C to determine survival rates.
806 **Autophagy flux assay in *Arabidopsis thaliana***

807 20-30 seedlings for western blot or 0.5 - 1 g seedlings for immunoprecipitation and mass spectrometry were
808 grown in liquid culture for 5 d under continuous light with shaking at 80 rpm. Media was supplemented
809 with different drugs (3 µM Torin, 10 µg/ml Tunicamycin or other drugs dissolved in DMSO) as indicated.
810 1 µM of concanamycin was added, if indicated in figures, to track the contribution of vacuolar degradation.
811 For nutrient starvation, seedlings were transferred to phosphate, nitrogen- or sucrose-depleted media (–C,
812 –P, -N). The plants were kept in the dark to reduce sucrose production by photosynthesis or to provide drug
813 stability. Pure DMSO was added to control samples. For analysing total protein degradation such as TMT,
814 seedlings were flash frozen in liquid nitrogen after 24 h treatment. For interaction analysis such as Co-
815 immunoprecipitation, seedling treatment was stopped after 8 h of treatment.
816 Samples were homogenized in a bead mill (RetschMM300, Haan, Germany; 30 Hz, 90 s) at 4°C with
817 zirconium oxide grinding beads or ground by mortar and pestle for bigger sample volumes. For Western
818 Blotting, SDS loading buffer was added and the sample boiled at 95°C for 10 min. Lysates were cleared by
819 centrifugation at 16,000 g for 10 min and protein concentration was normalized by Amidoblack staining
820 (Sigma). Western blotting was performed following standard protocols as described below. 5 µg of lysate
821 was loaded per lane.

822 **Human Cell Culture conditions**

823 HeLa-Kyoto and HEK293T cells maintained in Dulbecco's modified Eagle's Medium (DMEM) with 10%
824 FBS, 1% L-Glutamine and 1% Penicillin/Streptomycin. Transfection was performed with GeneJuice
825 transfection reagent according to manufacturer's instructions. 100 µl of empty media was mixed with 3µL
826 of GeneJuice and after 5 min of incubation a total of 1 µg of DNA mixture per transfection was added.
827 After 20 minutes of incubation transfection mixture was added dropwise to the cells. Cells were incubated
828 with DNA for 24h. DNA containing media was removed and replaced with media.

829 **Lentiviral Knockdown**

830 Lentiviral transduced shRNA mediated knockdown of *c53* in HeLa cells:
831 The knockdown was performed in S2 conditions. HEK293T cells were seeded 24 h prior to transfection in
832 DMEM without antibiotics. At 50-60 % confluency, cells were transfected with 1 µg shRNA, 750 ng
833 psPAX2 and 250 ng pMD2.G utilizing 6 µL of GeneJuice in 250 µL of empty DMEM. After 48 h of

834 incubation the virus containing media was harvested and mixed 1:1 with full media. This mixture was
835 applied to HeLa cells that were seeded 24 h prior. Polybrene was added to a final concentration of 4 µg/ml.
836 After 24 h of incubation the medium on target cells was exchanged with full media. After 24h, selection
837 with 2 µg/ml Puromycin was started. No living cells were observed in a control plate after 24 h. After
838 splitting cells in S2 conditions, cells were transferred into S1 conditions.

839 **Autophagy Flux Assay in Human cell culture**

840 Cells were seeded 24 h prior to treatment. At 50-60 % confluency treatments were started by replacing
841 media containing the indicated drugs or full media (untreated). Tunicamycin was added with a final
842 concentration of 2.5 µg/ml and Torin with a final concentration of 3 µM. The treatments were stopped after
843 16h by removing the media and washing the cells with 1xPBS. A 2 h recovery period was started by adding
844 either media containing 100 nM Bafilomycin A1 or full media. Cells were put on ice and lysed with 100
845 µL of Lysis buffer (50 mM HEPES, 150 mM NaCl, 1 mM EDTA, 1 mM EGTA, 25 mM NaF, 10 µM
846 $ZnCl_2$, 1% Triton X-100 and 10% Glycerol) per well. After centrifugation, supernatant was mixed 1:1 with
847 2x Laemmli Buffer and denatured by heating to 95°C for 5min.
848 Each sample was loaded onto a 4-20% SDS-PAGE gradient gel (BioRad) and electrophoresis was run at
849 100V for 1,5h.

850 **Western Blotting**

851 SDS-PAGE was performed using gradient 4-20% Mini-PROTEAN® TGX Precast Protein Gels (BioRad).
852 Blotting on nitrocellulose membranes was performed using a semi-dry Turbo transfer blot system (BioRad).
853 For images of human LC3B, a wet transfer to PVDF membranes was performed at 200mA for 70 minutes.
854 Membranes were blocked with 5% skimmed milk or BSA in TBS and 0.1% Tween 20 (TBS-T) for 1h at
855 room temperature or at 4°C overnight. This was followed by incubation with primary and subsequent
856 secondary antibody conjugated to horseradish peroxidase. After 3 times 10 min washes with TBS-T, the
857 immune-reaction was developed using ECL Super-Pico Plus (Thermo) and detected with ChemiDoc Touch
858 Imaging System (BioRad).

859 **Western Blot Image Quantification**

860 Protein bands intensities were quantified with Image Lab 6 (BioRad). Equal rectangles were drawn around
861 the total protein gel lane and the band of interest. The lane profile was obtained by subtracting the mean
862 intensity of the background. The adjusted volume of the peak in the profile was taken as a measure of the
863 band intensity. The protein band of interest was normalized for the total protein level of the whole lane.
864 Average relative intensities and a standard error of at least 3 independent experiments were calculated.

865 **Chemicals and Antibodies**

866 To generate *At*C53 antibody, purified protein was sent to Eurogentec for immunization of rabbits via their
867 28-day program. The final bleed was purified on column conjugated with the purified protein.

868 ***In-vitro* Pulldowns**

869 For pulldown experiments, 10 µl of glutathione magnetic agarose beads (Pierce™ Glutathione Magnetic
870 Agarose Beads, Thermo Scientific™) were equilibrated by washing them 2 times with wash buffer (100
871 mM Sodium Phosphate pH 7.2, 300 mM NaCl, 1 mM DTT, 0.01% (v/v) IGEPAL). Normalized *E. coli*
872 clarified lysates or purified proteins were mixed, according to the experiment, added to the washed beads
873 and incubated on an end-over-end rotator for 1hr at 4°C. Beads were washed 5 times in 1 ml wash buffer.
874 Bound proteins were eluted by adding 100 µl Laemmli buffer. Samples were analysed by western blotting
875 or Coomassie staining.

876 **Yeast two hybrid assay (Y2H)**

877 Yeast two hybrid assay (Y2H) was performed according to the Mathmaker™ GAL4 Two hybrid system
878 (Clonetech®) following the protocol from the manufacture. Different genes were fused in frame to GAL4
879 activation domain of the prey vector pGADT7 and GAL4 binding domain from the bait vector pGBKT7.
880 Split-GFP was used as positive control. Combinations of pGADT7 and pGBKT7 vectors carrying the
881 different genes were transformed in the yeast strains Y187 (MAT α) and AH109 (MAT a), respectively.
882 After mating between bait and prey strains, the diploid yeast was selected for growth on (SD)-Leu/-Trp,
883 (SD)-Leu/-Trp/-His and (SD)-Leu/-Trp/-His/-Ade plates at 28°C for 2 to 4 days.

884 ***In planta* Co-Immunoprecipitation**

885 0.5 – 1 g seedlings were grown in liquid and treated as described under section Autophagy Flux Assay.
886 After grinding of frozen samples, G-TEN buffer (10% Glycerole, 50 mM Tris/HCl pH 7.5, 1mM EDTA,

887 300 mM NaCl, 1 mM DTT, 0.1% [v/v] Nonidet P-40/Igepal, Complete protease inhibitor tablet) was added,
888 vortexed, and lysates were cleared by centrifugation at 16 000 g for 10 min at 4°C. Protein concentration
889 was equally adjusted using Bradford protein assay (Sigma).
890 25 µl of GFP-Trap_A beads (Chromotek) were equilibrated and added to each lysate and incubated for 2 h
891 at 4°C on a turning wheel. Beads were washed 3 times with 1 mL G-TEN buffer.
892 For Western Blot analysis, beads were resuspended in 30 µl SDS-loading buffer (116 mM Tris-HCl pH 6.8,
893 4.9% glycerol, 10 mM DTT, 8% SDS). On-bead bound proteins were eluted by boiling the beads for 10
894 min at 70 °C and analysed by western blotting with indicated antibodies.
895 For mass spectrometry experiments, the beads were further washed 5 times with mass spectrometry
896 compatible buffer (50 mM Tris/HCl pH 7.5, 1mM EDTA). Buffer resuspended beads were then submitted
897 for trypsin digestion.
898 **Microscopy-based protein-protein interaction assays**
899 Bead-bound bait proteins were incubated with fluorescently labelled prey protein as described previously
900 by Turco *et al.* 2019 (Turco et al., 2019).
901 10 µl of Glutathione Sepharose 4B beads (GE Healthcare, average diameter 90mm) were incubated for 30
902 min at 4 °C (16 rpm horizontal rotation) with GST-tagged bait proteins (4 mg/mL for GST and GST-FIP200
903 CTR). The beads were washed 2 times in 10x bead volume of washing buffer (25 mM HEPES pH 7.5, 150
904 mM NaCl, 1 mM DTT). The buffer was removed, and the beads were resuspended 1:1 in washing buffer.
905 10 µL of a 2-5 µM dilution of fluorescently labelled binding partners (GFP, C53-GFP and GFP-p62) were
906 added to the bead suspension and incubated for 30-60 min at room temperature before imaging with a Zeiss
907 LSM700 confocal microscope with 20 X magnification. For Quantification the maximum gray value along
908 the diameter of each bead ($n \geq 15$) was measured.
909 **Mass Spectrometry (TMT) and Analysis**
910 MS/MS Data Analysis: Raw files were processed with Proteome Discoverer (version 2.3, Thermo Fisher
911 Scientific, Bremen, Germany). Database searches were performed using MS Amanda (version 2.3.0.14114)
912 (Dorfer et al., 2014) against the TAIR10 database (32785 sequences). The raw files were loaded as fractions
913 into the processing workflow. Carbamidomethylation of cysteine and TMT on peptide N-termini were

914 specified as fixed modifications, phosphorylation on serine, threonine and tyrosine, oxidation of
915 methionine, deamidation of asparagine and glutamine, TMT on lysine, carbamylation on peptide N-termini
916 and acetylation on protein N-termini were set as dynamic modifications. Trypsin was defined as the
917 proteolytic enzyme, cleaving after lysine or arginine. Up to two missed cleavages were allowed. Precursor
918 and fragment ion tolerance were set to 5 ppm and 15 ppm respectively. Identified spectra were rescored
919 using Percolator (Käll et al., 2007), and filtered to 0.5% FDR at the peptide spectrum match level. Protein
920 grouping was performed in Proteome Discoverer applying strict parsimony principle. Proteins were
921 subsequently filtered to a false discovery rate of 1% at protein level. Phosphorylation sites were localized
922 using IMP-ptmRS implemented in Proteome Discoverer using a probability cut-off of >75% for
923 unambiguous site localization.
924 TMT-quantification: TMT Reporter ion S/N values were extracted from the most confident centroid mass
925 within an integration tolerance of 20 ppm. PSMs with average TMT reporter S/N values below 10 as well
926 as PSMs showing more than 50% co-isolation were removed. Protein quantification was determined based
927 on unique peptides only. Samples were sum normalized and missing values were imputed by the 5%
928 quantile of the reporter intensity in the respective sample. Statistical significance of differentially abundant
929 proteins was determined using limma (Smyth, 2004). Gene Ontology (Ashburner et al., 2000) enrichment
930 was determined using DAVID (Dennis et al., 2003) (version 6.8). Cross species comparison of regulated
931 proteins was performed by mapping proteins to ortholog clusters available in eggnog (Huerta-Cepas et al.,
932 2015). Proteins containing signal peptides were predicted using SignalP 5.0 (Almagro Armenteros et al.,
933 2019).
934 **Peptide array**
935 High density peptide array analysis was performed commercially by PEPperPRINT. This comprised a full
936 substitution scan of wild type peptide GVSEWDPILEELQEM, with exchange of all amino acid positions
937 with 23 amino acids including citrulline (Z), methyl-alanine (O) and D-alanine (U). The analysis also
938 included an N- and C-terminal deletion series of wild type peptide GVSEWDPILEELQEM; an additional
939 32 spots of custom control peptide KPLDFDWEIVLEEQ, and acidic variants of this control peptide
940 involving exchanges of selected amino acid positions with glutamic acid €. The resulting peptide

941 microarrays contained 416 different linear peptides printed at least in triplicate (1,412 peptide spots; wild
942 type peptides were printed with a higher frequency), and were framed by HA (YPYDVPDYAG, 88 spots)
943 control peptides (See Table S1 for the array map).
944 Peptide microarrays were pre-stained with rabbit anti-GST Dylight680 at a dilution of 1:2000 to investigate
945 background interactions with the variants of wild type peptides GVSEWDPILEELQEM and
946 KPLDFDWEIVLEEQ that could interfere with the main assays. Subsequent incubation of other peptide
947 microarrays with proteins GST-ATG8A and GST at a concentration of 10 µg/ml in incubation buffer was
948 followed by staining with secondary antibody rabbit anti-GST Dylight680 and read-out at a scanning
949 intensity of 7 (red). The control staining of the HA epitopes with control antibody mouse monoclonal anti-
950 HA (12CA5) DyLight800 was finally done as an internal quality control to confirm the assay quality and
951 the peptide microarray integrity. Read-out of the control staining was performed at a scanning intensity of
952 7/7 (red/green).
953 Quantification of spot intensities and peptide annotation were based on the 16-bit grey scale tiff files at a
954 scanning intensity of 7 that exhibit a higher dynamic range than the 24-bit colorized tiff files; microarray
955 image analysis was done with PepSlide® Analyzer. A software algorithm breaks down fluorescence
956 intensities of each spot into raw, foreground and background signal (see "Raw Data" tabs), and calculates
957 averaged median foreground intensities and spot-to-spot deviations of spot duplicates.
958 **Microscopy Methods**
959 Preparation of *Arabidopsis thaliana* samples for confocal imaging:
960 4d old seedlings were treated as indicated under the autophagy flux assay section. Seedlings were imaged
961 between 3h - 6h of drug incubation. Roots were placed on a microscope slide with indicated treatment
962 buffer and closed with coverslip. Imaging was performed in the root differentiation zone where root hair
963 growth starts.
964 Preparation of human cell samples for confocal imaging:
965 Transfected and treated cells were grown on coverslips and fixed utilizing 0.4% Paraformaldehyde solution
966 in PBS for 30min. Fixed cells were mounted in VectaShield mounting medium without DAPI and sealed
967 using clear nail polish.

968 Confocal imaging:

969 Samples were imaged at an upright ZEISS LSM800 or LSM 780 confocal microscope (Zeiss) with an
970 Apochromat 40x or 63x objective lens at 1x magnification.
971 Excitation/detection parameters for GFP and mCherry were 488 nm/463 nm and 510 nm and 561 nm/569
972 to 635 nm respectively, and sequential scanning mode was used for colocalization of both fluorophores.
973 Identical settings, including an optical section thickness of 2 µm per z-stack, were used during the
974 acquisition for sample comparison, and the images processed using identical parameters. Confocal images
975 were processed with ZEN (version 2011) and ImageJ (version 1.48v) software.

976 Image Quantification:

977 Autophagic puncta were counted using ImageJ. Several (at least five) z-stack merged images were manually
978 background subtracted, thresholded and the same threshold value was applied to all the images and
979 replicates of the same experiment. The image was converted to eight-bit grayscale and then counted for
980 ATG8 puncta either manually or by the Particle Analyzer function of ImageJ. The average number of
981 autophagosomes per z-stack was averaged between 10 or more different roots.
982 Colocalization analysis was performed by calculating Pearson's correlation coefficient as previously
983 described using ImageJ software with the plug-in JACoP (BOLTE and CORDELIÈRES, 2006). Values
984 near 1 represent almost perfect correlation, whereas values near 0 reflect no correlation. The average
985 Pearson's correlation coefficient was determined in 5 or more different roots.

986 Ultrastructural analyses using immunogold labelling electron microscopy:

987 **TEM experiments using mCherry and native AtC53 antibodies**

988 For high pressure freezing, 5-day old *Arabidopsis* seedling roots expressing AtC53-mCherry were cut and
989 high-pressure frozen (EM PACT2, Leica, Germany), prior to subsequent freeze substitution in acetone
990 containing 0.4% uranyl acetate at −85 °C in an AFS freeze-substitution unit (Leica, Wetzlar, Germany).
991 After gradient infiltration with increasing concentration of HM20, root samples were embedded and
992 ultraviolet polymerized for ultra-thin sectioning and imaging. TEM images were captured by an 80 kV
993 Hitachi H-7650 transmission electron microscope (Hitachi High-Technologies Corporation, Japan) with a
994 charge-coupled devise camera. IEM analysis were performed as previously described (Zhuang et al., 2017).

995 **TEM experiments using GFP antibodies**

996 *Arabidopsis* roots were fixed in 2% paraformaldehyde and 0.2% glutaraldehyde (both EM-grade, EMS,
997 USA) in 0.1 M PHEM buffer (pH 7) for 2h at RT, then overnight at 4°C. The fixed roots were embedded
998 in 12% gelatin and cut into 1 mm^3 blocks which were immersed in 2.3 M sucrose overnight at 4°C. These
999 blocks were mounted onto a Leica specimen carrier (Leica Microsystems, Austria) and frozen in liquid
1000 nitrogen. With a Leica UCT/FCS cryo-ultramicrotome (Leica Microsystems, Austria) the frozen blocks
1001 were cut into ultra-thin sections at a nominal thickness of 60nm at -120°C. A mixture of 2% methylcellulose
1002 (25 centipoises) and 2.3 M sucrose in a ratio of 1:1 was used as a pick-up solution. Sections were picked
1003 up onto 200 mesh Ni grids (Gilder Grids, UK) with a carbon coated formvar film (Agar Scientific, UK).
1004 Fixation, embedding and cryo-sectioning was conducted as described by Tokuyasu et al., 1973.

1005 Immunolabeling:

1006 Prior to immunolabeling, grids were placed on plates with solidified 2% gelatine and warmed up to 37 °C
1007 for 20 min to remove the pick-up solution. After quenching of free aldehyde-groups with glycine (0.1% for
1008 15 min), a blocking step with 1% BSA (fraction V) in 0.1 M Sörensen phosphate buffer (pH 7.4) was
1009 performed for 40 min. The grids were incubated in primary antibody, rabbit polyclonal to GFP (ab6556,
1010 Abcam, UK), diluted 1:125 in 0.1 M Sörensen phosphate buffer over night at 4°C, followed by a 2h
1011 incubation in the secondary antibody, a goat-anti-rabbit antibody coupled with 6 nm gold (GAR 6 nm,
1012 Aurion, The Netherlands), diluted 1:20 in 0.1 M Sörensen phosphate buffer, performed at RT. The sections
1013 were stained with 4% uranyl acetate (Merck, Germany) and 2% methylcellulose at a ratio of 1:9 (on ice).
1014 All labeling steps were conducted in a wet chamber. The sections were inspected using a FEI Morgagni
1015 268D TEM (FEI, The Netherlands) operated at 80kV. Electron micrographs were acquired using an 11-
1016 megapixel Morada CCD camera from Olympus-SIS (Germany).

1017 **Statistical analysis**

1018 Statistical analyses were performed with GraphPad Prism 8 software. For all the quantifications described
1019 above, statistical analysis was performed. Statistical significance of differences between two experimental
1020 groups was assessed wherever applicable by either a two-tailed Student's t-test if the variances were not
1021 significantly different according to the F test, or using a non-parametric test (Mann-Whitney or Kruskal-

1022 Wallis with Dunn's post-hoc test for multiple comparisons) if the variances were significantly different (p
1023 < 0.05). Differences between two data sets were considered significant at $p < 0.05$ (*) ($p < 0.01$ (**); $p <$
1024 0.001 (***); $p < 0.0001$ (****); n.s., not significant.

1025 **Biophysical Characterization**

1026 **Protein purification**

1027 Recombinant proteins were produced using *E. coli* strain Rosetta2(DE3)pLysS grown in 2x TY media at
1028 37°C to an A600 of 0.4–0.6 followed by induction with 300 µM IPTG and overnight incubation at 18°C.
1029 Pelleted cells were resuspended in lysis buffer (100 mM Sodium Phosphate pH 7.0, 300 mM NaCl)
1030 containing protease inhibitors (Complete™, Roche) and sonicated. The clarified lysate was first purified
1031 by affinity, by using HisTrap FF (GE HealthCare) columns. The proteins were eluted with lysis buffer
1032 containing 500 mM Imidazole. The eluted fraction was buffer exchanged to 10 mM Sodium Phosphate pH
1033 7.0, 100 mM NaCl and loaded either on Cation Exchange, Resource S, or Anion Exchange, Resource Q,
1034 chromatography columns. The proteins were eluted by NaCl gradient (50% in 20 CV). Finally, the proteins
1035 were separated by Size Exclusion Chromatography with HiLoad® 16/600 Superdex® 200 pg or HiLoad®
1036 16/600 Superdex® 75 pg, which were previously equilibrated in 50 mM Sodium Phosphate pH 7.0, 100
1037 mM NaCl. The proteins were concentrated using Vivaspin concentrators (3000, 5000, 10000 or 30000
1038 MWCO). Protein concentration was calculated from the UV absorption at 280 nm by DS-11 FX+
1039 Spectrophotometer (DeNovix).

1040 **Surface plasmon resonance analysis**

1041 Binding of AIM *wt* (EPLDFDWEIVLEEEM) and AIM mutant (EPLDFDAEIALEEEM) peptide to GST-
1042 GABARAP and GST-ATG8A, respectively, was investigated by surface plasmon resonance analysis using
1043 a Biacore T200 instrument (GE Healthcare) operated at 25°C. In additione, AIM-dependent binding of
1044 *Hs*C53 and *At*C53 to GST-GABARAP and GST-ATG8A were studied. The running buffer used for all
1045 experiments was 50 mM sodium phosphate pH 7.0 supplemented with 100 mM NaCl, 0.05% (v/v) Tween-
1046 20 and 0.1% (w/v) bovine serum albumin.

1047 Polyclonal anti-GST antibodies (GST Capture Kit, GE Healthcare) were amine coupled on to a Series S
1048 CM5 sensor chip (GE Healthcare) using 2 adjacent flow cells (i.e. the reference and active cell) according
1049 to the manufacturer's instructions.
1050 To determine specific binding, GST-GABARAP or GST-ATG8A were captured on the active cell
1051 (concentration: 5 µg/ml; contact time: 30 seconds; flow rate: 10 µl/min) and GST was captured on the
1052 reference cell (concentration: 10 µg/ml; contact time: 30 seconds; flow rate: 10 µl/min) to perform
1053 background subtraction.
1054 To qualitatively show whether the analytes, *Hs*C53, *Hs*C53 123A (i.e. HsC53$^{W269A, W294A, W312A}$), *At*C53 and
1055 *At*C53 1234A (i.e. *At*C53$^{W276A, W287A, Y304A, W335A}$), interact or do not interact in an AIM-dependent manner
1056 with GST-GABARAP or GST-ATG8A, the 2 flow cells were exposed to 4 sets of double consecutive
1057 injections (1st set: 10 µM analyte, running buffer; 2nd set: 10 µM analyte, 10 µM analyte; 3rd set: 10 µM
1058 analyte, 10 µM analyte + 6.4 µM AIM *wt* peptide; 4th set: 10 µM analyte, 10 µM analyte + 6.4 µM AIM
1059 mutant peptide. Contact time 1st injection: 30 seconds; contact time 2nd injection: 30 seconds; dissociation
1060 time: 60 seconds; flow rate: 30 µl/min).
1061 To quantify the binding affinities of the AIM *wt* peptide to GST-ATG8 or GST-GABARAP, multi-cycle
1062 kinetic experiments with increasing concentrations of the AIM *wt* peptide (25, 50, 100, 200, 400, 800,
1063 1600, 3200 nM and 400 nM as internal replicates) were performed (contact time: 60 seconds; dissociation
1064 time: 60 seconds; flow rate: 30 µl/min). As a negative control, the chip was exposed to 3200 nM of the
1065 AIM mutant peptide (contact time: 60 seconds; dissociation time: 60 seconds; flow rate: 30 µl/min).
1066 To quantify the apparent binding affinity of the AIM *wt* peptide to GST-GABARAP in presence of *Hs*C53,
1067 multi-cycle kinetic experiments with increasing concentrations of the AIM peptide (0, 25, 50, 100, 200,
1068 400, 800, 1600, 3200 nM and 400 nM as internal replicates), containing 10 µM of *Hs*C53, in running buffer
1069 (contact time: 60 seconds; dissociation time: 60 seconds; flow rate: 30 µl/min). For negative controls, the
1070 chip was exposed to 3200 nM of the AIM mutant peptide, containing 10 µM of *Hs*C53 or 10 µM of
1071 *Hs*C53 123A, and to 3200 nM of the AIM *wt* peptide, containing 10 µM of *Hs*C53 123A (contact time: 60
1072 seconds; dissociation time: 60 seconds; flow rate: 30 µl/min).

1073 To quantify the apparent binding affinity of the AIM *wt* peptide to GST-ATG8A in the presence of *At*C53,
1074 multi-cycle kinetic experiments with increasing concentrations of the AIM peptide (0, 50, 100, 200, 400,
1075 800, 1600, 3200, 6400, 12800 nM and 400 nM as internal replicate) containing 10 µM of *At*C53 were
1076 performed (contact time: 60 seconds; dissociation time: 60 seconds; flow rate: 30 µl/min). As negative
1077 controls, the chip was exposed to 6400 nM of the AIM mutant peptide, containing 10 µM of *At*C53 or 10
1078 µM of *At*C53 1234A, and to 6400 nM of the AIM *wt* peptide, containing 10 µM of *At*C53 1234A (contact
1079 time: 60 seconds; dissociation time: 60 seconds; flow rate: 30 µl/min).
1080 After each cycle, regeneration was performed with 2 injections of 10 mM glycine-HCl pH 2.1 for 120
1081 seconds at a flow rate of 10 µL/min.
1082 The sensograms obtained were analysed with Biacore T200 Evaluation software (version 3.1) by global
1083 fitting of the data to a 1:1 steady-state affinity model.
1084 Molecular weights and sources of the proteins for the SPR experiments are reported in the following table:

Sample name	Source	MW (Da)
AIM wt peptide	Synthetized *in house*	1894.08
AIM mutant peptide		1750.89
*Hs*C53	*Escherichia coli* recombinant expression	59191.15
*Hs*C53 123A		58758.66
*At*C53		64399.57
*At*C53 1234A		63962.07
GST-GABARAP		42458.87
GST-ATG8A		42366.85
GST		27898.33

1085

1086 Calculation for the apparent $\boldsymbol{K_D}$ ($\boldsymbol{K'_D}$) of the AIM^{wt} was done by using the following formula (Nelson,
1087 David L. Lehninger Principles Of Biochemistry. New York: W.H. Freeman, 2008):

1088 $$K'_D AIM^{wt} = \alpha K_D(AIM^{wt})$$

1089 Where, $\alpha = 1 + \frac{I}{K_i}$, $K_i = K_D(C53)$ and $[I] = [C53]$

1090 Then:

1091 $$K_D(C53) = \frac{K_D(AIM^{wt})[C53]}{K'_D(AIM^{wt}) - K_D(AIM^{wt})}$$

1092 **Isothermal titration calorimetry (ITC)**

1093 All experiments were carried out at 25°C in 50 mM sodium phosphate buffer pH 7.0, 100 mM NaCl, using
1094 the PEAQ-ITC Automated (Malvern Panalytical Ltd). For protein-protein interactions, the calorimetric cell
1095 was filled with 40 µM GABARAP or ATG8A and titrated with 250 µM *Hs*C53 or *At*C53 IDRs, respectively.
1096 A single injection of 0.4 µl of *Hs*C53 or *At*C53 IDRs (not taken into account) was followed by 18 injections
1097 of 2 µl each. Injections were made at 150 sec intervals with a duration of 4 sec and a stirring speed of 750
1098 rpm. The reference power was set to 10 µcal/sec, the feedback mode was set to *high*. For protein-peptide
1099 interactions, the calorimetric cell was filled with 40 µM GABARAP or ATG8A and titrated with 600 µM
1100 peptide from the syringe. The titrations were performed as described above. For the control experiments,
1101 equivalent volumes of the IDRs, or the peptides, were titrated to buffer, equivalent volumes of buffer were
1102 titrated to GABARAP or ATG8A and equivalent volumes of buffer were titrated to buffer, using the
1103 parameters above. The raw titration data were integrated, corrected for the controls and fitted to a one-set-
1104 of-sites binding model using the PEAQ-ITC analysis software (Version 1.22).

1105 **Sample preparation for native MS experiments.**

1106 Proteins were buffer exchanged into ammonium acetate using BioRad Micro Bio-Spin 6 Columns and
1107 concentrations were measured using DS-11 FX+ Spectrophotometer (DeNovix).

1108 **Mass spectrometry measurements.**

1109 Native mass spectrometry experiments were carried out on a Synapt G2S*i* instrument (Waters, Manchester,
1110 UK) with a nanoelectrospray ionisation source. Mass calibration was performed by a separate infusion of
1111 NaI cluster ions. Solutions were ionised through a positive potential applied to metal-coated borosilicate
1112 capillaries (Thermo Scientific). The following instrument parameters were used; capillary voltage 1.3 kV,
1113 sample cone voltage 40 V, extractor source offset 30 V, source temperature 40 °C, trap gas 3 mL/min. A
1114 higher capillary voltage (1.9 kV) was required for ionization of the 1:2 AtC53-AtG8A complex. Data were
1115 processed using Masslynx V4.1 and spectra were plotted using R. Peaks were matched to protein complexes
1116 by comparing measured m/z values with expected m/z values calculated from the mass of individual
1117 proteins which are given in table below.

Protein	Expected mass from sequence / Da	Measured Mass/ Da
AtC53	64 399.6	64 401.3

AtC53-1234A	63 962.1	63 976.7
HsC53	59 191.1	59 193.0
AtG8A	15 965.3	15 964.0
GABARAP	15 968.3	15 968.2
AtC53-IDR	9050.5	9050.5
HsC53-IDR	6060.2	6059.5

1118

1119 **Circular dichroism spectroscopy**

1120 CD spectroscopy experiments were performed using a Chirascan-Plus CD spectrophotometer (Applied
1121 Photophysics). Purified proteins in 50mM sodium phosphate pH 7.0, 100mM NaCl were diluted to
1122 approximately 0.2 mg/ml and spin-filtered with an 0.1µm filter. CD measurements were carried out in a
1123 quartz glass cuvette with 0.5 mm path length. To obtain overall CD spectra, wavelength scans between
1124 180nm and 260nm were collected at 25°C using a 1.0 nm bandwidth, 0.5 nm step size, and time per point
1125 of 0.5 s. Both CD and absorbance data were collected at the same time over three accumulations and
1126 averaged. CD data at wavelengths where the absorptivity was above 2.5 are not shown (data below 194nm).
1127 The raw data in millidegree units were corrected for background and drift (Θ_{dcorr}). Subsequently the
1128 differential molar extinction coefficient per peptide bond (Δε) was calculated, taking into account the
1129 absorptivity measured at 205nm (A_{205}) and the calculated protein extinction coefficient at 205nm (ε_{205})
1130 using the equation

1131 $$\Delta\varepsilon = \frac{\Theta_{dcorr} \cdot \varepsilon_{205}}{10 \cdot A_{205} \cdot (N-1) \cdot 3298}$$

1132

1133 **Materials**
1134
1135 Experimental Model/Cell lines

Organism	Background	Supplier
Arabidopsis thaliana	Col-0	
Marchantia Polymorpha	Tak-1	
Human Tumor Cell line	HeLa-Kyoto	Fumiyo Ikeda
Human Embryonic Kidney Cells	HEK293T	Fumiyo Ikeda

1136

1137 Plant Mutants

Genotype	Gene ID	Preparation/T-DNA line	Supplier	Reference
c53	At5g06830	CRISPR/Cas9	this study	
ddrgk1	At4g27120	CRISPR/Cas9	this study	
ufm1	At1g77710	CRISPR/Cas9	this study	
atg2	At3g19190	EMS-mutant (Gln803stop)	Morten Peterson	Wang *et al.* Plant Journal (2011)
atg5	At5g17290	SAIL_129B07	NASC (N39993)	Scholl *et al.* Plant Phys. (2000)
ufl1	At3g46220	SALK_022517C	NASC (N685434)	Scholl *et al.* Plant Phys. (2000)
uba5	At1g05350	SALK_134012	NASC (N634012)	Scholl *et al.* Plant Phys. (2000)
ufsp2	At3g48380	SAIL_607_G10	NASC (N826004)	Scholl *et al.* Plant Phys. (2000)
ufc1	At1g27530	SALK_112532	NASC (N678973)	Scholl *et al.* Plant Phys. (2000)
ire1a/b	At2G17520/ At5G24360	SALK_018112/SAIL_238_F07	Karolina Pajerowska-Mukhtar	McCormack et al. Front. in plant sci. (2015)
bzip 17/28	At2g40950/ At3g10800	SALK_104326/ SALK_132285	Kazuo Shinozaki	Kim *et al.* Plant Phys. (2018)

1138

1139 Plant Lines (all Col-0 background)

Name	Selection	Supplier	Reference
pUbi::mCherry-ATG8A	Alli-mCherry	this study	
pUbi::mCherry-ATG8E	HygB	Liwen Jiang	Hu *et al.* J. Integr. Plant Biol. (2020)
pUbi::mCherry-ATG8E x *atg5*	HygB/Basta	this study	
pUbi::GFP-ATG8A	Alli-YFP	this study	
pUbi::GFP-ATG8B	Alli-YFP	this study	
pUbi::GFP-ATG8C	Alli-YFP	this study	
pUbi::GFP-ATG8D	Alli-YFP	this study	
pUbi::GFP-ATG8E	Alli-YFP	this study	
pUbi::GFP-ATG8F	Alli-YFP	this study	
pUbi::GFP-ATG8G	Alli-YFP	this study	
pUbi::GFP-ATG8H	Alli-YFP	this study	
pUbi::GFP-ATG8I	Alli-YFP	this study	
pUbi::C53-mCherry	Kan	this study	
pUbi::C53-mCherry x *atg2*	Kan	this study	
pUbi::C53-mCherry x *atg5*	Kan	this study	
pUbi::C53-mCherry x *ufl1*	Kan	this study	
pUbi::C53-mCherry x *ddrgk1*	Kan	this study	
pUbi::C53-mCherry x *ire1a/b*	Kan	this study	
pUbi::C53-mCherry x pUbi::GFP-ATG8A	Alli-YFP/Kan	this study	
pUbi::C53-mCherry x wave-YFP	Kan/Bas	this study	
pUbi::C53-mCherry x p35S::GFP-HDEL	Kan	this study	
pUbi::C53-mCherry x p35S::GFP-ATG11	Kan/HygB	this study	

pUbi::C53-mCherry x pUbi::UFL1-GFP	Kan/Alli-YFP	this study	
pUbi::C53-mCherry x pUbi::DDRGK1-GFP	Kan/Alli-YFP	this study	
pUbi::C53-mCherry x GCSI-SUBEX-C57Y-GFP	Kan/HygB	this study/ Richard Strasser	Shin *et al.* The Plant Journal (2018)
pUbi::C53-mCherry x MNS1-SUBEX-GFP	Kan/HygB	this study/ Richard Strasser	Shin *et al.* The Plant Journal (2018)
pUbi::C53-GFP	Alli-YFP	this study	
pUbi::C53-GFP x *c53*	Alli-YFP	this study	
pUbi::C53$^{sAIM(W276A,W287A,Y304A,W335A)}$-GFP x *c53*	Alli-YFP	this study	
pUbi::C53-GFP x SP-mRFP-SUBEX-C57Y-EMP12	Alli-YFP/HygB	this study/ Richard Strasser	Shin *et al.* Plant Journal (2018)
pUbi::UFL1-GFP	Alli-YFP	this study	
pUbi::DDRGK1-GFP	Alli-YFP	this study	
p35S::GFP-HDEL (ER-gk)	Kan	NASC	N16251
wave-YFP	BASTA	Niko Geldner	Geldner et al. The Plant Journal (2009)

Bacterial Strains

Organism	Strain	Supplier
E. coli	DH5α	In-house facility
	BL21 (DE3)	In-house facility
	Rosetta2 (DE3) pLysS	In-house facility
Agrobacterium tumefaciens	GV3101 (pSoup)	In-house facility

Oligonucleotides – gRNAs :

Organism	Name	5‘ – 3‘ Sequence
Arabidopsis th.	C53_BsF	ATATATGGTCTCGATTGATATCACCTTCTCTCGTCTGTT
	C53_F0	TGATATCACCTTCTCTCGTCTGTTTTAGAGCTAGAAATAGC
	C53_R0	AACCAAGGCCTTGGCTTTCTTCCAATCTCTTAGTCGACTCTAC
	C53_BsR	ATTATTGGTCTCGAAACCAAGGCCTTGGCTTTCTTCCAA
	DDRGK1_BsF	ATATATGGTCTCGATTGAGAGATGCTAGATCACGGGGTT
	DDRGK1_F0	TGAGAGATGCTAGATCACGGGGTTTTAGAGCTAGAAATAGC
	DDRGK1_BsR	AACTGCACTTCCTCTGTAGTACCAATCTCTTAGTCGACTCTAC
	DDRGK1_R0	ATTATTGGTCTCGAAACTGCACTTCCTCTGTAGTACCAA
	UFM1_BsF	ATATATGGTCTCGATTGGAGGAGATTCAGATTAGCA GTT
	UFM1_F0	TGGAGGAGATTCAGATTAGCA GTTTTAGAGCTAGAAATAGC
	UFM1_R0	AACGAAGGAGCTCCGTTCACGGCAATCTCTTAGTCGACTCTAC
	UFM1_BsR	ATTATTGGTCTCGAAACGAAGGAGCTCCGTTCACGGCAA

Marchantia p.	C53- sgRNA1-FWD	CTCGTCAATCGGAAGAGACAGAGC
	C53- sgRNA1-REV	AAACGCTCTGTCTCTTCCGATTGA
	C53- sgRNA2-FWD	CTCGAAAGTTCTGCCCTGATGT
	C53- sgRNA2-REV	AAACACATCAGGGCAGAACTTT
	IRE1-sgRNA1-FWD	CTCGTACGTTAAAGGCGAATATGG
	IRE1-sgRNA1-REV	AAACCCATATTCGCCTTTAACGTA
	IRE1-sgRNA2-FWD	CTCGCATCAAAGGACCACCAGGGC
	IRE1-sgRNA2-REV	AAACGCCCTGGTGGTCCTTTGATG

1144
1145 Antibodies:

	Antibody	Host	Supplier	Cat. #	Working concentration
General	Anti-Rabbit IgG HRP-Conjugate	goat	Biorad	1706515	1:10000
	Anti-Mouse IgG-HRP Conjugate	goat	Biorad	1706516	1:10000
	mCherry	rabbit	Abcam	ab167453	1:5000
	His	mouse	Sigma Aldrich	H1029	1:5000
	GST HRP Conjugate	goat	GE Healthcare	RPN1236	1:1000
	GFP	rabbit	Invitrogen	A11122	1:3000
	GFP	mouse	Roche	11814460001	1:3000
	MBP	mouse	Sigma Aldrich	M1321-200UL	1:3000
	Streptavidin-HRP Conjugate	goat	GE Healthcare	GERPN1231-100UL	1:1000
Human	C53	mouse	SCBT	sc271671	1:1000
	LC3B	mouse	nanoTools	0260-100/LC3-2G6	1:100
	BIP3	rabbit	CST	3177	1:1000
	Vinculin	mouse	Sigma Aldrich	V9131	1:1000
	UFM1	rabbit	Abcam	ab108062	1:2000
Arabidopsis t.					
	ATG8A	rabbit	Agrisera	AS14 2811	1:1000
	C53	rabbit	this study	-	1:5000

1146
1147 Plasmids

Organism	Name	Supplier	Cat. #	Reference
E. coli				
	E. coli destination (expression) vector	This study		

	MBP-AtC53	This study		
	GST-ATG8A	This study		
	GST-ATG8A$^{LDS(YL50AA)}$	This study		
	GST-ATG8A$^{UDS(IFV77AAA)}$	This study		
	GST-ATG8B	This study		
	GST-ATG8C	This study		
	GST-ATG8D	This study		
	GST-ATG8E	This study		
	GST-ATG8F	This study		
	GST-ATG8G	This study		
	GST-ATG8H	This study		
	GST-ATG8I	This study		
	GST-GABARAP	This study		
	GST-GABARAPL1	This study		
	GST-GABARAPL2	This study		
	GST-LC3A	This study		
	GST-LC3B	This study		
	GST-LC3C	This study		
	GST-GABARAP$^{LDS(YL49AA)}$	This study		
	GST-GABARAP$^{(P52A)}$	This study		
	GST-GABARAP$^{(R67A)}$	This study		
	GST-GABARAP$^{(P52A, R67A)}$	This study		
	GST-GABARAP$^{(KK64AA)}$	This study		
	GST-MpATG8A	This study		
	GST-MpATG8A$^{LDS(YL50AA)}$	This study		
	GST-MpATG8B	This study		
	GST-MpATG8B$^{LDS(YL50AA)}$	This study		
	MBP-MpC53	This study		
	MBP-AtC53	This study		
	MBP-AtC53$^{N\text{-}IDR(1\text{-}372)}$	This study		
	MBP-AtC53$^{C\text{-}IDR(239\text{-}549)}$	This study		
	MBP-AtC53$^{IDR(239\text{-}372)}$	This study		
	MBP-AtC53$^{N\text{-}C(1\text{-}239,(KGSGSTSGSG)2,373\text{-}549)}$	This study		
	MBP-HsC53	This study		
	MBP-HsC53$^{N\text{-}IDR(1\text{-}316)}$	This study		
	MBP-HsC53$^{C\text{-}IDR(263\text{-}506)}$	This study		
	MBP-HsC53$^{IDR(263\text{-}316)}$	This study		
	MBP-HsC53$^{N\text{-}C(1\text{-}262, (KGSGSTSGSG),317\text{-}506)}$	This study		
	MBP-AtC53^{Y304A}	This study		
	MBP-AtC53$^{Y304A, 1A (W276A)}$	This study		
	MBP-AtC53$^{Y304A, 2A (W287A)}$	This study		
	MBP-AtC53$^{Y304A, 3A (W335A)}$	This study		
	MBP-AtC53$^{Y304A, 12A (W276A, W287A)}$	This study		
	MBP-AtC53$^{Y304A, 13A (W276A, W335A)}$	This study		
	MBP-AtC53$^{Y304A, 23A (W287A, W335A)}$	This study		
	MBP-AtC53$^{Y304A, 123A (W276A, W287A, W335A)}$	This study		
	MBP-HsC53$^{1A(W269A)}$	This study		
	MBP-HsC53$^{2A(W294A)}$	This study		
	MBP-HsC53$^{3A(W312A)}$	This study		
	MBP-HsC53$^{12A(W269A, W294A)}$	This study		
	MBP-HsC53$^{13A(W269A, W312A)}$	This study		

	MBP-HsC53$^{23A(W294A, W312A)}$	This study		
	MBP-HsC53$^{123A(W269A, W294A, W312A)}$	This study		
	MBP-AtC53$^{IDR\ sAIM\ (Y304A, W276A, W287A, W335A)}$	This study		
	MBP-HsC53$^{IDR\ sAIM(W269A, W294A, W312A)}$	This study		
	GST-AtUFL1	This study		
	GST-AtC53	This study		
	MBP	This study		
	Ts-ATG8A	This study		
	Ts-AtDDRGK1$^{(24-298)}$	This study		
	Ts-AtC53	This study		
	HIS6-ATG8A	This study		
	HIS6-GABARAP	This study		
	HIS6-AtC53	This study		
	HIS6-AtC53 $^{sAIM\ (Y304A, W276A, W287A, W335A)}$	This study		
	HIS6-HsC53	This study		
	HIS6-HsC53 $^{sAIM(W269A, W294A, W312A)}$	This study		
	GST	This study		
Plant				
	pUbi::C53-mCherry	this study		
	pUbi::C53-GFP	this study		
	pUbi::C53$^{sAIM(W276A,W287A,Y304A,W335A)}$-GFP	this study		
	pUbi::UFL1-GFP	this study		
	pUbi::DDRGK1-GFP	this study		
	pUbi::C53-GFP	this study		
	pUbi::mCherry-ATG8A	this study		
	pUbi::GFP-ATG8A	this study		
	pUbi::GFP-ATG8B	this study		
	pUbi::GFP-ATG8C	this study		
	pUbi::GFP-ATG8D	this study		
	pUbi::GFP-ATG8E	this study		
	pUbi::GFP-ATG8F	this study		
	pUbi::GFP-ATG8G	this study		
	pUbi::GFP-ATG8H	this study		
	pUbi::GFP-ATG8I	this study		
Human Cell Culture				
	psPAX2	Addgene	12260	Didier Trono
	pMD2.G	Addgene	12259	Didier Trono
	C53 shRNA in pLKO1	Honglin Li	Gift	Wu *et al. Cell Res* (2013).
	peGFP(N2)-HsC53-GFP	This study		
	peGFP(N2)-AtC53-GFP	This study		
	peGFP(N2)-HsC53^{sAIM}-GFP	This study		
	peGFP(N2)-AtC53	This study		
	pmCherry(N2)-HsC53-mCherry	This study		
	pmCherry-GABARAP-mCherry	Fumiyo Ikeda	Gift	
	mRFP-LAMTOR1	Sascha Martens	Gift	

	ER-K20	Addgene	133861	Wang *et al.* Cell Res. (2020)
	ERAD-C (pEGFP-GFP:CFTR$_{\Delta F508}$)	Ron R. Kopito	Gift	Leto *et al.* Mol. Cell (2019)
	ERAD-L (pcDNA3-NHK-GFP)	Ron R. Kopito	Gift	Leto *et al.* Mol. Cell (2019)
	ERAD-M (pMCB497-pTRE-INSIG1-GFP)	Ron R. Kopito	Gift	Leto *et al.* Mol. Cell (2019)
	pcDNA3-Erdj3-GFP-3Gly	Maya Schuldiner	Gift	Ast *et al.* Cell (2016)

1148
1149 General Chemicals

Name	Supplier	Cat. #
Vectashield	Vector	H-1000-10
GeneJuice	Sigma Aldrich Aldrich	70967
Phenolred	Sigma Aldrich Aldrich	P3252
Polybrene	Gift from Fumiyo Ikeda	
5x Transfer Buffer	BioRad	
Acrylamide		
Glycerol (87%)	Applichem	A0970
Glass beads (0.75-1mm)	Roth	A554.1
Glass beads (1.7-2.1mm)	Roth	A556.1
Glass beads (2.85-3.45mm)	Roth	A557.1
IGEPAL CA-630	Sigma Aldrich	I8896-50ml
Magnesium Chloride	Sigma Aldrich	M8266-100G
Precellys steel beads 2.8mm	peqlab	
Tris(2-carboxyethyl)-phosphine hydrochloride solution 0.5 M pH7	Sigma Aldrich	646547-10X1ML
Acrilamide/Bis-acrylamide, 30% solution, 37.5:1	Sigma Aldrich	
Bovine Serum Albumine	Sigma Aldrich	
Glycerol (87%)	Applichem	A0970
EDTA-free cOmplete Protease inhibitor Cocktail	Roche	4693159001
Tween-20	Sigma Aldrich	
TBS	In-house facility	
DMSO	Sigma Aldrich	
Isopropanol	Sigma Aldrich	
10x Transfer Buffer (wet)	In-house facility	
pH Stripes		
NaN3		
NaOH		
Ethanol		
Naphthol Blue (Amidoblack)	Sigma Aldrich	N3393-25G
Acetic Acid		
Methanol		
$ZnCl_2$	Gift from Fumiyo Ikeda	
Triton X-100		

NaF		
EGTA		
HEPES	In-house facility	
EDTA	Sigma Aldrich	E6760-100G
NaCl (sol.)	In-house facility	
Tris Buffers	In-house facility	
Bromophenolblue		
DTT	Sigma Aldrich	43815
SDS		
Glycerol		
APS		
TEMED		
Paraformaldehyd		
Thimerosal		
Sodium dihydrogen phosphate		
Sodium hydrogen phosphate		

Inhibitors and drugs

Name	Supplier	Cat. #
Tunicamycin	SCBT	sc-3506
Torin	SCBT	sc-396760
Bafilomycin A1	Abcam	ab120497
4μ8C	Sigma Aldrich	SML0949
KIRA6	MedChemExpress	HY-19708
Anisomycin (ANS)	Sigma Aldrich	A5862-0.5ml
DTT	Sigma Aldrich	43815
Concanamycin-A (conA)	Santa Cruz	sc-202111A
Cyclopiazonic acid (CPA)	Santa Cruz	sc-201510
Kifunensine (kif)	Santa Cruz	sc-201364A
Thapsigargin (Tg)	Santa Cruz	sc-24017

Media and supplements

Name	Supplier	Cat. #
FBS	Sigma Aldrich	F7524
PBS/PBS Tissue Culture	In-house facility	
LB	In-house facility	
2xTY	In-house facility	
TB	In-house facility	
DMEM	In-house facility	
SOC	In-house facility	
gamborg B5 vitamin mixture 1000X	Duchefa	G0415.0250
gamborg B5 medium (microsalt mixture)	Duchefa	M0302.0025
gamborg B5 medium (including vitamins)	Duchefa	G0210.0010
gamborg B5 medium (basal salt mixture)	Duchefa	G0209.0050
Murashige & Skoog vitamin mixture 1000X	Duchefa	M0409.0250

Murashige & Skoog micro salt mixture	Duchefa	M0301.0050
Murashige & Skoog macro salt mixture	Duchefa	M0305.0050
Murshige & Skoog Basal salt mixture with MES	Duchefa	M0254.0050
Murashige & Skoog without nitrogen	Caisson labs	
MES monohydrate	Applichem	A1074
Puromycin	Sigma Aldrich	P8833
Ampicillin	In-house facility	
Kanamycin	In-house facility	
Penicillin-Streptomycin	Sigma Aldrich	P4333
Trypsin	Thermo Fisher	25300054
L-Glutamine	Sigma Aldrich	G7513

Affinity matrices for purification and immuno-precipitation

Name	Supplier	Cat. #
GFP-Trap	Chromotek	Gta-20
Glutathion Sepharose 4	GE Healthcare	17-5132-01
Pierce™ Glutathione Magnetic Agarose Beads	Thermo Scientific™	78601
HisTrap FF 5 ml	GE Healthcare	17525501
HisTrap FF 1 ml	GE Healthcare	17531901
Resource Q 6 ml	GE Healthcare	17117901
Resource S 6 ml	GE Healthcare	17118001
HiPrep 26/10 Desalting	GE Healthcare	17508701
HiLoad 16/600 Superdex 75 pg	GE Healthcare	28989333
HiLoad 16/600 Superdex 200 pg	GE Healthcare	28989335
GSTrap FF	GE Healthcare	17513101

Software

Name	Company	Application
CLC main work bench 7	Qiagen	Cloning
Zen Software	Carl Zeiss	Microscopy
Image J (Fiji)	NIH	Image Quantification
Prism 8	Graph Pad	Statistics
Image Lab	BioRad	Western Blot Analysis
Adobe Illustrator 2020	Adobe Inc.	Graphics editing
RStudio 1.2.5019	RStudio, Inc	Graph plotting

1164 **References**

1165 Almagro Armenteros, J.J., Tsirigos, K.D., Sønderby, C.K., Petersen, T.N., Winther, O., Brunak, S., von
1166 Heijne, G., and Nielsen, H. (2019). SignalP 5.0 improves signal peptide predictions using deep neural
1167 networks. Nat. Biotechnol. *37*, 420–423.
1168 An, H., Ordureau, A., Paulo, J.A., Shoemaker, C.J., Denic, V., and Harper, J.W. (2019). TEX264 Is an
1169 Endoplasmic Reticulum-Resident ATG8-Interacting Protein Critical for ER Remodeling during Nutrient
1170 Stress. Mol. Cell *74*, 891-908.e10.
1171 Ashburner, M., Ball, C.A., Blake, J.A., Botstein, D., Butler, H., Cherry, J.M., Davis, A.P., Dolinski, K.,
1172 Dwight, S.S., Eppig, J.T., et al. (2000). Gene Ontology: tool for the unification of biology. Nat. Genet. *25*,
1173 25–29.
1174 Ast, T., Michaelis, S., and Schuldiner, M. (2016). The Protease Ste24 Clears Clogged Translocons. Cell
1175 *164*, 103–114.
1176 Bernales, S., McDonald, K.L., and Walter, P. (2006). Autophagy counterbalances endoplasmic reticulum
1177 expansion during the unfolded protein response. PLoS Biol. *4*, 2311–2324.
1178 Beveridge, R., Covill, S., Pacholarz, K.J., Kalapothakis, J.M.D., MacPhee, C.E., and Barran, P.E. (2014).
1179 A Mass-Spectrometry-Based Framework To Define the Extent of Disorder in Proteins. Anal. Chem. *86*,
1180 10979–10991.
1181 Birgisdottir, Å.B., Lamark, T., and Johansen, T. (2013). The LIR motif - crucial for selective autophagy.
1182 J. Cell Sci. *126*, 3237–3247.
1183 BOLTE, S., and CORDELIÈRES, F.P. (2006). A guided tour into subcellular colocalization analysis in
1184 light microscopy. J. Microsc. *224*, 213–232.
1185 Chen, Q., Xiao, Y., Chai, P., Zheng, P., Teng, J., and Chen, J. (2019). ATL3 Is a Tubular ER-Phagy
1186 Receptor for GABARAP-Mediated Selective Autophagy. Curr. Biol. *29*, 846-855.e6.
1187 Chino, H., and Mizushima, N. (2020). ER-Phagy : Quality Control and Turnover of Endoplasmic
1188 Reticulum. Trends Cell Biol. 1–15.
1189 Chino, H., Hatta, T., Natsume, T., and Mizushima, N. (2019). Intrinsically Disordered Protein TEX264
1190 Mediates ER-phagy. Mol. Cell 1–13.
1191 Clough, S.J., and Bent, A.F. (1998). Floral dip: a simplified method for Agrobacterium -mediated
1192 transformation of Arabidopsis thaliana. Plant J. *16*, 735–743.
1193 Dennis, G., Sherman, B.T., Hosack, D.A., Yang, J., Gao, W., Lane, H.C., and Lempicki, R.A. (2003).
1194 DAVID: Database for Annotation, Visualization, and Integrated Discovery. Genome Biol. *4*, R60.
1195 Dikic, I. (2018). Open questions: why should we care about ER-phagy and ER remodelling? BMC Biol.
1196 *16*, 131.
1197 Dikic, I., and Elazar, Z. (2018). Mechanism and medical implications of mammalian autophagy. Nat.
1198 Rev. Mol. Cell Biol. *19*, 349–364.

1199 Dorfer, V., Pichler, P., Stranzl, T., Stadlmann, J., Taus, T., Winkler, S., and Mechtler, K. (2014). MS
1200 Amanda, a Universal Identification Algorithm Optimized for High Accuracy Tandem Mass Spectra. J.
1201 Proteome Res. *13*, 3679–3684.
1202 Fregno, I., and Molinari, M. (2019). Proteasomal and lysosomal clearance of faulty secretory proteins:
1203 ER-associated degradation (ERAD) and ER-to-lysosome-associated degradation (ERLAD) pathways.
1204 Crit. Rev. Biochem. Mol. Biol. *54*, 153–163.
1205 Fumagalli, F., Noack, J., Bergmann, T.J., Cebollero Presmanes, E., Pisoni, G.B., Fasana, E., Fregno, I.,
1206 Galli, C., Loi, M., Soldà, T., et al. (2016). Translocon component Sec62 acts in endoplasmic reticulum
1207 turnover during stress recovery. Nat. Cell Biol. *18*, 1173–1184.
1208 Gerakis, Y., Quintero, M., Li, H., and Hetz, C. (2019). The UFMylation System in Proteostasis and
1209 Beyond. Trends Cell Biol. *29*, 974–986.
1210 Grumati, P., Morozzi, G., Hölper, S., Mari, M., Harwardt, M.-L.I., Yan, R., Müller, S., Reggiori, F.,
1211 Heilemann, M., and Dikic, I. (2017). Full length RTN3 regulates turnover of tubular endoplasmic
1212 reticulum via selective autophagy. Elife *6*, e25555.
1213 Huber, J., Obata, M., Gruber, J., Akutsu, M., Löhr, F., Rogova, N., Güntert, P., Dikic, I., Kirkin, V.,
1214 Komatsu, M., et al. (2019). An atypical LIR motif within UBA5 (ubiquitin like modifier activating
1215 enzyme 5) interacts with GABARAP proteins and mediates membrane localization of UBA5. Autophagy
1216 *0*, 15548627.2019.1606637.
1217 Hübner, C.A., and Dikic, I. (2019). ER-phagy and human diseases. Cell Death Differ.
1218 Huerta-Cepas, J., Szklarczyk, D., Forslund, K., Cook, H., Heller, D., Walter, M.C., Rattei, T., Mende,
1219 D.R., Sunagawa, S., Kuhn, M., et al. (2015). eggNOG 4.5: a hierarchical orthology framework with
1220 improved functional annotations for eukaryotic, prokaryotic and viral sequences. Nucleic Acids Res. *44*,
1221 D286–D293.
1222 Ishizaki, K., Nishihama, R., Ueda, M., Inoue, K., Ishida, S., Nishimura, Y., Shikanai, T., and Kohchi, T.
1223 (2015). Development of Gateway Binary Vector Series with Four Different Selection Markers for the
1224 Liverwort Marchantia polymorpha. PLoS One *10*, e0138876.
1225 Jia, M., Liu, X., Xue, H., Wu, Y., Shi, L., Wang, R., Chen, Y., Xu, N., Zhao, J., Shao, J., et al. (2019).
1226 Noncanonical ATG8–ABS3 interaction controls senescence in plants. Nat. Plants.
1227 Johansen, T., and Lamark, T. (2019). Selective Autophagy: ATG8 Family Proteins, LIR Motifs and
1228 Cargo Receptors. J. Mol. Biol.
1229 Käll, L., Canterbury, J.D., Weston, J., Noble, W.S., and MacCoss, M.J. (2007). Semi-supervised learning
1230 for peptide identification from shotgun proteomics datasets. Nat. Methods *4*, 923–925.
1231 Karagöz, G.E., Acosta-Alvear, D., and Walter, P. (2019). The Unfolded Protein Response: Detecting and
1232 Responding to Fluctuations in the Protein-Folding Capacity of the Endoplasmic Reticulum. Cold Spring
1233 Harb. Perspect. Biol. a033886.

1234 Kellner, R., De la Concepcion, J.C., Maqbool, A., Kamoun, S., and Dagdas, Y.F. (2016). ATG8
1235 Expansion: A Driver of Selective Autophagy Diversification? Trends Plant Sci.
1236 Khaminets, A., Heinrich, T., and Dikic, I. (2015). Regulation of endoplasmic reticulum turnover by
1237 selective autophagy. Nature *522*, 354–358.
1238 Kim, J.-S., Yamaguchi-Shinozaki, K., and Shinozaki, K. (2018). ER-Anchored Transcription Factors
1239 bZIP17 and bZIP28 Regulate Root Elongation. Plant Physiol. *176*, 2221 LP – 2230.
1240 Klionsky, D.J., Deretic, V., Vi, V.I., and Vi, V.I.V.I. (2011). Autophagy : molecular mechanisms and
1241 disease outcomes. Cell 2011–2011.
1242 Koizumi, N., Martinez, I.M., Kimata, Y., Kohno, K., Sano, H., and Chrispeels, M.J. (2001). Molecular
1243 Characterization of Two Arabidopsis Ire1 Homologs, Endoplasmic Reticulum-Located Transmembrane
1244 Protein Kinases. Plant Physiol. *127*, 949 LP – 962.
1245 KUBOTA, A., ISHIZAKI, K., HOSAKA, M., and KOHCHI, T. (2013). Efficient Agrobacterium-
1246 Mediated Transformation of the Liverwort Marchantia polymorpha Using Regenerating Thalli. Biosci.
1247 Biotechnol. Biochem. *77*, 167–172.
1248 Kulsuptrakul, J., Wang, R., Meyers, N.L., Ott, M., and Puschnik, A.S. (2019). A CRISPR screen
1249 identifies UFMylation and TRAMP-like complexes required for hepatitis A virus infection. BioRxiv
1250 2019.12.15.877100.
1251 Lahiri, V., and Klionsky, D.J. (2018). CCPG1 is a noncanonical autophagy cargo receptor essential for
1252 reticulophagy and pancreatic ER proteostasis. Autophagy *14*, 1107–1109.
1253 Lampropoulos, A., Sutikovic, Z., Wenzl, C., Maegele, I., Lohmann, J.U., and Forner, J. (2013).
1254 GreenGate - A novel, versatile, and efficient cloning system for plant transgenesis. PLoS One *8*.
1255 Leto, D.E., Morgens, D.W., Zhang, L., Walczak, C.P., Elias, J.E., Bassik, M.C., and Kopito, R.R. (2019).
1256 Genome-wide CRISPR Analysis Identifies Substrate-Specific Conjugation Modules in ER-Associated
1257 Degradation. Mol. Cell *73*, 377-389.e11.
1258 Liang, J.R., Lingeman, E., Luong, T., Ahmed, S., Muhar, M., Nguyen, T., Olzmann, J.A., and Corn, J.E.
1259 (2020). A Genome-wide ER-phagy Screen Highlights Key Roles of Mitochondrial Metabolism and ER-
1260 Resident UFMylation. Cell.
1261 Ma, X., Zhang, Q., Zhu, Q., Liu, W., Chen, Y., Qiu, R., Wang, B., Yang, Z., Li, H., Lin, Y., et al. (2015).
1262 A Robust CRISPR/Cas9 System for Convenient, High-Efficiency Multiplex Genome Editing in Monocot
1263 and Dicot Plants. Mol. Plant *8*, 1274–1284.
1264 Madeira, F., Park, Y.M., Lee, J., Buso, N., Gur, T., Madhusoodanan, N., Basutkar, P., Tivey, A.R.N.,
1265 Potter, S.C., Finn, R.D., et al. (2019). The EMBL-EBI search and sequence analysis tools APIs in 2019.
1266 Nucleic Acids Res. *47*, W636–W641.
1267 Maly, D.J., and Papa, F.R. (2014). Druggable sensors of the unfolded protein response. Nat. Chem. Biol.
1268 *10*, 892–901.

1269 Marshall, R.S., and Vierstra, R.D. (2018). Autophagy: The Master of Bulk and Selective Recycling.
1270 Annu. Rev. Plant Biol. *69*, 173–208.
1271 Marshall, R.S., Hua, Z., Mali, S., McLoughlin, F., and Vierstra, R.D. (2019). ATG8-Binding UIM
1272 Proteins Define a New Class of Autophagy Adaptors and Receptors. Cell 1–16.
1273 Mochida, K., Oikawa, Y., Kimura, Y., Kirisako, H., Hirano, H., Ohsumi, Y., and Nakatogawa, H.
1274 Receptor-mediated selective autophagy degrades the endoplasmic reticulum and the nucleus.
1275 Naumann, C., Müller, J., Sakhonwasee, S., Wieghaus, A., Hause, G., Heisters, M., Bürstenbinder, K., and
1276 Abel, S. (2019). The Local Phosphate Deficiency Response Activates Endoplasmic Reticulum Stress-
1277 Dependent Autophagy. Plant Physiol. *179*, 460–476.
1278 Ravenhill, B.J., Boyle, K.B., von Muhlinen, N., Ellison, C.J., Masson, G.R., Otten, E.G., Foeglein, A.,
1279 Williams, R., and Randow, F. (2019). The Cargo Receptor NDP52 Initiates Selective Autophagy by
1280 Recruiting the ULK Complex to Cytosol-Invading Bacteria. Mol. Cell *0*, 1–10.
1281 Shin, Y.J., Vavra, U., Veit, C., and Strasser, R. (2018). The glycan-dependent ERAD machinery degrades
1282 topologically diverse misfolded proteins. Plant J. *94*, 246–259.
1283 Slovak, R., Göschl, C., Su, X., Shimotani, K., Shiina, T., and Busch, W. (2014). A scalable open-source
1284 pipeline for large-scale root phenotyping of Arabidopsis. Plant Cell *26*, 2390–2403.
1285 Smith, M.D., Harley, M.E., Kemp, A.J., Wills, J., Lee, M., Arends, M., von Kriegsheim, A., Behrends,
1286 C., and Wilkinson, S. (2018). CCPG1 Is a Non-canonical Autophagy Cargo Receptor Essential for ER-
1287 Phagy and Pancreatic ER Proteostasis. Dev. Cell *44*, 217-232.e11.
1288 Smyth, G.K. (2004). Linear models and empirical bayes methods for assessing differential expression in
1289 microarray experiments. Stat. Appl. Genet. Mol. Biol. *3*, Article3.
1290 Stephani, M., and Dagdas, Y. (2019). Plant Selective Autophagy - Still an uncharted territory with a lot of
1291 hidden gems. J. Mol. Biol.
1292 Stolz, A., and Grumati, P. (2019). The various shades of ER-phagy. FEBS J. *286*, 4642–4649.
1293 Stolz, A., Ernst, A., and Dikic, I. (2014). Cargo recognition and trafficking in selective autophagy. Nat.
1294 Publ. Gr. *16*, 495–501.
1295 Sugano, S.S., Nishihama, R., Shirakawa, M., Takagi, J., Matsuda, Y., Ishida, S., Shimada, T., Hara-
1296 Nishimura, I., Osakabe, K., and Kohchi, T. (2018). Efficient CRISPR/Cas9-based genome editing and its
1297 application to conditional genetic analysis in Marchantia polymorpha. PLoS One *13*, e0205117.
1298 Sun, Z., and Brodsky, J.L. (2019). Protein quality control in the secretory pathway. J. Cell Biol. *218*,
1299 3171–3187.
1300 Ticconi, C.A., Lucero, R.D., Sakhonwasee, S., Adamson, A.W., Creff, A., Nussaume, L., Desnos, T., and
1301 Abel, S. (2009). ER-resident proteins PDR2 and LPR1 mediate the developmental response of root
1302 meristems to phosphate availability. Proc. Natl. Acad. Sci. *106*, 14174 LP – 14179.
1303 Turco, E., Witt, M., Abert, C., Bock-Bierbaum, T., Su, M.-Y., Trapannone, R., Sztacho, M., Danieli, A.,

Shi, X., Zaffagnini, G., et al. (2019). FIP200 Claw Domain Binding to p62 Promotes Autophagosome Formation at Ubiquitin Condensates. Mol. Cell *0*, 1–17.

Vargas, J.N.S., Wang, C., Bunker, E., Hao, L., Maric, D., Schiavo, G., Randow, F., and Youle, R.J. (2019). Spatiotemporal Control of ULK1 Activation by NDP52 and TBK1 during Selective Autophagy. Mol. Cell *0*, 1–16.

Walczak, C.P., Leto, D.E., Zhang, L., Riepe, C., Muller, R.Y., DaRosa, P.A., Ingolia, N.T., Elias, J.E., and Kopito, R.R. (2019). Ribosomal protein RPL26 is the principal target of UFMylation. Proc. Natl. Acad. Sci. *116*, 1299–1308.

Walter, P., and Ron, D. (2011). The Unfolded Protein Response: From Stress Pathway to Homeostatic Regulation. Science (80-.). *334*, 1081 LP – 1086.

Wamsley, J.J., Gary, C., Biktasova, A., Hajek, M., Bellinger, G., Virk, R., Issaeva, N., and Yarbrough, W.G. (2017). Loss of LZAP inactivates p53 and regulates sensitivity of cells to DNA damage in a p53-dependent manner. Oncogenesis *6*.

Wang, L., Xu, Y., Rogers, H., Saidi, L., Noguchi, C.T., Li, H., Yewdell, J.W., Guydosh, N.R., and Ye, Y. (2019). UFMylation of RPL26 links translocation-associated quality control to endoplasmic reticulum protein homeostasis. Cell Res.

Wild, P., McEwan, D.G., and Dikic, I. (2014). The LC3 interactome at a glance. J. Cell Sci. *127*, 3–9.

Wilkinson, S. (2019). Emerging Principles of Selective ER Autophagy. J. Mol. Biol.

Xing, H.L., Dong, L., Wang, Z.P., Zhang, H.Y., Han, C.Y., Liu, B., Wang, X.C., and Chen, Q.J. (2014). A CRISPR/Cas9 toolkit for multiplex genome editing in plants. BMC Plant Biol. *14*, 1–12.

Yang, R., Wang, H., Kang, B., Chen, B., Shi, Y., Yang, S., Sun, L., Liu, Y., Xiao, W., Zhang, T., et al. (2019). CDK5RAP3, a UFL1 substrate adaptor, is crucial for liver development. Development *146*, dev169235.

Yang, X., Srivastava, R., Howell, S.H., and Bassham, D.C. (2016). Activation of autophagy by unfolded proteins during endoplasmic reticulum stress. Plant J. *85*, 83–95.

Zaffagnini, G., and Martens, S. (2016). Mechanisms of Selective Autophagy. J. Mol. Biol. *428*, 1714–1724.

Zhang, X., Ding, X., Marshall, R.S., Paez-Valencia, J., Lacey, P., Vierstra, R.D., and Otegui, M. (2020). Reticulon proteins modulate autophagy of the endoplasmic reticulum in maize endosperm. Elife *9*, e51918.

Zhuang, X., Chung, K.P., Cui, Y., Lin, W., Gao, C., Kang, B.-H., and Jiang, L. (2017). ATG9 regulates autophagosome progression from the endoplasmic reticulum in Arabidopsis; Proc. Natl. Acad. Sci. *114*, E426 LP-E435.